ABSTRACT

Title of Dissertation:	Fluorescent Carbon Nanotubes as Molecular Sensors and Color-Center Hosts
	Haoran Qu, Doctor of Philosophy, 2022
Dissertation directed by:	Professor YuHuang Wang
	Department of Chemistry and Biochemistry

This thesis demonstrates the application of single-walled carbon nanotubes (SWCNTs) as single-digit nanopores for molecular sieving and addresses a fundamental challenge pertaining to controlled synthesis of organic color-centers (OCCs) on the sp^2 carbon lattice of SWCNTs. First, I describe a hyperspectral single-defect photoluminescence imager system that provides both hyperspectral imaging and super-resolution capabilities in the shortwave infrared. Second, I aim to understand the relationship between nanotube photoluminescence and encapsulated molecules. Using carbon nanotubes with sub-1 nm pores, I demonstrate molecular sieving of n-hexane from cyclohexane, which are nearly identical in size. Furthermore, I discovered a light irradiation method to drive structural transformation of OCCs which allow us to narrow the spectral distribution of defect emissions by 26%. Finally, I show that [2+2] cycloaddition can efficiently create OCCs. Remarkably, this novel defect chemistry reduces the number of OCC bonding configurations from six, which are commonly observed with monovalent defect chemistries, to just three. This work may have broad implications to the potential applications of SWCNTs and OCCs in chemical sensing, bioimaging, and quantum information science.

FLUORESCENT CARBON NANOTUBES AS MOLECULAR SENSORS AND
COLOR-CENTER HOSTS

by

Haoran Qu

Dissertation submitted to the Faculty of the Graduate School of the
University of Maryland, College Park, in partial fulfillment
of the requirements for the degree of
Doctor of Philosophy
2022

Dissertation Committee:
 Professor Wang, YuHuang, Chair
 Professor Lee, Sang Bok
 Professor Nemes, Peter
 Dr. Zheng, Ming
 Dean's Representative: Professor Cumings, John

Acknowledgments

First of all, I would like to express my gratitude to my advisor, Prof. YuHuang Wang for his support in my Ph.D. study. I appreciate the opportunity to work on the exciting research in Wang Research Group. I enjoyed working with all the Wang group members and appreciate their advice and helpful discussion. Especially, I thank Dr. Xiaojian Wu, Dr. Peng Wang, Dr. Mijin Kim, Dr. Alexandra Brozena, Jacob Fornter, Benjamin Barnes, Chiyu Zhang, and Ziyi Wang for their help along my Ph.D.

I would also like to thank Prof. John Cumings, Prof. Sang Bok Lee, Dr. Ming Zheng, and Prof. Peter Nemes for serving on my committee.

I am grateful to all my collaborators for their work and support. Especially, I thank Dr. Narayana Aluru and Archith Rayabharam for the molecular dynamic and quantum simulation. I thank Dr. Jeffery Fagan and Dr. Ming Zheng for the preparation of high-purity carbon nanotube samples. I thank Prof. Michael Strano, Dr. Matthias Kuehne, and Samuel Faucher for the collaborations on Raman spectroscopy. I thank Prof. John Cumings and Kyle Sendgikoski for the collaboration on electron microscopy on carbon nanotubes.

I thank my friends who are always on my side and make unforgettable memories during the past five years.

Lastly, I would like to thank my family including my fiancé, Xinye Liu, and my parents, Bing Wang and Bo Wang, for their unconditional love and support. I want to acknowledge my furry friends, Tuna and Salmon, my cats, for providing me with their companionship during stressful times and bring up smiles to my face.

Table of Contents

iv

List of Tables

List of Figures

List of Abbreviations

0D: Zero-dimensional
1D: One-dimensional
2D: Two-dimensional
3D: Three-dimensional
MWCNT: Multi-walled carbon nanotube
SWCNT: Single-walled carbon nanotube
SDNs: Single Digit Nanopores
E_b: Exciton binding energy
PL: Photoluminescence
UV: Ultraviolet
vis: Visible
NIR: Near-infrared
OD: Optical density
FWHM: Full width at half maximum
DOC: Sodium deoxycholate
SDS: Sodium dodecyl sulfate
SDBS: Sodium dodecylbenzenesulfonate
ATPE: Polymer aqueous two-phase extraction
DZ: Diazonium salts
DFT: Density functional theory
TD-DFT: Time-dependent density functional theory
PS: Polystyrene
NA: Numerical aperture
RWI: Read while integrate
ROI: Region of interest
NTO: Natural transition orbitals

1 Introduction

Parts of this introduction are adapted from published works I co-authored:

Qu, H.; Wu, X.; Fortner, J.; Kim, M.; Wang, P.; Wang, Y., Reconfiguring Organic Color Centers on the sp² Carbon Lattice of Single-Walled Carbon Nanotubes. ACS Nano 2022, 16, 2077-2087.

Carbon is the 4th most abundant element on earth. It can form allotropes of different dimensions, including fullerenes (0D), carbon nanotubes (1D), graphene (2D), and graphite (3D). The discovery of carbon nanotubes may be traced all the way back to 1952 when hollow carbon fibers were observed.[1] Later in 1991, Iijima revealed the molecular structure of multi-walled carbon nanotubes (MWCNTs) as multilayer graphitic tubular structures using transmission electron microscopy.[2] These MWCNTs are analogous to graphite in terms of their electronic properties. Therefore, research in the early stage was primarily focused on the mechanical properties,[3-5] electrical conductivity,[6] and thermal conductivity.[7] In 1993, the first synthetic process for single-walled carbon nanotubes (SWCNTs) was discovered by the NEC and IBM groups.[8, 9] These SWCNTs can be seen as single layers of graphene rolled up in a helical fashion. This discovery has enabled a great expansion of the nanomaterial field, allow investigation of the fundamental properties and applications of carbon nanotubes.

The interest in SWCNTs is primarily driven by the intriguing properties of these quasi-1D materials. The smooth 1D interior channel, chemical stability, well-defined nanopores, and distinct optical properties of SWCNTs have led to enhanced transport

rates inside these 1D pipes,[10] alteration of freezing point of the encapsulated molecules,[11] and applications, such as electronic[12, 13] and optical devices,[14-16] biosensing,[17, 18] and single photon sources for quantum communications,[19-21] among many others.

1.1 Chirality of SWCNTs

The rolled-up direction of SWCNTs can be described by a specific wrapping vector $C_h = n\vec{a_1} + m\vec{a_2} \equiv (n, m)$ (Figure 1-1).[22] The chiral vector is defined in terms of the primitive lattice vectors of a graphene unit cell, $\vec{a_1}$ and $\vec{a_2}$. This vector, denoting the chirality of SWCNTs, determines their physical and chemical properties. Each specific chirality has a well-defined diameter (d) calculated by equation 1-1, a chiral angle (θ) calculated by equation 1-2, a smooth wall made by sp^2 honeycomb carbon, a well-defined one-dimensional pore, and distinct optical properties.

$$d = \frac{C_h}{\pi} = a_{c-c}\sqrt{3(m^2 + n^2 + nm)}/\pi \qquad \text{Equation 1-1}$$

$$\theta = \tan^{-1}\frac{\sqrt{3}\,m}{2n+m} \qquad \text{Equation 1-2}$$

where a_{c-c} is the distance between two sp^2 carbons in the lattice (1.44 Å). To study structure dependence of SWCNTs, (n,m) chirality is categorized by mod and family. ($n–m$) mod categorizes SWCNTs with similar chiral angle but varying diameter. ($2n+m$) family groups SWCNTs with similar diameter but varying chiral angle. Depending on the (n, m), SWCNTs can be grouped into metallic SWCNTs $mod(n - m, 3) = 0$), and small bandgap semiconducting SWCNTs $mod(n - m, 3) = 1\ or\ 2)$. If m = 0, nanotubes are called "zigzag" ($\theta = 0°$) and if n = m, nanotubes are called "armchair" ($\theta = 30°$). The structure variation is closely related to the electronic

structure of SWCNTs, because this rolling of the graphene sheet imposes specific boundary conditions on the electronic wavefunction in the direction of rolling.
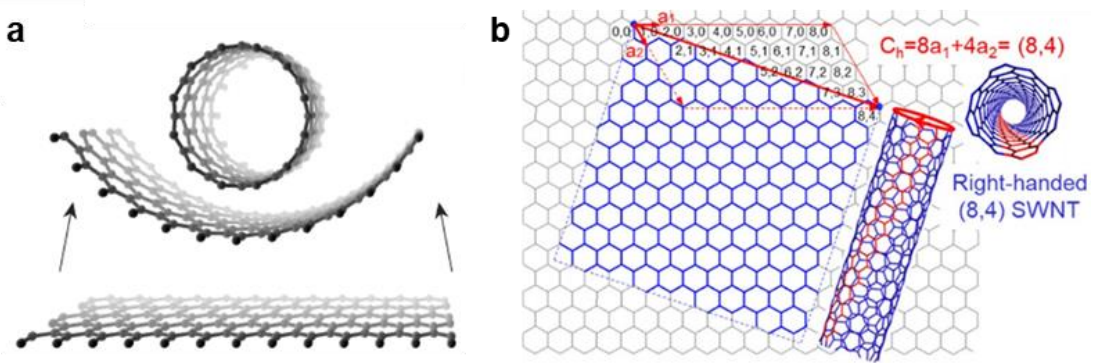
Figure 1-1. Schematic illustration of. a, a SWCNT rolled up from a graphene sheet. b, the chirality related to the wrapping vector (n, m). Figure 1-1b adapted from ref 23.

1.2   Optical Properties of SWCNTs

The electronic structure of a SWCNT can originate from that of single layer graphene according to the hexagonal Brillouin zone. Figure 1-2a shows the band structure of graphene near the Fermi level. In the 2D Brillouin zone, the Fermi level lies at the crossing points between an occupied π band and an empty π^* band, denoted by K and K'. The π and π^* bands have a linear dispersion around the K and K' points, and the valence and conduction bands meet at the Fermi level at the K and K' points. Hence, graphene is a zero-gap semiconductor.

In contrast, SWCNTs can be metallic or semiconducting with different energy gaps, depending on the diameter. The physics behind this variation of the electronic structures can be explained by trigonal wrapping effects.[24] For a mod 0 SWCNT, a cutting line (k line) crosses the K point, and thus it is metallic with continuous density of states (DOS) at the Fermi energy resulting in no photoluminescence (PL) (Figure

1-3a). On the other hand, for semiconducting, there is no allowed k-line cross K point

(Figure 1-2b), exhibiting chirality-dependent transitional energies (E_{ii}) (Figure 1-3b).[23]
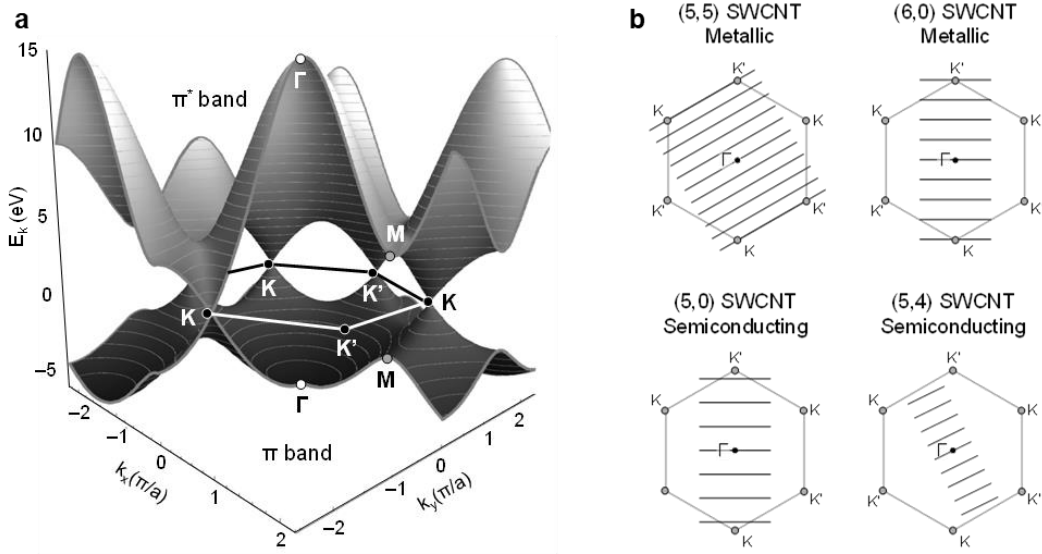
Figure 1-2. Brillouin zone of Graphene (a) and SWCNTs (b).
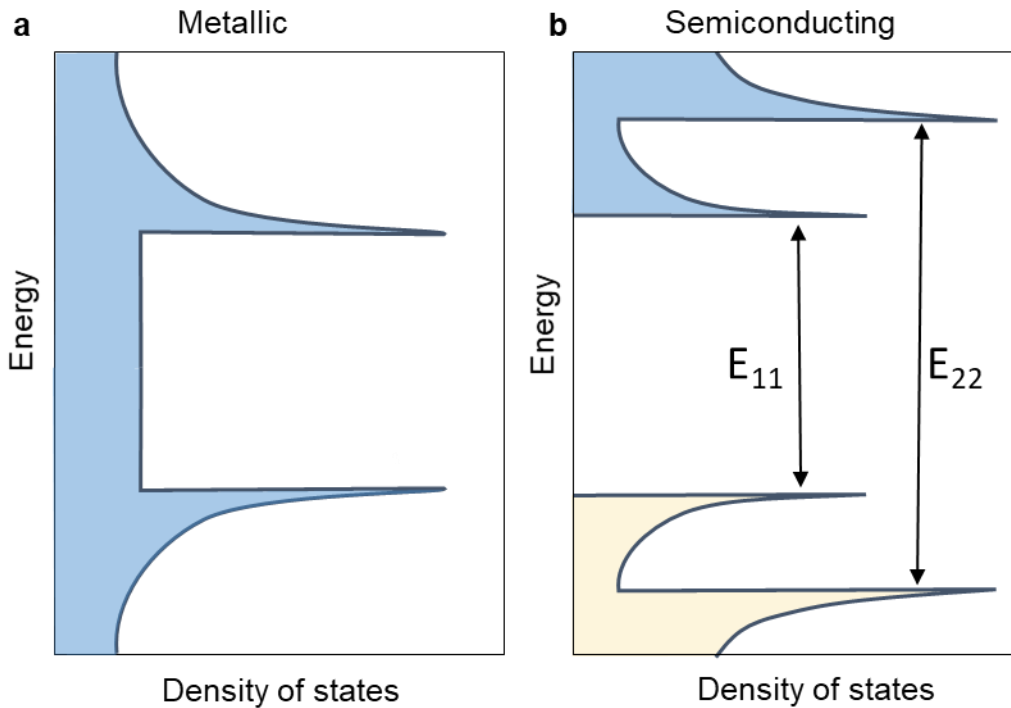
Figure 1-3. Density of States (DOS) plots of metallic nanotubes (a) and semiconducting nanotubes (b).

The DOS of SWCNTs exhibit the Van Hove singularity (VHs) characteristic of 1D electronic systems. Distinct optical resonance occurs between the VHs peaks. Under light illumination, excited electrons and holes are generated by absorption of photons. These electrons are excited to conduction bands and leave holes in the valence band. A negatively charged electron and a positively charged hole interact through the attractive Coulombic force forming a two-particle bound-state, called the exciton, which are stabilized by the binding energy E_b of the two particles with opposite charges. In SWCNTs, the E_b on the order of 500 meV is significantly higher than that of bulk semiconductors (~26 meV).[25] As a result, the optical resonance in SWCNTs occurs at the photon energy (wavelength) corresponding to the exciton energy emitting as E_{11} photoluminescence (PL) instead of the quasi particle bandgap energy. Note that the SWCNTs' optical properties mainly arise from a series of optically allowed E_{ii} transitions which indicates the transition between ith VHs of conduction and valence band, while the E_{ij} ($i \neq j$) is optically forbidden due to strong depolarization).

1.2.1 Spectroscopic Characterization of SWCNTs

Multiple instruments can be used to detect the E_{ii} optical transition. However, the optical signatures of SWCNTs are significantly different. For example, the optical absorption spectra of as-grown bundled SWCNTs are considerably different from those of individualized SWCNTs. In the case of PL, it is generally difficult to observed PL from as-grown bundles owing to the rapid nonradiative relaxation of excitons in semiconducting SWCNTs into metallic SWCNTs that are bundled.[26] This can be avoided by individually dispersing bundled SWCNTs by tip sonication,[26] shear force

mixing,[27] and superacid-surfactant exchange,[28, 29] and stabilized in aqueous surfactant solution or polymer organic solution. Therefore, in this dissertation, we mainly focus on individualized SWCNTs that allow detection of their PL.

1.2.1.1   Optical Absorption Spectroscopy

Optical absorption spectroscopy is one of the most fundamental techniques for directly probing electronic transitions in SWCNTs. The chirality-dependent excitonic transitions (E_{ii}, i = 1,2,3,…) of SWCNTs can be directly resolved by absorption spectroscopy (Figure 1-4a). For SWCNTs that have relatively small diameters (0.6-1.5 nm), their E_{ii} transitions appear in the near-infrared (NIR), visible and ultraviolet (UV) regions. The D-phonon sideband of each E_{ii} transition is 200-300 meV lower than the primary E_{ii} absorption band originating from the phonon-assisted transitions. Figure 1-4a shows an absorption spectrum of High-pressure carbon monoxide (HiPco) SWCNTs. The optical absorption spectra provide a fingerprint to identify the chirality of SWCNTs. The absorbance of the peak can be used for quantitative analysis of the composition and fraction of chirality-sorted SWCNT according to Lambert-Beer's law. In addition, the sharpness of the peaks indicates the percentage of individually dispersed SWCNTs in solution. Bundled SWCNTs do not have sharp absorbance features.
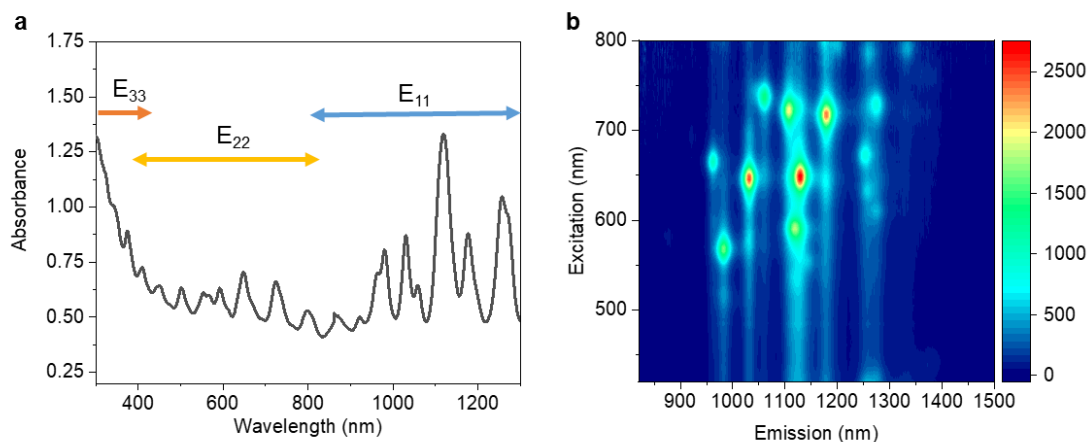
Figure 1-4. Optical properties of SWCNTs. a, absorption spectroscopy showing E_{11}, E_{22}, and E_{33} transitions for HiPco SWCNTs in 1% DOC/D_2O. b, PL excitation map for HiPco SWCNTs in 1% DOC/D_2O.

1.2.1.2 Photoluminescence spectroscopy

The bandgap and large exciton binding energy in semiconducting SWCNTs enables NIR PL at room temperature.[26] This PL and its quantum yield are influenced by the chirality, length, defect density and surrounding environment. Therefore, PL spectroscopy is a sensitive tool for studying the excitonic properties of SWCNTs. The PL excitation (PLE) map of HiPco SWCNTs shown in Figure 1-4b provides a basis for identifying the chirality of SWCNTs as one can identify the E_{22} absorption and corresponding E_{11} emission. A vertical slice of the PLE map at E_{11} of (n, m)-SWCNTs traces the absorption profile while the horizontal slice of the PLE map represents the PL emission spectrum excited at specific wavelength. In the PL spectrum of (n, m)-SWCNTs, the strong PL emission related to the radiative recombination of E_{11} excitons. A low intensity D-phonon sideband can be observed at ~140 meV lower in energy than E_{11} PL, which originated from phonon-assisted excitonic recombination.[30] In addition, this E_{11} PL is sensitive to the environment both outside[31, 32] and inside[33-35] the hollow nanotubes. As such PL spectra provide rich information on the optical

7

properties of SWCNTS as well as their surroundings. Furthermore, the optical properties of semiconducting SWCNTs are beneficial for many optoelectronic and biological applications, including their use as a single-photon source[36] and in bioimaging.[37]

1.2.1.3 Raman Spectroscopy

Raman spectroscopy is a useful tool for graphitic materials, such as carbon nanotubes and graphene, as these structures have signature G band and D band (Figure 1-5). G band commonly at 1500-1600 cm^{-1} in the Raman spectrum represents the an in-plane tangential optical phonon involving the stretching of the bond between two atoms in the graphitic unit cell.[38, 39] This G band of SWCNTs split into G$^+$ (~1590 cm^{-1}) and G$^-$ band (1572 cm^{-1}) due to the curvature effects, as they are related to the circumferential and axial atomic vibration. In addition, the line shape and wavenumbers of peaks are determined by the SWCNT type. D band at 1350 cm^{-1} represents disorder-related vibration induced by symmetry breaking on the hexagonal sp^2 carbon lattice. Therefore, the D/G ratio is used for characterizing the relative density of defects on the SWCNTs.

Another featured Raman signal is radial breathing mode (RBM) of SWCNTs. It represents the vibration in the radial direction of nanotubes and is not observed in other sp^2 carbon materials. The peak position strongly depends on the diameter of nanotubes following the equation:[38]

$$\omega_{RBM} = \frac{218}{d} \qquad\qquad \text{Equation 1-3}$$

where ω_{RBM} and d are the RBM frequency and diameter of the SWCNT, respectively. This RBM is also sensitive to the surrounding environment both inside and outside

nanotubes as the molecules or ions in the environment directly affect the carbon atom.[11, 40]
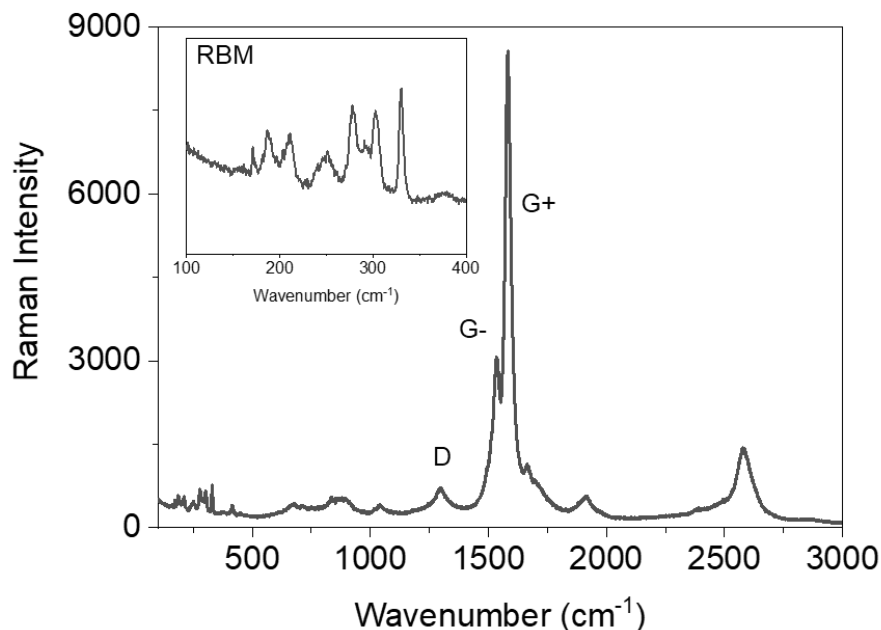
Figure 1-5. Raman spectrum of CoMoCat SG65i SWCNTs excited with 532 nm laser. The RBM band are zoomed in (inset).

1.3 Nanopore and 1D Channel of SWCNTs

Single Digit Nanopores (SDNs) are nanopores that have characteristic diameters or conduit widths less than 10 nm and have only recently been accessible experimentally for precision transport measurement.[41] The recent studies of transport in SDNs reveal many counterintuitive behaviors that often defy a continuum description of fluid flow. Specifically, SDNs can be tailored to sieve ions from salt water and serve as membranes for seawater desalination,[42, 43] differentiate liquid flow and serve as sensors,[44] and enhance proton transport.[10]

As a hollow cylindrical structure, the interior 1D channel of SWCNTs possesses interesting properties as SDNs. The SWCNT nanopore is atomically smooth, providing

9

an enhanced flux for liquid to penetrate through the channel,[45, 46] with well-defined pore diameter allowing ion or molecular selectivity.[34, 47] The diameter of SDNs depend on the SWCNT chirality which can be enriched by several sorting method, which will be discussed in later sections.

The as-grown SWCNTs are commonly capped or end-closed with semi-fullerene structure or catalysts. Additional thermal oxidation is required to open the ends and allow liquid to access the SDN interior. The resulting SWCNTs can be filled with a variety of liquids depending on their diameter.[48] Note that dispersion of nanotubes in aqueous solution via tip sonication commonly allows water molecules to spontaneously fill in and results in a redshift in E_{11}.[33, 49] This shifted E_{11} can be used as an indicator to find the status of the SWCNT interior.

Empty SWCNTs can serve as an essential control to differentiate the interior confinement effect from that caused by outside environment change. Density gradient ultracentrifugation (DGU) has been used for sorting empty SWCNTs from water-filled SWCNTs due to the buoyant density difference between them.[49, 50]

1.4 Preparation of Chirality-Sorted SWCNTs

Carbon nanotubes are synthesized as a mixture of different chiralities, although current synthesis methods, such as CoMoCat®, HiPco, arc-discharge, and laser oven, can produce CNTs in certain diameter ranges. Therefore, non-destructive methods are necessary to separate semiconducting nanotubes or specific chiralities from the mixture. The purified SWCNTs are essential requirement for comprehensible study on PL emissions as the OCCs emissions can overlap with E_{11} of other chiralities.

Purification has been achieved via several methods. Zheng *et al.* demonstrated high purity of single chirality enriched SWCNTs by the aqueous two-phase extraction (ATPE) with the assistance of DNA sequences that recognize particular nanotubes species.[51, 52] More than 21 species can be enriched via this method. Fagan *et al.* varies the surfactant concentration in ATPE to achieve a versatile sorting of SWCNTs with diameter ranging from 0.6 nm to 1.4 nm.[53] This is a powerful method without introducing additional compounds to modify the nanotube surface, and the polymer used in ATPE can be easily removed by ultrafiltration while leaving the nanotubes intact.

1.5   Organic Color Centers (OCCs)

Even though the unique electronic and optical properties of semiconducting SWCNTs have been intensively studied, the low PL quantum yields of ~1%[54] and difficulty in chemically controlling their optical properties after synthesis have been hindering the application of SWCNTs.

Our group found that covalently bonding a low density of functional groups to the semiconducting SWCNTs creating a whole new class of emitters, named as organic color centers (OCCs), helps to mitigate these challenges.[55-58]   OCCs introduce new optically allowed quantum states in the electronic structure of SWCNTs. This new quantum state is lower in energy than the E_{11} excitonic states, thus an exciton diffusing along the nanotubes can be trapped locally at the defect site and emit a bright OCC emission E_{11}^- (Figure 1-6a). This energy level is lower than the dark state. As a result, the OCC emissions are orders of magnitude brighter and have higher quantum yield compared to pristine SWCNTs. Piao *et al.* first reported the new, bright

photoluminescence through sp³ defects with aryl diazonium salts.[59] This method induces photoluminescence brightening up to 8-fold for (6,5)-SWCNTs and 28-fold for (6,4)-SWCNTs.
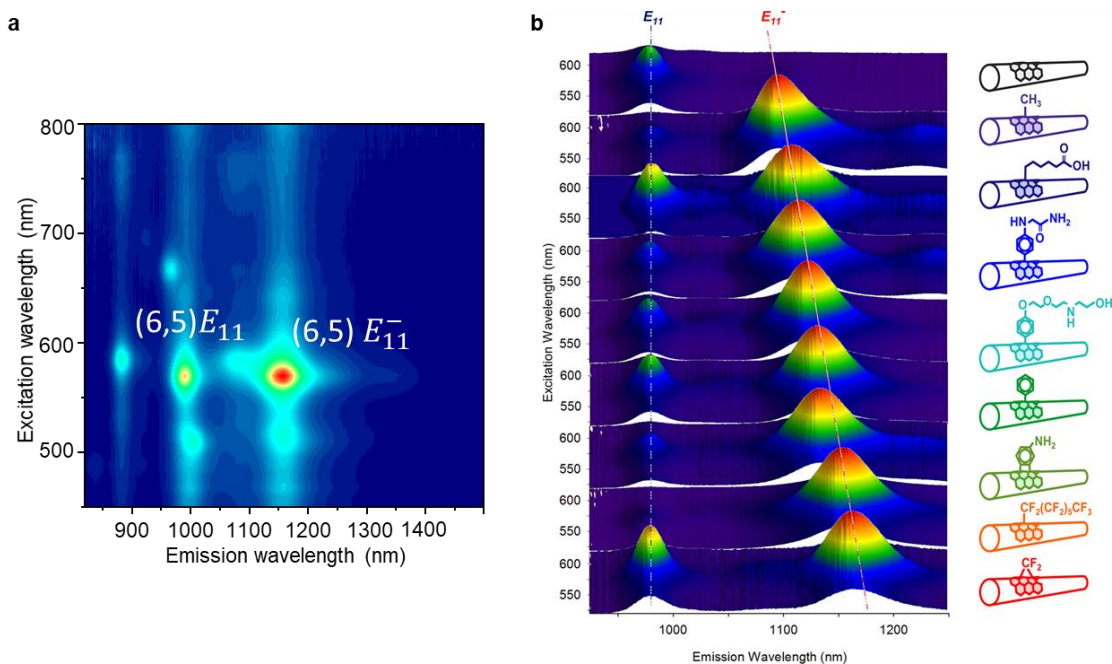
Figure 1-6. PL of OCC functionalized (6,5)-SWCNTs. a, PL excitation map of functionalized (6,5)-SWCNTs. b, Excitation–emission maps of (6,5)-SWCNTs with chemically tailored fluorescent quantum defects. Figure 1-6b adapted from ref[58].

By varying the functional groups attached to SWCNTs, the defect-induced states are molecularly specific and chemically tunable (Figure 1-6b). Therefore, it enables a family of OCCs emitting at a variety of emission and application of OCCs, such as proton sensing.[60]

1.5.1 OCCs Functionalization Methods

The controlled functionalization of OCCs on SWCNTs provides the opportunity to manipulate and tune the defect emission properties and defect density. A number of methods have been explored to generate covalent bonds to nanotubes.

A most widely studied method is to use diazonium salt, such as 4-nitrobenzenediazonium tetrafluoroborate. The mechanism behind the selective reaction is the rapid non-covalent adsorption of the diazonium molecules to the nanotubes due to their higher density of states at the Fermi level compared to other semiconducting parts, followed by a slower covalent reaction initiated by single electron transfer from SWCNTs to the diazonium salt to create a radical that readily initiates a C-C bond with the graphitic surface. The physisorption of diazonium salts on semiconducting SWCNTs induces stepwise quenching of E_{11} PL.[61] Although the quenching nature of E_{11} induced by diazonium salts have been widely recognized and studied for SWCNTs, the synthesis of OCC was recently discovered by Piao *et al.*[59, 62] When the defect density is as low as 0.33 mol% [Diazonium]:[C], corresponding to approximately < 1 OCC per 20 nm length, the average defect spacing is comparable to or slightly shorter than the exciton diffusion length.

Diazoether chemistry was also used to covalently functionalized nanotubes with the diazoether molecules (3-*O*-4-nitrobenzenediazoascorbic acid; NO$_2$Ar-DZE) to produce 4-nitroaryl OCCs.[63] DZE molecules consist of an ascorbic and an aryl group that are bonded by an azo bond, thus, they can switch conformation between E and Z isomers by light or pH. In contrast to the stable E isomer which does not react with SWCNTs, the Z isomer reacts with SWCNTs at a narrow pH window of ~ 3.8 creating a covalently bonded aryl defect on the SWCNTs.

Furthermore, halides as a good leaving group can tether aryl or alkyl group and create a radial species to functionalize SWCNTs. Kwon et al. demonstrated the molecular tunability of OCCs using a simple alkyl halide chemistry.[58] This reaction

uses alkyl iodide reactant with acetonitrile and a mild reducing agent sodium dithionite to create covalent attachment of over 30 functional groups including monovalent and divalent OCCs at room temperature. The products remain stable for months. As a results OCC emissions are generated, for example (6,5)-SWCNTs can have E_{11}^- redshifted by as much as 190 meV from the native E_{11} emission. Similarly, Wu et al demonstrated the photoinduced functionalization using iodine tethered aryl groups.[64] The reaction is temperature independent, but is strongly dependent on the incident photon energy. (6,5)-SWCNTs were excited with different wavelengths of light in the presence of 4-iodobenzene, which absorbs in the UV region. When the solutions were excited at the E_{22} and E_{33} band of nanotubes, the rapid evolution of E_{11}^- occurs. Meanwhile, the creation of OCCs was not observed when excited at E_{11} due to lack of sufficient photon energy to overcome the reaction activation barrier. This suggests a single electron transfer from SWCNTs to the physiosorbed aryl halide, creating a benzene radical and iodine anion. The radical can bond to the nanotubes, thus creating an OCC on the SWCNTs.

Among this organic synthesis, the mechanism is an addition reaction to the C-C double bonds and the asymmetric sp^2 carbon lattice. The resulting covalent products would result in at least 6 different isomers called bonding configurations. For example, diazonium chemistry, the most widely used approach for generating OCCs,[59, 62, 65, 66] is believed to leave a reactive carbon at either the adjacent (ortho) positions or three carbons away (para) from the first bonding carbon.[67] These reactive species then presumably bond to an available H or OH group to complete the reaction.[20, 67] This pair of functional groups may take one of many possible positions on the sp^2 carbon lattice,

resulting in a large number of bonding configurations that are chemically, thermodynamically, and energetically distinct.[20, 68, 69] As a result, multiple OCC emission peaks are observed when carbon nanotubes, such as (6,5)-SWCNTs, are modified with diazonium chemistry, producing a broad distribution of OCC emission peaks in the range of 1100–1350 nm, even for the same functional groups on the same (6,5) chirality.[70]

To deal with the complex bonding configuration, I proposed a naming convention to describe the rich structures afforded by these quantum defects, particularly OCC defect pairs. This naming system is inspired by the Miller index-like description of the sp^2 carbon lattice, which is widely used to distinguish the different (n,m) chiralities of tubular structures, such as carbon nanotubes and hexagonal boron nitride nanotubes, as well as graphene ribbons.[71] I define the position of the first defect as the origin, (0,0). The atomic configuration of an OCC can then be uniquely determined by the pairing position, PP(x,y), which follows $\overrightarrow{PP(x, y)} = x \overrightarrow{a_1} + y \overrightarrow{a_2}$, where $\overrightarrow{a_1}$ and $\overrightarrow{a_2}$ are the two base vectors for the sp^2 carbon lattice. With this naming system, one can identify each of the para and ortho defects, and any other atomic configuration, for a specific nanotube host. For example, an "ortho" defect can actually take up to three distinct atomic configurations, which can be differentiated as PP(1/3, 1/3), PP(1/3, -2/3), and PP(-2/3, 1/3) on a (6,5)-SWCNT host (Figure 1-7). Similarly, the "para" configurations[72, 73] include PP(4/3, -2/3), PP(-2/3, -2/3), and PP(-2/3, 4/3). This naming system can be readily expanded to associate each atomic bonding position with the specific functional group along with the chirality of the nanotube host. A comparison of our naming system and existing ones[20, 68] is shown in Table 1-1. I note

that such a rich structural variability may also occur with other low dimensional materials such as transition metal dichalcogenides and graphene ribbons,[74-76] and this naming system can similarly be applied to this increasingly rich family of atomic defects on different hosts.

Table 1-1. Comparison among different OCC nomenclatures reported in the literature for each bonding configuration on (6,5)-SWCNTs.

Coordinate Nomenclature	Notation Nomenclature[20]	Chiral Angle-based Nomenclature[68]
PP(1/3, -2/3)	ortho+	Ortho L_{30}
PP(-2/3, 1/3)	ortho-	Ortho L_{-30}
PP(1/3, 1/3)	ortho++	Ortho L_{90}
PP(-2/3, 4/3)	para+	Para L_{30}
PP(4/3, -2/3)	para-	Para L_{-30}
PP(-2/3, -2/3)	para++	Para L_{90}
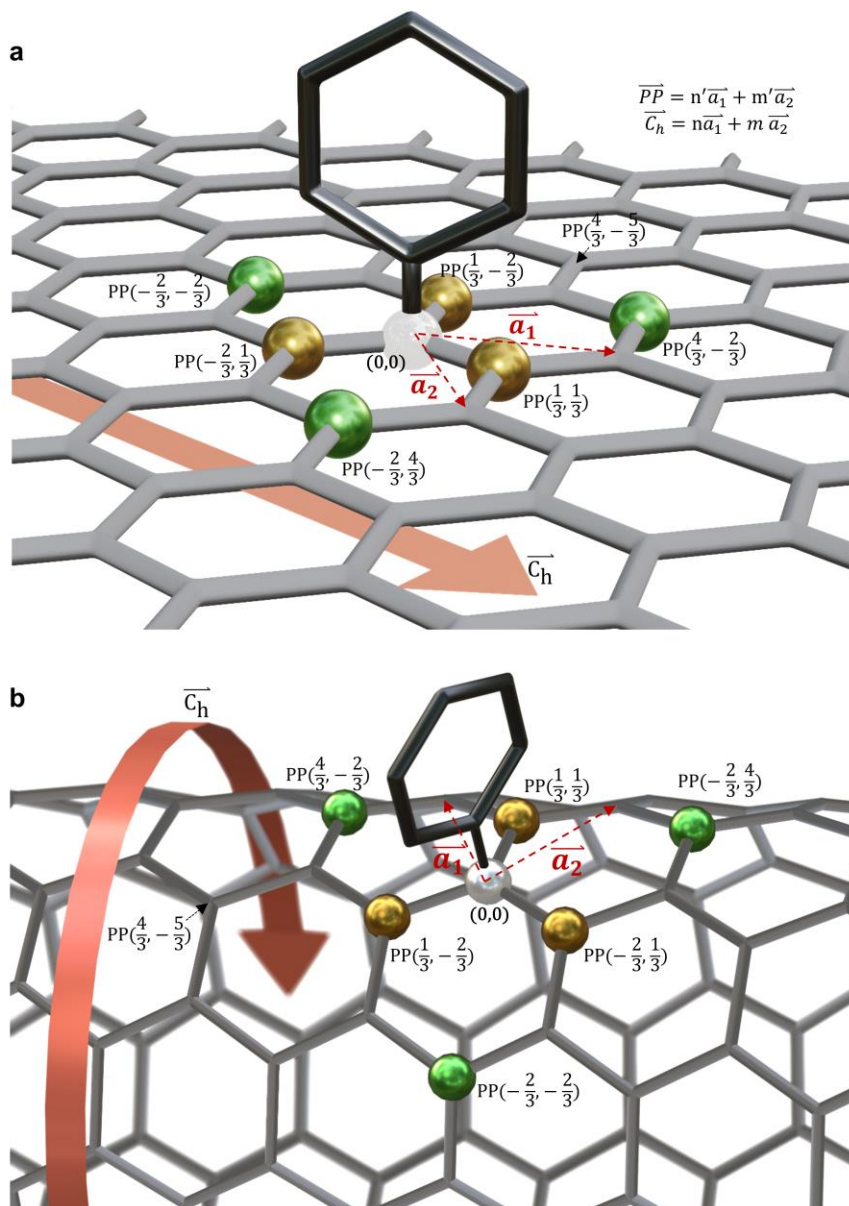
Figure 1-7. A naming system for the rich OCC bonding configurations. a, A graphene sheet with an OCC that contains a pair of covalently attached functional groups. The bonding site for the first group (-C_6H_5 here) is defined as the origin of this coordinate system, and the carbon (gold and green atoms) for bonding the pairing group (H or -OH, not shown here) is defined by the pairing position ($PP(n', m')$). The corresponding pairing position vector is defined by $\overrightarrow{PP} = n'\overrightarrow{a_1} + m'\overrightarrow{a_2}$, where $\overrightarrow{a_1}$ and $\overrightarrow{a_2}$ are the two basis vectors for the hexagonal sp^2 carbon lattice. The chiral vector $\overrightarrow{C_h} = n\overrightarrow{a_1} + m\overrightarrow{a_2}$ for the nanotube host is also shown. b, The molecular model for an OCC-tailored (6,5)-SWCNT which is rolled up from the graphene following the chiral vector $\overrightarrow{C_h}$ in a. The pairing positions for the "ortho" configurations (green), including PP(1/3, -2/3), PP(-2/3, 1/3), and PP(1/3, 1/3), and the "para" configurations (gold), including PP(4/3, -2/3), PP(-2/3, -2/3), and PP(-2/3, 4/3), are indicated on the lattice.

17

1.6   Overview of This Dissertation

This dissertation demonstrates an application of SWCNTs for molecular sieving and address challenges pertaining to controlled synthesis of OCCs.

Following this introduction, Chapter 2 describes a single-defect imaging system that we custom built to achieve super-resolved hyperspectral imaging in the shortwave infrared where SWCNTs and OCCs emit.

In Chapter 3, I introduce the environmentally sensitive optical properties that can be used for sensing molecules that become encapsulated inside SWCNTs which can affect the emission. I explored the application of molecular sieve using (6,5)-SWCNTs to purify liquid mixture. The work also reveals the fundamental mechanism behind molecules entering nanopores that are smaller than the filling molecules.

In Chapter 4, I discuss the spectral heterogeneity of OCC emissions that arise from the different bonding configurations on the sp^2 carbon lattice. This work explores the non-destructive light irradiation method that tunes the heterogeneous emission of OCCs by converting the kinetic OCCs to thermodynamic OCCs. Chapter 4 describes an alternative way to deal with the OCC emission heterogeneity by introducing a [2+2] cycloaddition chemistry to create OCCs. My work shows that this functionalization mechanism greatly reduces the number of configurations compared to monovalent OCC chemistries.

Finally, in the Conclusion and Outlook, I summarize the work discussed in this dissertation and propose further improvements that can be performed to narrow down the OCC emissions.

2 Single-Defect Spectroscopy in the Shortwave Infrared

This chapter is adapted from the following published manuscript: Wu, X.; Kim, M.;

Qu, H.; Wang, Y. Single-Defect Spectroscopy in the Shortwave Infrared. Nat.

Commun. 2019, 10, 2672.

Y.H.W. conceived the experiments and supervised the project; X.W., M.K., and H.Q.

performed the measurements; X.W. analyzed the results; X.W. and Y.H.W. wrote the

paper with inputs from all authors.

2.1 Introduction

Chemical defects are nearly ubiquitous in low-dimensional materials. However, their roles are largely unknown[77-80]. The challenges are primarily due to the small footprint of these defects and the extended lattice of the solid substrate, which make the task of finding a defect like searching for a needle in a haystack. Additionally, defects may occur in random clusters that are indistinguishable from each other or they may present in different atomic configurations, each of which modifies the host to a different degree[20, 79, 81, 82]. The ability to study defects at the single defect limit will circumvent the limitations imposed by ensemble averaging and unravel the roles of defects on the chemical, optical, and electronic properties of a material[77, 80].

The shortwave infrared (typically 900 – 1700 nm, but may also refer to 1–3 μm) is a spectral window that presents exciting opportunities for bioimaging[83, 84], telecommunication[85], and quantum technologies[86, 87]. For instance, optical-fiber-based quantum communications require single photon sources that emit in the telecom bands

(1260–1625 nm)[85, 88]. Color centers (emissive point defects in crystal lattices) that emit light in the shortwave IR are also important for non-invasive *in vivo* fluorescent imaging[83, 89]. The deep penetration of shortwave IR light in living tissue[90], as well as the negligible tissue autofluorescence within this optical window[91], offers enhanced resolution and contrast[92, 93]. Although spectroscopic studies of individual color centers in the visible range have been reported[94, 95], single defect spectroscopy in the shortwave IR is challenging due to the diffraction limit, which is approximately half of the wavelength of the emitted light, and indium gallium arsenide (InGaAs) detectors, which are noisy for low-light measurements[96, 97]. Additionally, the throughput of existing methods is typically low because the sample is scanned point-by-point.

Here I show it is possible to perform high throughput single-defect spectroscopy in the shortwave IR to spectrally identify and quantitatively count chemical defects at the single defect level. I show that nondestructive readout and cooling the InGaAs detector array to -190 °C (*vs.* -100 °C typical of liquid-N_2 cooled detectors) collectively improve the signal-to-noise ratio by more than three orders-of-magnitude. I have also designed a Si-based fiduciary marker that works in the shortwave IR to correct the stage drift at a resolution of 5 nm. As an illustration of this high-resolution high throughput single defect spectroscopy method, I show it is possible to simultaneously resolve chemical defects in carbon nanotube semiconductors at the single defect limit, collecting a full spectrum for each defect within the entire field of view.

2.2 Results and Discussion

2.2.1 *Counting chemical defects*

Our strategy for counting defects is based on quantitative analysis of the stochastic blinking of defect photoluminescence (PL). I hypothesize for an emitting site that contains only one defect, photoluminescence blinks on and off at a constant intensity step (Figure 2-1a and b). If multiple defects are present at an emitting site, the PL time trajectory will have a variable number of intensity states and multiple step sizes depending on the number of defects present. For example, when three defects are blinking independently, they will collectively produce four PL intensity states and three step sizes (Figure 2-1c and d). Although less likely, adjacent defects may blink in a correlated manner, such that two or more defects are turned on or off in synchrony. However, I can retrieve the defect locations in a manner equivalent to the super-resolution approach used in stochastic optical reconstruction microscopy[98]. By analyzing the two-state nature of fluorescence blinking from a single-defect emitting site in correlation with its super-resolved location, I can optically identify single defects. This approach, when combined with the hyperspectral capabilities of our imaging system, makes it possible to study emissive defects at the single defect level.
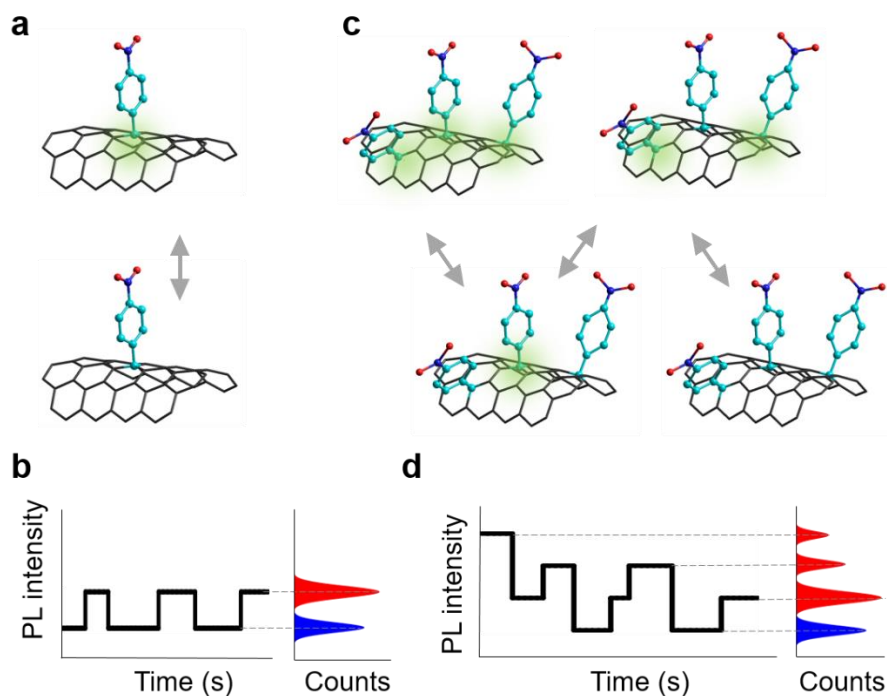
Figure 2-1. Counting defects based on photoluminescence (PL) blinking. a, Schematic illustration of a single chemical defect that switches between PL on (green shade) and off states due to surface charges. The gray arrows represent reversible PL state switching. b, The illustration of PL intensity time trajectory (black solid line) and histogram from a single defect features two states, PL on and off. The red and blue bells in the histogram represent the distribution of PL intensity of on and off states respectively. Dashed lines are added as a guide to the eye. c, For a cluster of defects, each defect randomly turns on and off. d, The stochastic blinking of clustered defect PL is collectively shown as multiple intensity steps.

2.2.2 *Super-resolved hyperspectral imaging system*

To perform single defect spectroscopy in the shortwave IR, I custom-built a super-resolved hyperspectral imaging system that allows the acquisition of PL spectra from all pixels in the camera frame simultaneously (Figure 2-2a). To achieve this, a volume Bragg grating is placed in front of the detector on the light path and an image stack is collected, one wavelength at a time, and reconstructed to provide the PL spectrum for each pixel over the entire field of view (see Methods section). This grating can be bypassed so the system can be switched between the spectrum mode and the

22

imaging mode. In imaging mode, the stochastic blinking of defect emissions is recorded

and analyzed to super-resolve defect locations[96]. The team can thus spectrally and

spatially resolve the same defects at the single defect level by simultaneous super-

resolution and hyperspectral imaging.
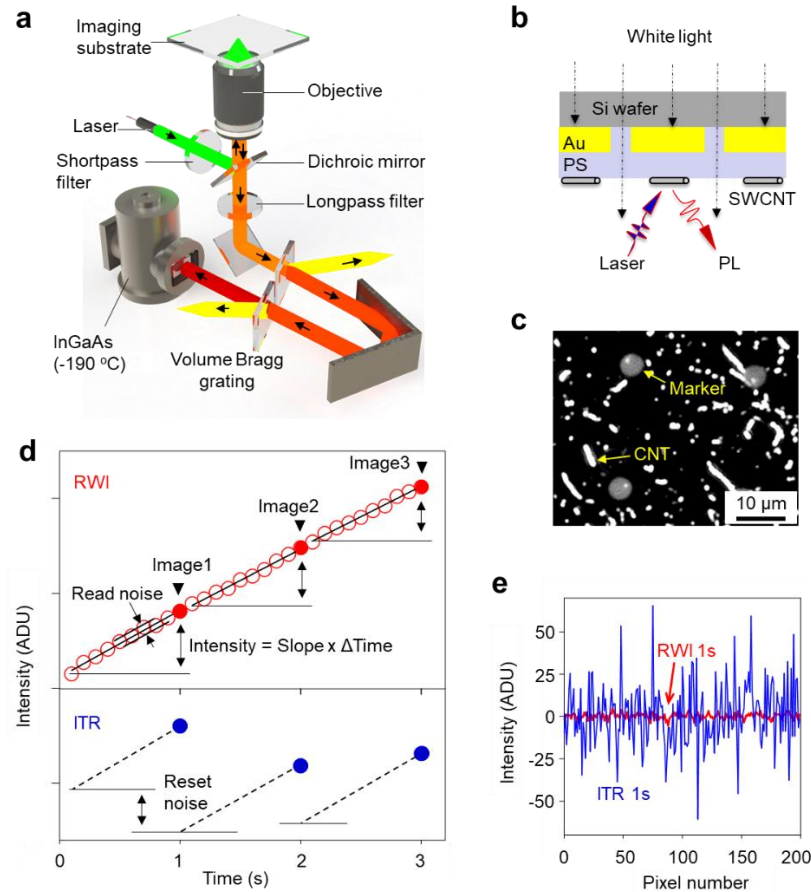
Figure 2-2. Single-defect spectroscopy set-up. a, Schematic of the system, which integrates a volume Bragg grating for hyperspectral imaging and an InGaAs 2D array detector that operates at -190 °C to significantly suppress the dark current in the shortwave IR. b, Schematic of the imaging substrate that incorporates Au-on-Si markers and polystyrene (PS) insulating layer for drift correction in the shortwave IR. c, A PL image with both SWCNTs and the markers simultaneously resolved. Note that nanotubes with length smaller than the diffraction limit (~600 nm for a numerical aperture 0.85 objective collecting emission at 1000 nm) appear as white dots in the image. d, The comparison of signals of the same pixel from an image sequence captured by the integrate-then-read (ITR, blue filled circles) and read-while-integrate (RWI, red empty circles) demonstrates the working principle of non-destructive RWI mode. The integration slopes for different images in ITR (dashed lines) do not have

identical starting point, caused by reset noise. Unlike ITR, RWI does not reset the detector, thus eliminating the reset noise. For each image (red filled circles) in RWI, the noise can be further suppressed by linear regression of different data points to retrieve the integration slope (black solid line). e, The comparison of background signals from images captured by the ITR (blue) and RWI (red). Under otherwise identical conditions, RWI demonstrates more than an order of magnitude lower noise level than ITR, with a standard deviation of merely 1.75 analog-digital unit (ADU) (vs. 18.5 ADU for ITR). Note that 0.168 ADU corresponds to one photon arriving at the detector.
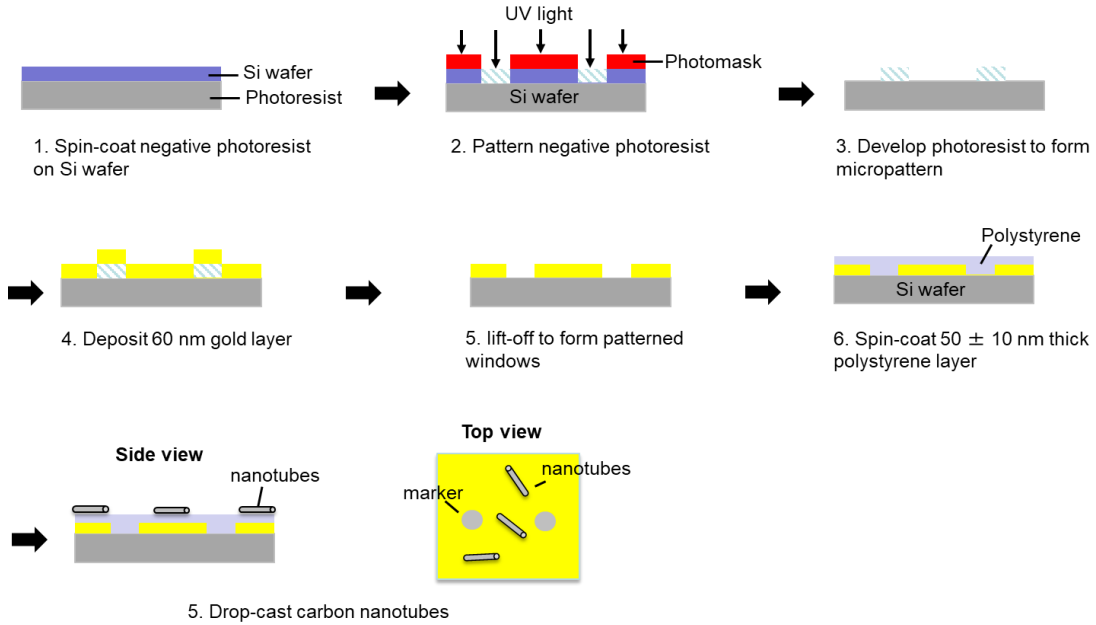
Figure 2-3. Schematic for photolithographic fabrication of the imaging substrate that contains fiduciary markers for sample drift correction in the shortwave infrared.

Additionally, we have developed a drift correction method that works in the shortwave IR. Although fiduciary markers, such as fluorescent beads immobilized on the sample substrate[99], have been used to correct stage drifts, they work only in the visible range. Our design makes use of silicon, which is transparent in the shortwave IR since its bandgap absorption cuts off at 1100 nm, to directly create shortwave IR markers on the imaging substrate. The markers used in this experiment are 5 µm diameter dots of shortwave IR-transparent windows, which are patterned at a pitch of 30 µm on a silicon wafer by photolithography, with Au covering the rest of the substrate

24

(Figure 2-2b and Figure 2-3). This design results in a photomask-like structure allowing the shortwave IR component of the microscope's halogen lamp to transmit through the patterned Si dots to create bright markers while the visible component is blocked by the silicon (Figure 2-2b). The Au layer concomitantly acts as a mirror to enhance the collection efficiency of photons emitting from the sample while blocking the fluorescence from the underlying silicon substrate. To prevent photoluminescence quenching by Au, a ~50 nm thick polystyrene (PS) layer was spin-coated on top of the Au layer. With this substrate design the collection efficiency of the nanotube PL is ~5-times higher than when imaged on bare glass (Figure 2-4). This observed increase can be attributed to the reflective gold layer acting as a mirror to enhance both the absorption of excitation photons by the carbon nanotubes and the collection efficiency of emission photons by the objective, as well as the PS layer, which minimizes surface charges that would otherwise quench the PL. Figure 2-2c shows the markers simultaneously resolved along with single-walled carbon nanotubes (SWCNTs) by the InGaAs camera. I fit the intensity profile of each individual dot marker with a 2D Gaussian to locate its center (Figure 2-5c), and this process was repeated for all imaging frames in a time sequence, allowing us to plot the sample drift trajectory (Figure 2-5d and e). The standard deviation of an individual drift trajectory from the averaged one defines the precision of this drift correction, which I determined to be 5 nm (Figure 2-5f). We note that to achieve 5-nm drift correction precision, we ensured there were at least 5 markers in the field of view.
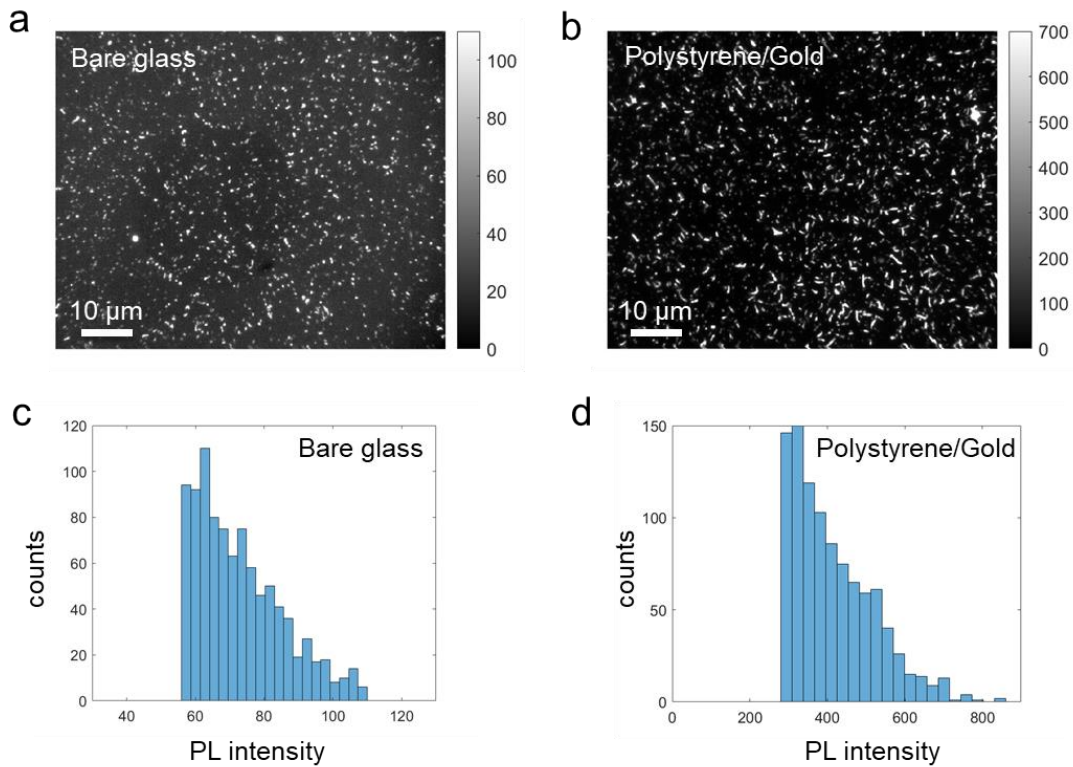
Figure 2-4. The polystyrene/gold (PS/Au) substrate increased the PL intensity by ca. 5-fold. PL images of SWCNTs on (a) bare glass and (b) the PS/Au substrate. The excitation wavelength was 730 nm and the integration time was 2 s. The color bar is the PL intensity ADU count. (c, d) The corresponding histograms of the SWCNT PL intensity distribution based on the PL images shown in (a) and (b).
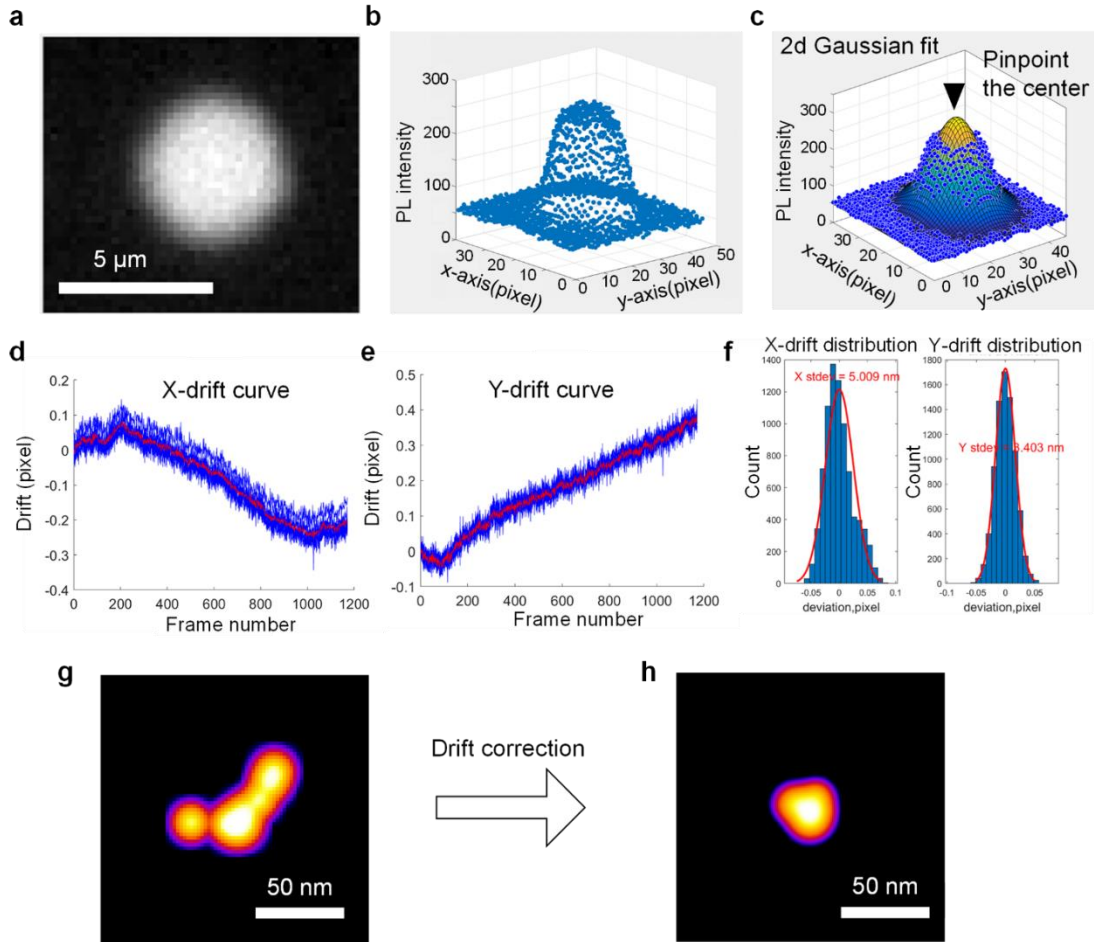
Figure 2-5. Proposed mechanism for drift correction in the shortwave infrared. a, The PL image, b, intensity profile, and c, center position of an individual fiduciary marker. Note the center position is located by fitting the intensity profile with a 2D Gaussian. This process was repeated for all frames in a time sequence, allowing us to plot the center positions versus time and construct a trajectory of the corresponding sample drift in the d, X and e, Y directions. At least five such trajectories (blue in d and e) from different markers in the same field of view were averaged together (red in d and e) and applied to correct the sub-pixel stage drift. f, The drift curve of an individual marker. The standard deviation from the averaged one defines the precision of this drift correction, which is determined to be 5 nm. Example of super-resolved defect locations g, before and h, after the drift correction using the obtained average X and Y sample drift trajectories.

To detect extremely low light stemming from individual defects in the shortwave IR, we integrated a liquid nitrogen cooled InGaAs detector array (Cougar 640) that is optimized for -190 °C operation. Note that liquid-N_2 cooled InGaAs

detectors are typically operated at temperatures no lower than -100 °C. Cooling down

to nearly the true liquid-N_2 temperature suppresses the dark current to just 10 e$^-$ pixel^{-1}

s^{-1}, which is 500 times lower than achievable by InGaAs detectors cooled to -100 °C.

Another enabling feature of our system is the implementation of a read-while-

integrate (RWI) readout mode, which significantly reduces the read noise. Unlike the

conventional integrate-then-read (ITR) mode, RWI is non-destructive, which

eliminates the reset and read noise. Figure 2-2d compares the signals of the same pixel

from an image sequence captured by the two modes to demonstrate the working

principle of RWI. In the RWI mode, the signal is read without resetting the detector

while the ITR mode resets after each signal readout. Since the pixel is reset to a slightly

different value each time, this causes significant reset noise in ITR (Figure 2-2d). This

reset noise is effectively removed in the RWI mode since the reset is avoided. The noise

in RWI can be further suppressed by linear regression to eliminate the read noise. For

each image, I accumulate n readouts, from which the slope of every pixel is calculated

by

$$\alpha = \left[\frac{n\sum(xy) - \sum x \sum y}{n\sum x^2 - (\sum x)^2}\right]$$ Equation 2-1

where x is the readout count and y the readout value. I then multiply the

calculated slope α with the total number of accumulated readouts n for each pixel (i.e.,

$Pixel = n\,\alpha$) to obtain the signal intensity. The effect of the RWI mode on reducing

the image noise is dramatic, increasing the signal-to-noise ratio by more than 10 times

(Figure 2-2e). The clean background significantly improves the image contrast. Figure

2-6a and b show PL images of the same SWCNT with the same integration time (1 s)

captured in the ITR and RWI modes, respectively. The nanotube is clearly resolved in

28

RWI but almost invisible in ITR. The much higher image contrast in RWI is due to a

much lower noise level while maintaining the signal intensity, as shown in the intensity

profile (Figure 2-6c).
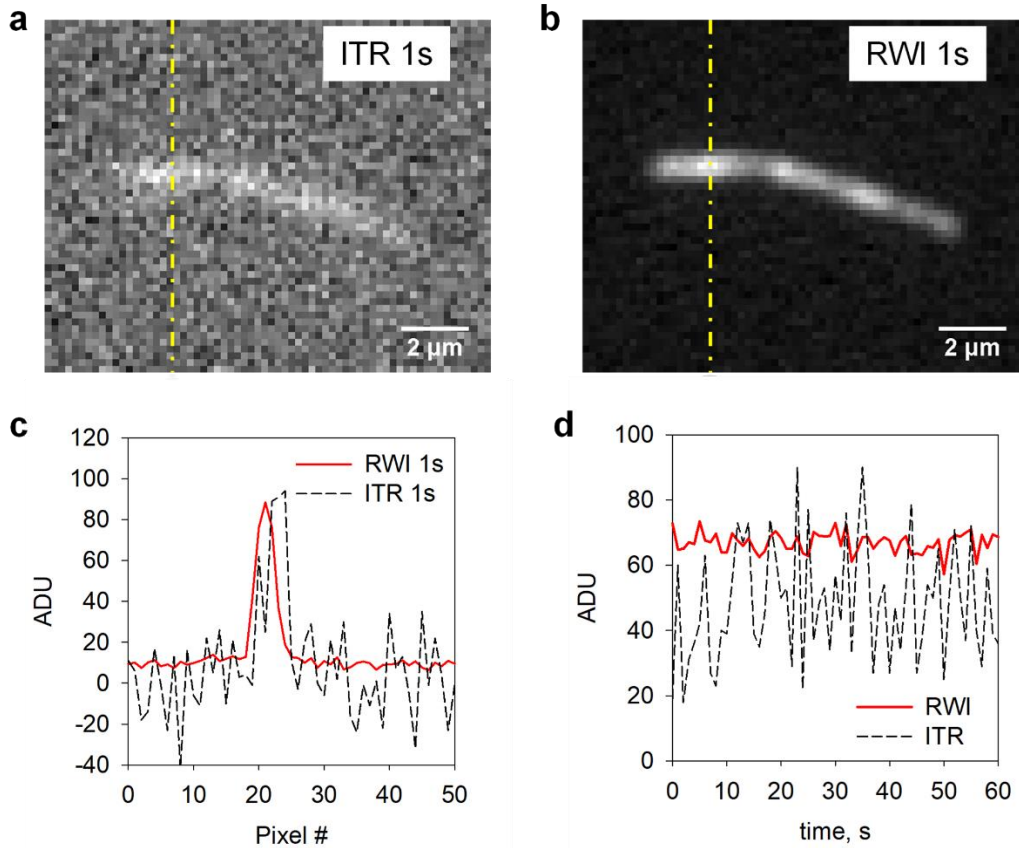
Figure 2-6. Non-destructive readout improves the signal-to-noise ratio in the shortwave IR. PL images of the same SWCNT taken in the a, ITR mode and the b, RWI mode with 1 s integration time. c, PL intensity profiles along the yellow line in (a) and (b) show much higher signal-to-noise ratio in the RWI mode (red) compared to the ITR mode (black). d, The PL time trajectory from the same pixel on the nanotube as shown in (a) and (b), which demonstrates nearly 8-times less fluctuation in intensity, with a standard deviation of 2.6 ADU (vs. 20.1 ADU for ITR).

The RWI mode also greatly reduces the background signal fluctuation over time

in an image sequence. RWI is a continuous readout mode (Figure 2-2d), which reads

the accumulated signal at a preset time interval. In order to capture the PL time

trajectory, I recorded the luminescence image sequence at 2 frames per second and then computed the difference between two adjacent images in the readout sequence (which accumulate the signal from time zero up to the point of each readout) using MATLAB codes to obtain the time-lapse images at equal time intervals. Figure 2-6d shows a 60 s intensity trajectory of the same pixel taken using the RWI and ITR modes under the otherwise same conditions. RWI demonstrates a background fluctuation significantly lower than the ITR mode, providing the sensitivity required to probe the defect PL fluctuation in a time sequence.

2.2.3   *Characterization of organic color-centers*

As an illustration of this high sensitivity single defect spectroscopy, I characterized organic color-centers which are synthetic defects chemically incorporated into SWCNTs by covalently bonding functional groups to the sidewalls[58, 59, 100, 101]. The introduced chemical defect locally modulates the electronic structure of the SWCNT in such a way that mobile excitons can become trapped at the defect site where they emit brightly as single photons in the shortwave IR[77, 80,86, 87]. I excited the sample at an off-resonant wavelength at low power densities (below 64 W cm^{-2}) to avoid exciton-exciton annihilation effects[102]. I find that the defect emission is highly localized (Figure 2-7a) and the defect emission shows stochastic PL intensity changes. This PL blinking can be suppressed when the SWCNT is sandwiched between two layers of polystyrene, which form a charge-free environment[103], confirming surface charges as the cause of blinking. This intermittency in defect emission enables us to identify single defects by analyzing the PL intensity time trajectory from a defect emitting site. Figure 2-7c shows the PL intensity trajectories acquired over 10 minutes,

30

revealing the presence of multiple intensity states for the emitting defect sites marked in Figure 2-7a. I quantified the number of intensity states by analyzing the PL intensity distribution, presented as a histogram in Figure 3d, which is bimodal for (i) and (ii), but trimodal in (iii). Although the defect emitting sites in all 3 cases appear as similar diffraction-limited spots, the PL intensity time trajectories are bimodal *vs.* trimodal, which are characteristic of one (vs. two) emitting centers in those sites. I note that the majority (>80%) of defect emitting sites observed in the current study show multiple intensity steps, indicating the prevalence of clustered defects.
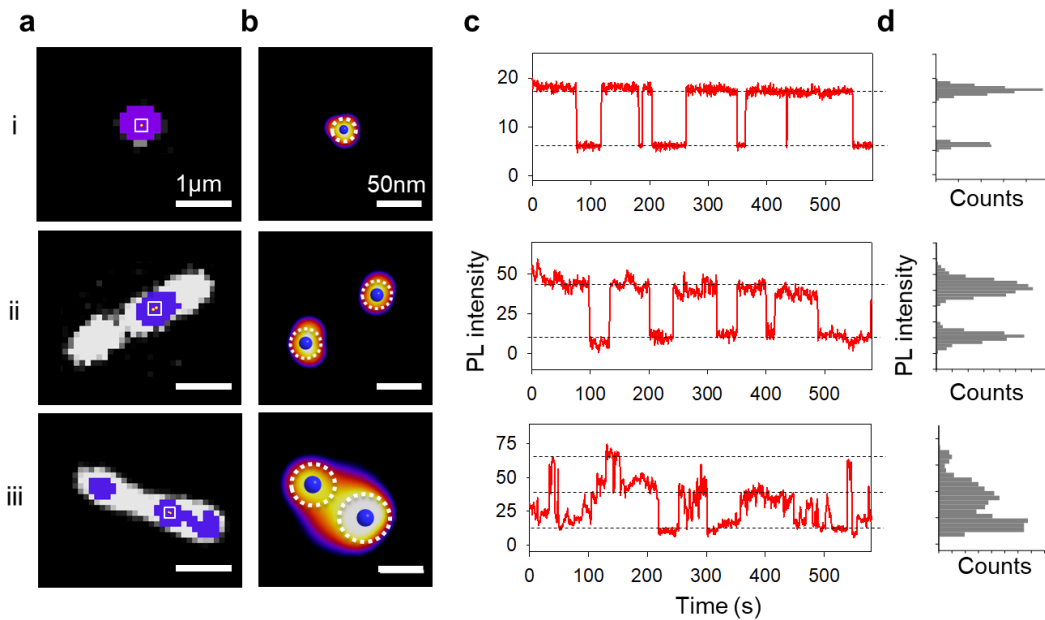
Figure 2-7. Super-localization and PL blinking of individual 4-nitroaryl defects. Note that the images on the same row are associated with the same defect sites. a, The diffraction limited PL images of the defect emission sites (blue) and intrinsic E_{11} exciton emission (white) reveal the localized nature of the defects along the nanotube length. b, Individual defects within those emitting sites marked in (a, white square) are resolved with sub-pixel resolution. Here, individual defect localization is displayed as blue spots with the corresponding localization precision as dotted circles. c, PL intensity trajectories (red solid line) from each defect emitting sites reveal stochastic blinking behavior and d, the corresponding PL intensity histograms show bimodal (i) and (ii), and trimodal (iii) intensity states. Dashed lines are added as a guide to the eye.

To spatially resolve defects within a cluster, I retrieved the defect locations by fitting the differential images (between successive images before and after each PL blinking event), as we have previously shown to super-resolve ultrashort nanotubes[96], with a Gaussian approximation of the point spread function of our setup. Since each differential image represents the appearance or disappearance of the PL stemming from a defect within a cluster, I can compute and compare the locations of defects to determine the number of defects at the limit of the localization precision. Figure 2-7b shows the defect localizations for several emitting defect sites marked in Figure 2-7a. Here, individual defect localization is displayed as blue spots with the corresponding localization precision as dotted circles. Note that each localization has different localization precision, determined following a literature method[98, 104], and the localization precision is as high as 15 nm in our experiments. The localization confirms the presence of only one single defect at emitting site (i) and two defects at (iii), which are in consistent with their PL blinking behavior.

Unexpectedly, I identified two defects from emitting site (ii) even though the PL from this site shows two-state blinking. In addition, the PL time trajectory of (ii) shows blinking at step heights that are quantitatively correlated with two defects. This observation suggests the two defects are strongly coupled, manifesting as a two-state on and off mode just like a single defect. This correlation makes it possible to distinguish independent defects from coupled defects that are in very close proximity to each other. This technique suggests the possibility of quantitatively measuring the coupling effect of two or more closely spaced defects. We note that this coupling effect

was observed only occasionally (~5%) in the current study and will be further exploited in future experiments.

I further showed it is possible to address the outstanding challenge of unambiguously determining the chemical nature of defects at the single defect level[20, 81, 105]. To demonstrate this possibility, I synthesized (6,5)-SWCNTs containing two types of defects: methoxyaryl (MeOAr-) and nitroaryl (NO$_2$Ar-) (Figure 2-8). Figure 4a shows a PL image with the defect locations super-resolved (Figure 2-8a). Note that the defects are located inhomogeneously along the nanotube length. I then plotted the PL spectra from each pixel along the tube length in a spatially and spectrally correlated map with the defect PL resolved (Figure 2-8b). From this particular nanotube, we identified three defect emitting sites with overlapping defect emission spectra but distinct center wavelengths, spatially corresponding to the three super-resolved defect groups in Figure 2-8a. By comparing these results with the spectra of isolated defects (Figure 2-8c), we can unambiguously assign each defect as (i) nitroaryl defects; (ii) methoxyaryl defects; and (iii) both. I note that the two defects at site iii show a 5~6 meV redshift in emission energy compared to the corresponding defects at sites i and ii. This shift is relatively small compared to the energy difference between these two types of defects (~19 meV)[101] and was also observed in the E$_{11}$ emission (Figure 2-9). This behavior may arise from coupling between neighboring defects or the different local dielectric environment caused by inhomogeneous surfactant coverage on the nanotube surface[106] or the partial filling of water inside the SWCNT[33]. Further studies are warranted to understand and quantify these different effects.
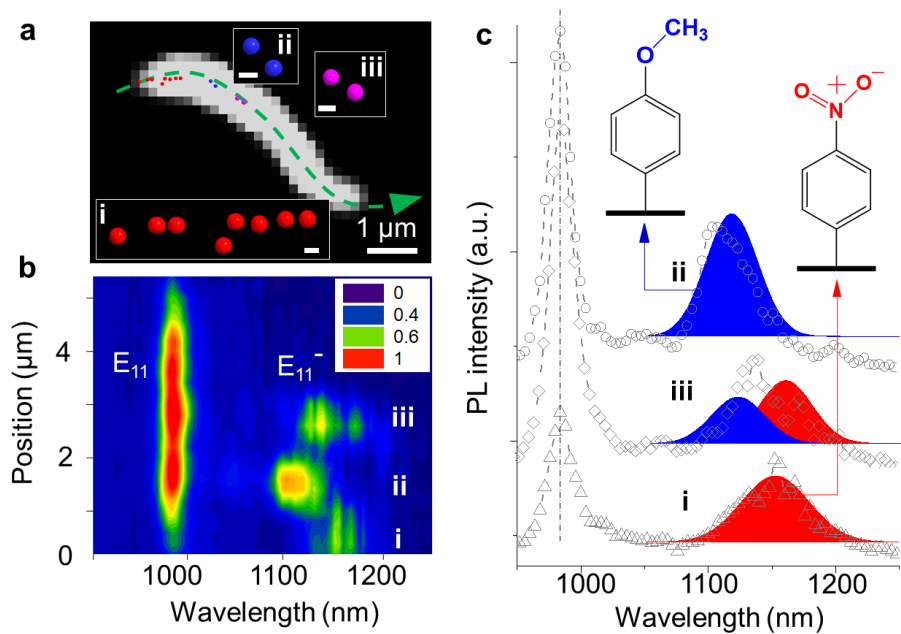
Figure 2-8. Resolving and identifying two types of defects along a nanotube. a, The super-resolved defect locations superimposed on the E_{11} emission of a (6,5)-SWCNT. Three major defect groups can be found. The insets are close looks of the resolved defect locations from these three defect groups. Red, blue and magenta represent 4-nitroaryl, 4-methoxyaryl and mix of the two defect types, respectively (scale bar 100 nm). b, Spatially and spectrally correlated PL map along the nanotube centerline as indicated by the green dashed line in (a). The y-axis represents the physical positions on the centerline, starting from the left nanotube end. Three defect sites with emission wavelengths in the range of 1080 to 1200 nm can be identified, which spatially correspond to the three super-resolved defect groups in (a). c, PL spectra from the 3 identified defect sites. Site i and ii are 4-nitroaryl and 4-methoxyaryl defects, respectively, and site iii contains both.

34
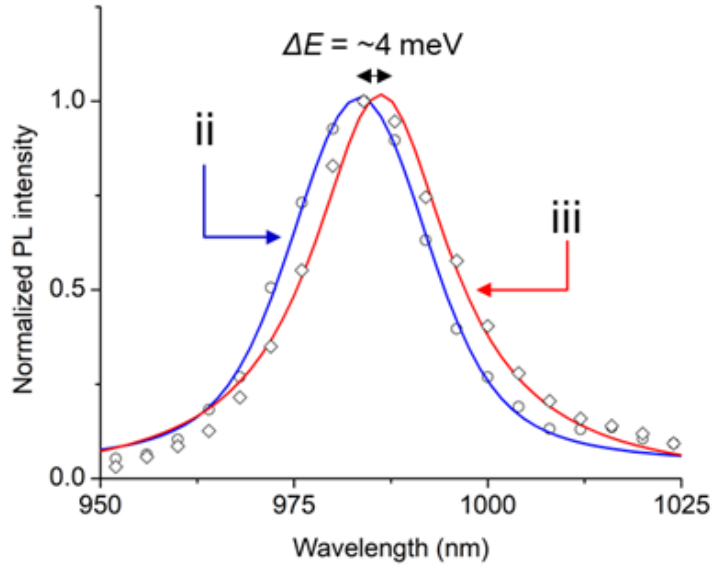
Figure 2-9. The normalized PL spectra of a (6,5)-SWCNT with two types of defects, methoxyaryl and nitroaryl. The E_{11} emission of at site iii has a 4 meV redshift from that of site ii.

2.3 Conclusions

In summary, I have demonstrated a super-resolved hyperspectral imaging technique capable of performing high-throughput single-defect spectroscopy in the shortwave infrared. Distinct from conventional single point spectroscopy, which requires point-by-point scanning, our method allows all 640×512 pixels of an InGaAs detector array to simultaneously acquire a full PL spectrum to achieve hyperspectral function. Notably, by cooling the detector array to nearly the true liquid-nitrogen temperature (-190 $^\circ$C *vs.* -100 $^\circ$C) and implementing a non-destructive readout scheme, I reduced the dark current by nearly 500-fold and achieved another 10-times improvement in the signal-to-noise ratio due to the low-noise readout, collectively improving the signal-to-noise ratio by more than three orders-of-magnitude. Additionally, I have designed a fiduciary marker that works in the shortwave IR to achieve a correction precision as high as 5 nm. As an illustration of this super-resolved

35

hyperspectral imaging technique, I resolved individual chemical defects, both spatially and spectrally, along SWCNT semiconductor hosts. I show it is possible to capture low light fluorescent events at the single emissive defects, allowing us to quantify the number of defects within a diffraction limited spot and spatially resolve them with a resolution of 15 nm in the shortwave infrared with simultaneous hyperspectral capabilities to unambiguously determine their chemical identities. This super-resolved hyperspectral imaging technique may open possibilities to screen shortwave IR fluorophores, resolve functionalization patterns, capture single molecule reactions, and probe chemical defects with high throughput and rich spectral details at the single defect limit.

2.4   Methods

2.4.1   The single-defect spectroscopy imaging system

The system was built on a Nikon Eclipse U inverted microscope with IR optimized objectives, including a 100x objective (LCPLN100XIR, Numerical aperture (NA) = 0.85, Olympus) and a 150x objective (UAPON150XOTIRF, NA=1.45, Olympus). A continuous wave laser beam at 730 nm (Shanghai Dream Lasers Technology Co., Ltd.) or 561 nm (Jive^{TM} Cobolt AB, Sweden) was shaped through a beam shaping module to produce a top hat profile, with the top flat part of the hat effectively overfilling the field of view on the sample surface. The laser was then reflected into the objective through a long pass dichroic mirror (875 nm edge, Semrock, USA) and focused to create a uniform excitation field on the sample surface. Fluorescent emission from the sample was collected by the same objective and filtered

through the long pass dichroic mirror to remove the photons produced by elastic laser scattering at the sample surface. The detector for the fluorescent signal was a Cougar-640 imaging camera (Xenics, Leuven, Belgium) with an InGaAs focal plane array with 640×512 pixels, cooled with liquid nitrogen to -190 °C. To perform hyperspectral imaging, a volume Bragg grating (VBG, Photon Etc., Montreal, Canada)[107] was situated between the long pass dichroic mirror and the liquid nitrogen cooled InGaAs detector array. The fluorescent signal was filtered by the VBG and only the diffracted light with a narrow bandwidth of 3.7 nm was directed to the detector to form a spectrally-filtered image. A hyperspectral cube containing a stack of images at spectral intervals of 4 nm was collected by rotating the VBG to continuously tune the diffracted wavelength. To record the defect emission blinking in the full field of view, the VBG was bypassed, where instead a 1100 nm long pass filter (Thorlabs, FELH1100) was placed between the long pass dichroic mirror and the InGaAs detector array to block the fluorescent signal from the semiconductor nanotube itself (~980 nm for (6,5)-SWCNTs) and image the defect emission only (~1150 nm). The videos of defect blinking were recorded for 10 min with a frame rate of 2-10 frames-per-second.

2.4.2 *Covalent incorporation of defects into (6,5)-SWCNTs*

Aryl defects were chemically incorporated into the nanotube structure using a light-activated diazonium reaction[62]. Briefly, we conducted the chemistry by mixing aqueous suspensions of (6,5)-SWCNTs with 4-methoxybenzenediazonium tetrafluoroborate (Sigma Aldrich, 98%) or 4-nitrobenzenediazonium tetrafluroborate (synthesized from 4-nitroaniline and nitrous acid) then irradiating the solution with 565 nm light using a Nanolog spectrometer (Horiba Jobin Yvon). The reaction was

monitored *in situ* by measuring the evolution of a new emission that originates from the created defect sites, which is red-shifted from the intrinsic nanotube emission. The reaction was terminated when the desired defect PL intensity was reached by diluting the solution to 3.2% wt/v DOC-D_2O using 4% wt/v DOC-D_2O. For (6,5)-SWCNTs containing two types of defects (MeOAr- and NO_2Ar-) a two-step reaction was performed by first reacting (6,5)-SWCNTs with 4-methxoyaryl diazonium salt and then 4-nitroaryl one. I confirmed the successful incorporation of each defect type at each step by PL spectroscopy (Figure 2-10). The pristine (6,5)-SWCNT has a characteristic E_{11} peak at ~988 nm. Reaction with 4-methxoyaryl diazonium created a new emission peak that was 155 meV lower in energy than the E_{11} peak, confirming the successful incorporation of MeOAr-defects. Following the addition of the 4-nitroaryl diazonium reactant, the intensity of this defect-related new emission peak increased while its emission energy further red-shifted to 170 meV below the E_{11} peak, as the NO_2Ar-defects become dominating the final product.
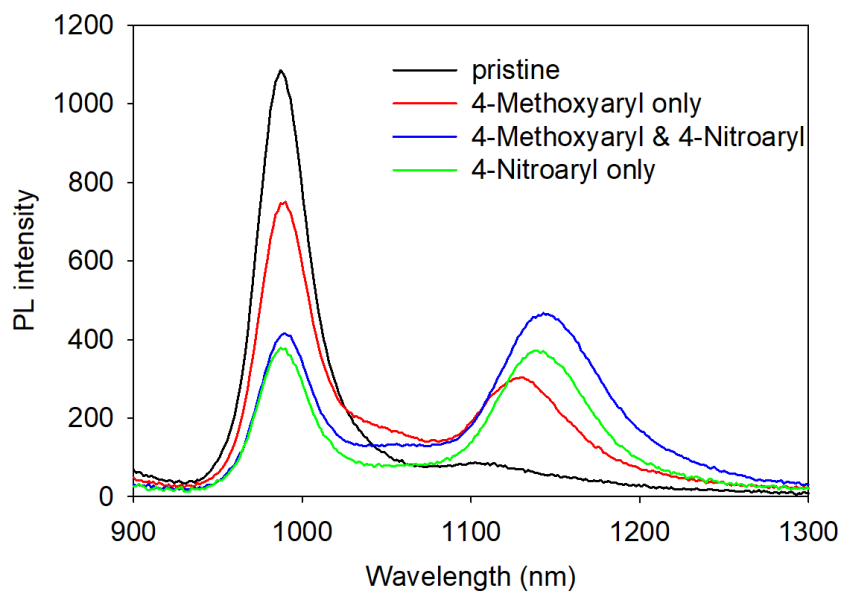
Figure 2-10. Incorporating two types of defects in the same nanotube. The ensemble level PL spectra of the pristine (6,5)-SWCNT sample (black), reacting first with 4-methxoyaryl diazonium (red), then with 4-nitroaryl diazonium (blue), and only with 4-nitroaryl diazonium (green). The excitation wavelength is 565 nm and the integration time is 3 s.

3   Selective Filling of n-Hexane in a Tight Nanopore

This chapter is adapted from the following published manuscript: Qu, H.;

Rayabharam, A.; Wu, X.; Wang, P.; Li, Y.; Fagan, J.; Aluru, N. R.; Wang, Y.,

Selective Filling of N-Hexane in a Tight Nanopore. Nat. Commun. 2021, 12, 310.

Y.H.W., H.Q., and N.R.A. conceived and directed the research. H.Q., X.W., P.W., and Y.L. performed the experiments, and J.F. sorted end-capped nanotubes. A.R. performed MD and AIMD simulations. All authors contributed to data analysis. H.Q. and Y.H.W. wrote the manuscript with inputs from all co-authors.

3.1   Introduction

Nanopores play an important role in chemical separations and selective mass transport that underlie many basic biological functions and industrial processes[108-110]. Biological systems, for example, have evolved a diverse array of specialized nanoscale protein channels that can allow only selected ions and molecules to cross the cell membrane[111]. Synthetic porous materials, such as zeolites, have also demonstrated an impressive level of molecular sieving capabilities for chemicals, allowing the separation of minor components from heterogeneous mixtures[112]. It is generally believed that the selectivity enabling such separations arises from the ability of molecules with smaller kinetic diameter (KD) to enter the pore while larger ones are excluded[113-116].

However, in examining nanopores defined by single-wall carbon nanotubes (SWCNTs), I find unambiguous evidence that molecules can adapt their conformation to enter smaller pores. The SWCNT nanopores are chemically inert, structurally rigid (Young's modulus > 1 TPa)[5], and atomically smooth cylinders, featuring inflexible pores that are well-defined by the nanotube cylinder that is constructed from a

conjugated sp^2 carbon lattice. These nanopores are tunable in size within the sub-nm range based on their individual atomic structure (i.e., nanotube chirality, as defined by a pair of integers (n,m))[117], and they exhibit intriguing molecular transport properties[118, 119]. Many of these SWCNT nanopores have a pore size comparable to small molecules. For example, (6,5)-SWCNT has a van der Waals pore size of just 0.422 nm, which is even smaller than n-hexane (KD ≈ 0.43 nm)[120, 121] and cyclohexane (KD ≈ 0.60 nm)[121, 122]. Additionally, the excitonic photoluminescence (PL) of semiconducting SWCNTs is sensitive to both the exterior and interior environments of the hollow nanotube[123, 124] due to changes in the dielectric microenvironment[125], as well as from molecule-induced strain[126].

Here, I show that n-hexane is able to enter (6,5)-SWCNT, while cyclohexane is excluded. This is despite the fact that plausible filling configurations of both molecules suggest that neither molecule should be able to enter the rigid pore when observed from the view of KD (Figure 3-1a,b). Our series of experiments further confirm that even a trace amount of 0.1 % n-hexane in 99.9 % cyclohexane can be selectively captured and removed from the mixture. In contrast, for SWCNT pores only 0.025 nm larger, both molecules are able to enter and the selectivity is lost. By capturing the optical response of the nanotube, as schematically illustrated in Figure 3-1c, and combining *ab initio* molecular dynamics simulations, I uncover a molecular level of insights for the nanopore selectivity.
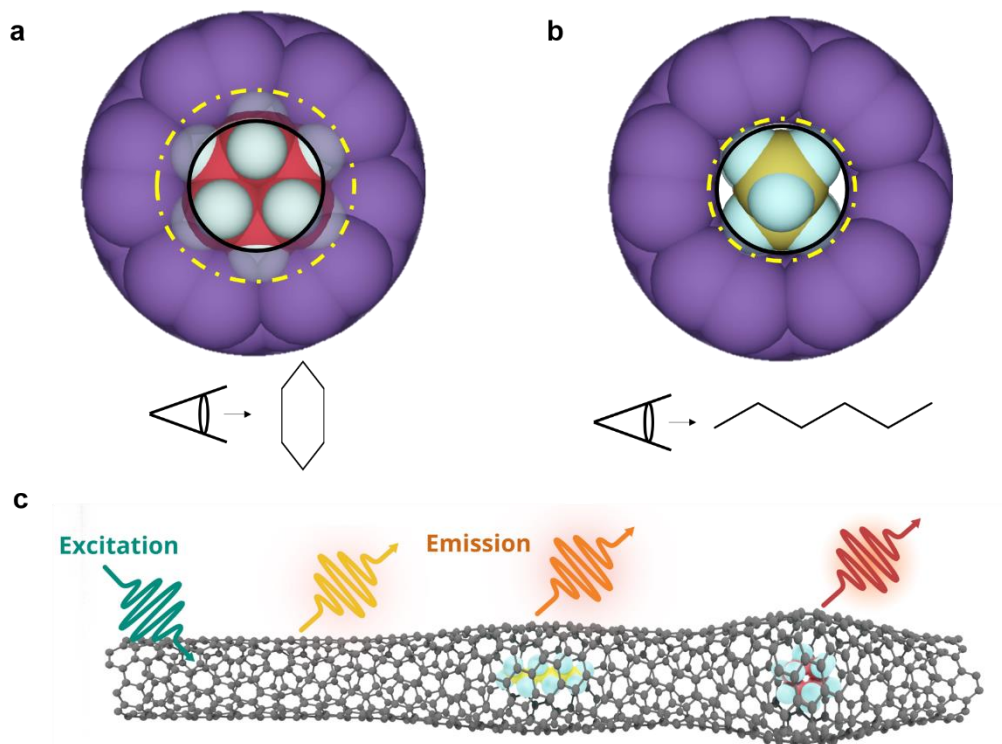
Figure 3-1. Photoluminescence response of a carbon nanotube to encapsulated molecules. Cross-sectional views of a, cyclohexane and b, n-hexane with respect to a (6,5)-SWCNT (purple cylinder). The nanotube pore (as indicated by the black circle) is smaller than the molecule (as indicated by the dashed yellow circle). c, The nanotube fluoresces at different wavelengths in response to different encapsulated molecules. The yellow arrow represents the PL emission from unfilled nanotube segments, while the PL emission from the filled positions are shifted depending on the encapsulated molecules.

3.2   Results

To prepare samples of molecule-filled SWCNTs, I first thermally oxidized the nanotubes to open their ends, and then incubated these end-opened SWCNTs in cyclohexane or n-hexane (see Methods for details). This opening step is required as the ends of raw SWCNTs are typically capped or blocked, which would prevent the molecules from entering the pore[124, 127]. I note that the nanotubes retain their structural integrity during this oxidative opening process. The amount of oxidative defects

introduced, if any, is negligible, as evidenced by the nearly unchanged Raman D/G peak ratio (Figure 3-2a) and bright PL from the end-opened nanotubes (vide infra). After exposure to either n-hexane or cyclohexane, the opened nanotubes were then stabilized as individual particles in water by the surfactant sodium deoxycholate for ensemble measurements or deposited on a substrate for single nanotube hyperspectral imaging. As controls, I prepared both empty (end-capped) SWCNTs and water-filled end-opened nanotubes. The water-filled SWCNTs are a necessary control because the particle dispersion process required to achieve individualized nanotubes is also known to cut the nanotubes shorter and cause them to fill with water[123, 127]. To prepare both controls, I dispersed end-capped SWCNTs and separated those that remained intact from the water-filled end-opened structures based on their difference in buoyant density[123, 127].
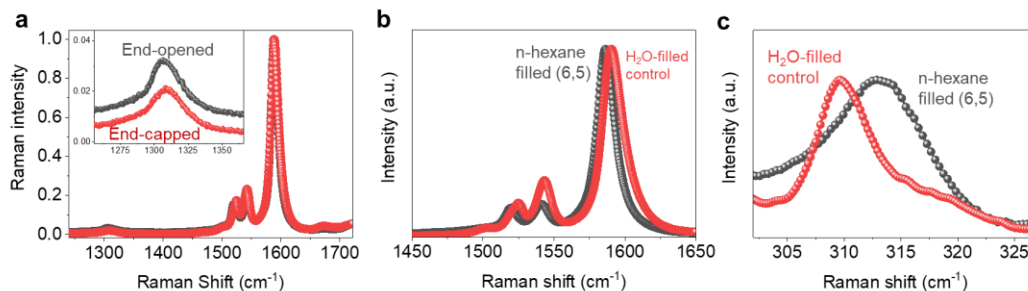
Figure 3-2. Raman spectra of n-hexane-filled (6,5)-SWCNTs in comparison with H_2O-filled and end-capped controls. a, Raman spectra for end-opened SWCNTs (black curve) and end-capped SWCNTs (red curve). b, Raman spectra of (6,5)-enriched SWCNTs that are filled with n-hexane (black curve) and H_2O (red curve). c, RBMs of the n-hexane-filled and H_2O-filled (6,5)-SWCNTs. Note that all the spectra are normalized to the G or RBM peak intensity. Note: Raman spectra were collected under 532 nm laser excitation.

43

3.2.1   Hyperspectral Imaging of Individual, Molecule-filled SWCNTs

I confirmed molecular filling by comparing the nanotube PL for the n-hexane exposed samples against both the empty and water-filled nanotube controls. Using hyperspectral imaging[128, 129], I directly measured and mapped the PL response along the lengths of individual nanotubes. I then fit the spectrum captured on each detector pixel with a Gaussian function (see Supplementary note 3-1 and Figure 3-3) and plot the peak PL emission wavelength as a pseudo-colored map along with the intensity image (Figure 3-4a, b). Generally, hexane-filled (6,5)-SWCNTs emit at ≈ 998 nm, in contrast with the empty and water-filled (6,5)-SWCNTs, which emit at ≈ 982 nm and ≈ 987 nm, respectively (Figure 3-4a, c, e). I find that hexane-filled (6,5)-SWCNTs are red-shifted by (12 ± 1) meV from the empty control and by (8 ± 2) meV compared with the water-filled counterpart. In some instances (21 out of 81 individual long nanotubes that were analyzed), I observed partially filled (6,5)-SWCNTs, as shown in Figure 2b, d. The PL peaks shift from 994 nm to 987 nm at different points along the nanotube length, suggesting a single file of n-hexane molecules intermittently spaced along the nanotube. A simplified estimate of the numbers of n-hexane molecules in each pixel region is provided in Supplementary Note 3-1. More examples of empty and partially filled (6,5), (8,3) and (7,5)-SWCNTs are shown in Figure 3-5.
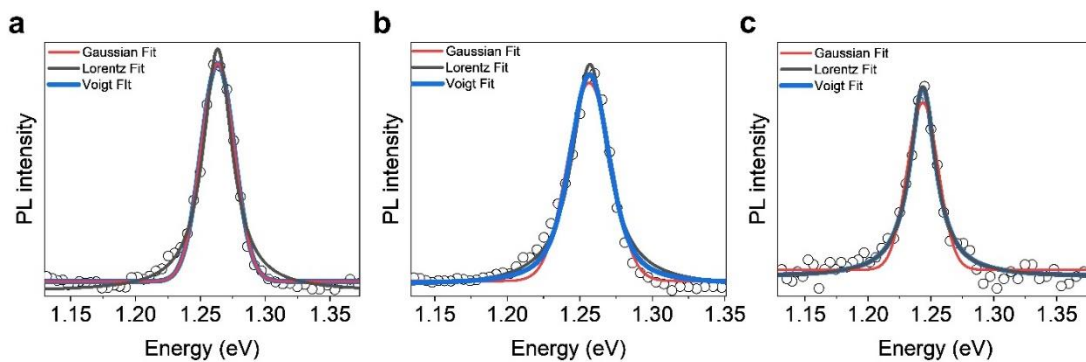
Figure 3-3. Hyperspectral PL imaging spectra of individual (6,5)-SWCNTs fitted with Gaussian, Lorentzian and Voigt functions. a, Empty (6,5)-SWCNTs fitted with Gaussian, Lorentzian and Voigt functions. The peak positions from these fittings are all at 1.263 eV. b, Water-filled (6,5)-SWCNTs fitted with Gaussian, Lorentzian and Voigt functions. The peak positions from these fittings are all at 1.256 eV. c, n-hexane-filled (6,5)-SWCNTs fitted with Gaussian, Lorentzian and Voigt functions. The peak positions from these fittings are all at 1.243 eV. These results show that the peak position is not affect by the fitting functions, although their line widths do.
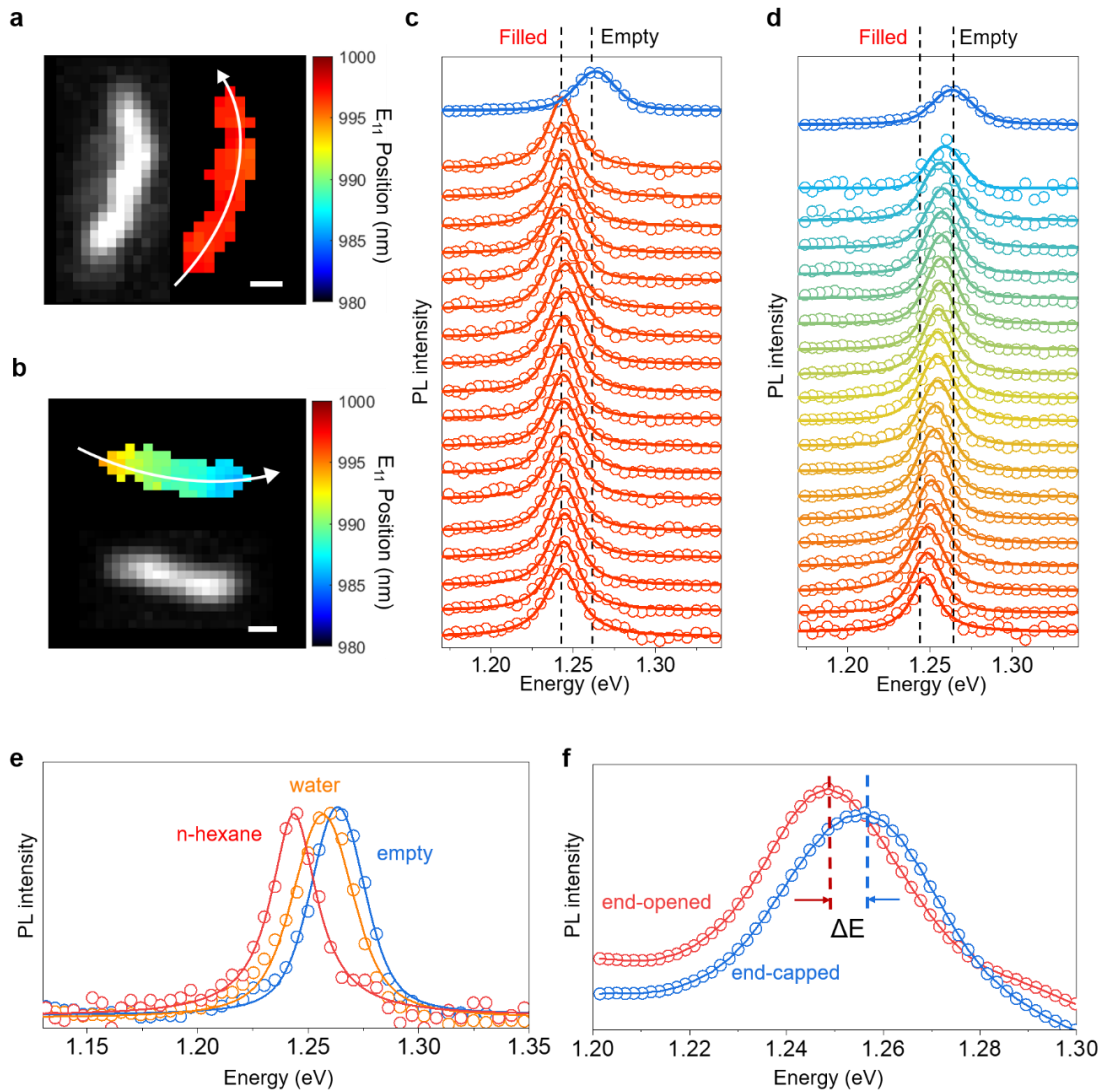
Figure 3-4. Hyperspectral imaging and photoluminescence spectroscopy of alkane-filled individual SWCNTs. a, Hyperspectral images of the E_{11} PL from a single (6,5)-SWCNT that is filled with n-hexane along its length. Left: PL intensity image. Right: Map of the PL peak positions. b, PL image of a (6,5)-SWCNT partially filled with n-hexane. Top: PL Peak position map. Bottom: PL intensity image. c, PL spectra along the center of the n-hexane filled nanotube (indicated by the arrow in a) in comparison with an empty control. d, PL spectra along the center of the nanotube partially filled with n-hexane (indicated by the arrow in b). e, PL spectra from individual (6,5)-SWCNTs that are empty (blue), water-filled (orange), and n-hexane-filled (red). f, Ensemble PL spectra of end-opened (red) and end-capped (6,5)-SWCNTs (blue) that had been incubated in n-hexane. Scale bars in a and b represent 500 nm. Note that in 2a and 2b, the peak position is from spectral fitting of each data set with a Gaussian function. The other spectra are fitted with a Voigt distribution function.
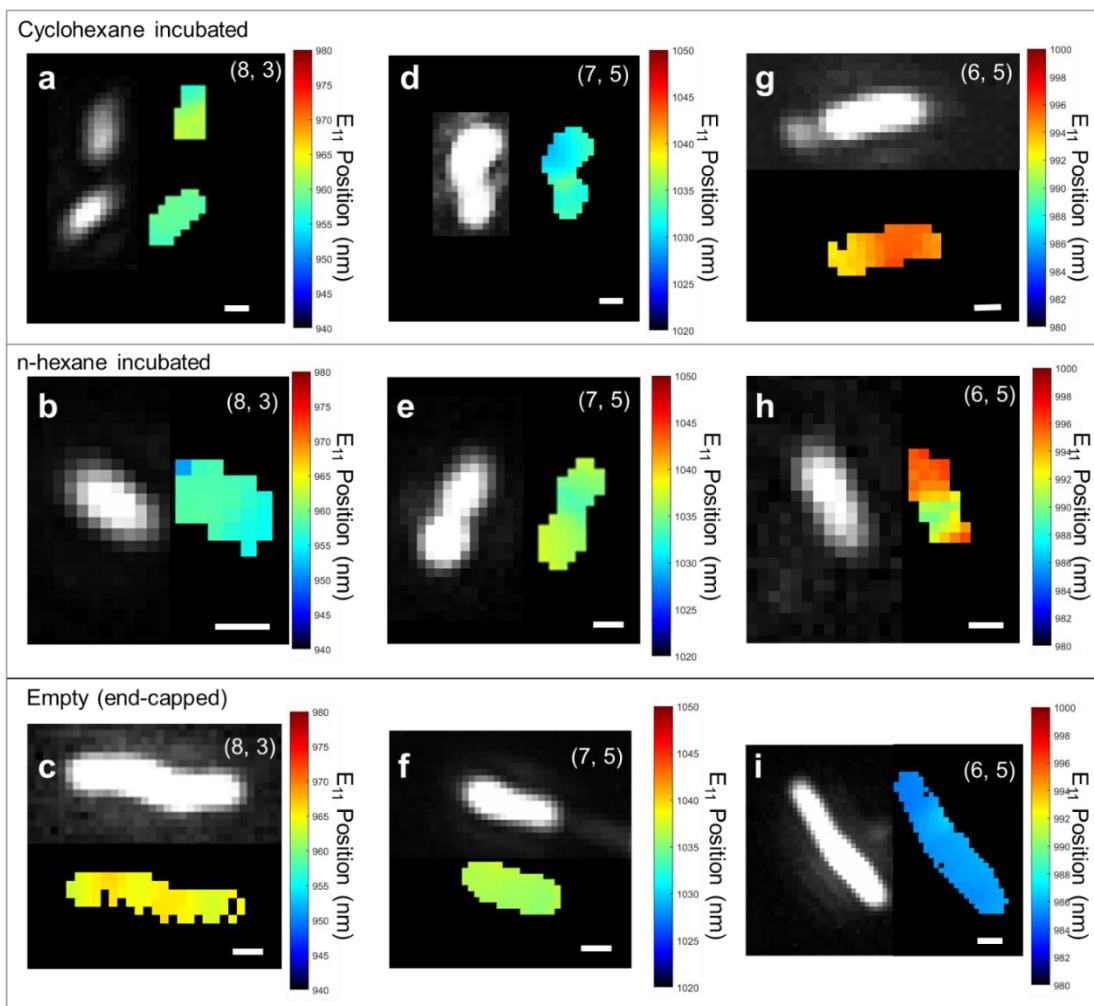
Figure 3-5. Hyperspectral maps of individual SWCNTs that were incubated with cyclohexane, n-hexane, or left empty. a, A cyclohexane-incubated (8,3)-SWCNT. b, An n-hexane-incubated (8,3)-SWCNT. c, An empty (8,3)-SWCNT. d, A cyclohexane-incubated (7,5)-SWCNT. e, An n-hexane-incubated (7,5)-SWCNT. f, An empty (7,5)-SWCNT. g, A cyclohexane-incubated (6,5)-SWCNT. h, An n-hexane-incubated (6,5)-SWCNT. i, An empty (6,5)-SWCNT. For each nanotube, the PL peak position is plotted as a false color image along with the intensity image. Scale bars represent 500 nm. Note that the peak position is from spectral fitting of each data set with a Gaussian function.

3.2.2 Origin of PL Shift

I note there are two possibilities that could produce the observed shifts in the (6,5)-SWCNT spectra: surface adsorption or endohedral filling. If the PL shift were due to the surface adsorption of n-hexane on the nanotubes, then I would expect there

47

to be no observable difference in the PL spectra of end-capped versus end-opened nanotubes. However, I find that the PL of the end-opened nanotubes is clearly redshifted compared to that from the end-capped nanotubes after both samples had been incubated with n-hexane (Figure 3-4f). This result confirmed that the PL shift is caused by endohedral encapsulation of n-hexane molecules. Furthermore, spectroscopy studies confirm the fact that without opening the ends of the nanotubes, the interior channel is inaccessible for filling regardless of how large the pore is relative to the molecule (Figure 3-6 and Figure 3-7), which, again, supports that surface adsorption of hexane or cyclohexane is not the cause of the observed spectral shifts.
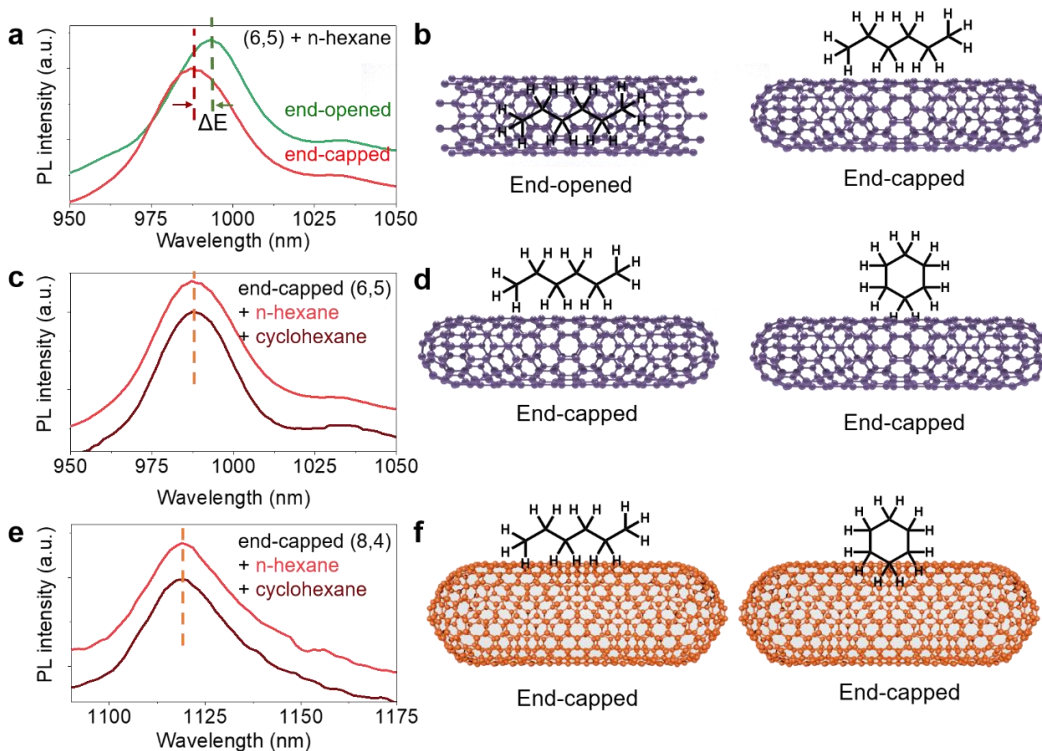
Figure 3-6. Ensemble PL spectra of end-capped and end-opened SWCNTs that were incubated with n-hexane or cyclohexane. a, PL spectra and b, schematic of end-opened (green) and end-capped (6,5)-SWCNTs (red) that were incubated with n-hexane. c, PL spectra and d, schematic of end-capped (6,5)-SWCNTs that were incubated with n-hexane (light red) and cyclohexane (dark red). e, PL spectra and f, schematic of end-capped (8,4)-SWCNTs that were incubated in n-hexane (light red)

48

and cyclohexane (dark red). Note that the spectra are normalized at the peak intensity and offset for clarity.
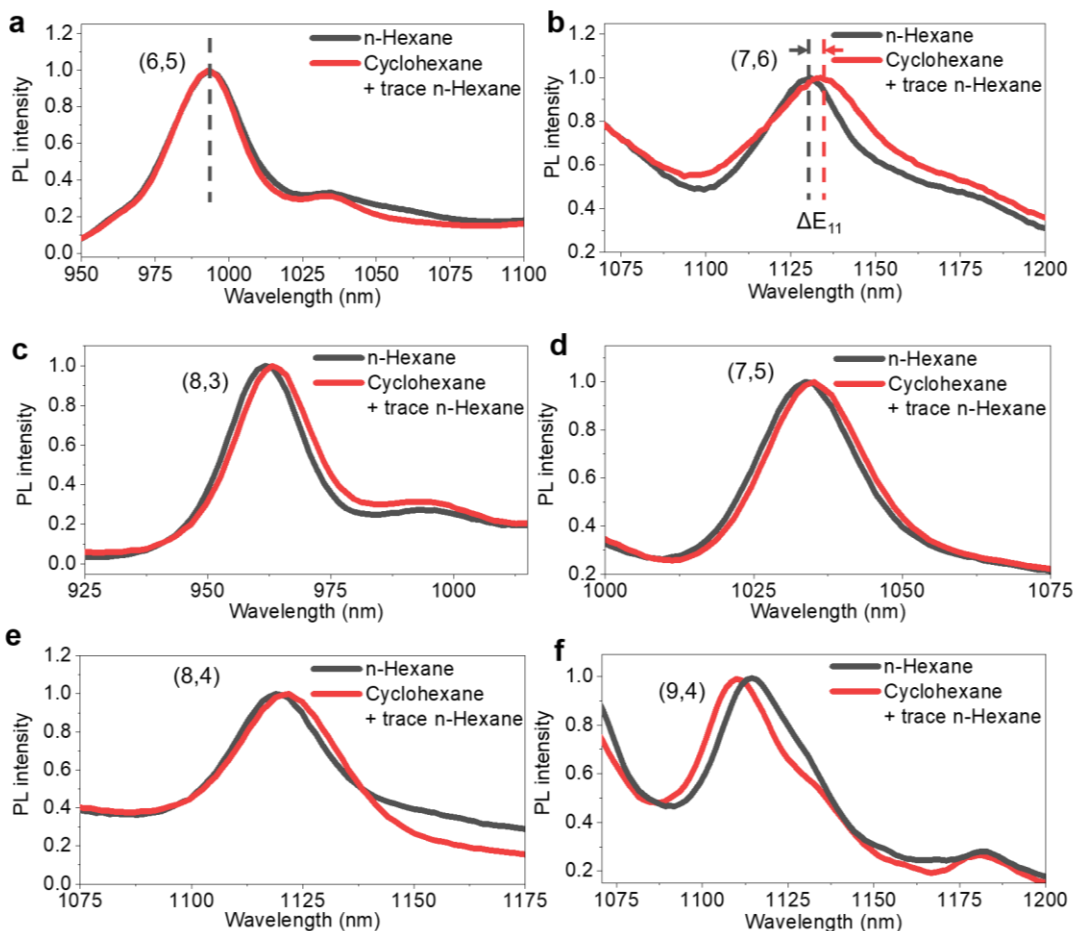
Figure 3-7. End-opened Nanotube photoluminescence responds to filling molecules. a, (6,5); b, (7,6); c, (8,3); d, (7,5); e, (8,4); and f, (9,4) SWCNTs respond to cyclohexane (red curves) and n-hexane (black curves) with a spectral shift. The nanotube ends were opened prior to incubation with the solvents.

Molecular filling can induce strain on the nanotube[130] as well as change its interior dielectric environment[125], both of which may cause the observed PL shifts. However, strain-induced PL shifts are strongly dependent on the nanotube mod (*n-m*, 3). Expansive radial strain is predicted to shift the emission of mod (*n-m*, 3) = 1 SWCNTs to the red (i.e., longer wavelength emission) and mod (*n-m*, 3) = 2 SWCNTs to the blue when compared to an unstrained nanotube[126, 131]. In contrast, the dielectric

environment is expected to induce the same effect on all nanotubes of the same diameter. I can differentiate these effects of strain *vs.* the dielectric environment by comparing n-hexane, cyclohexane, and water-filled nanotubes of different mod and relatively larger pore size. I note that water filling also causes a spectral shift due to the dielectric effect, but it features little to no strain since the molecular size of water is relatively small[33, 49]. I observe that PL from (8,4)- and (7,6)-SWCNTs, both being mod 1, are redshifted when incubated with cyclohexane or n-hexane compared with water-filled controls (Figure 3-8). In contrast, mod 2 nanotubes, including (8,3), (7,5), and (9,4), show blueshifts. These trends closely follow the theoretical model by Yang et al.[132], which predicts a mod-dependent, radial strain-induced electronic effect. The larger the strain, the larger the change in the band gap energy *(ΔE)*, following

$$\Delta E \propto (-1)^{[mod(n-m,3)]+1} \cdot \sigma \cdot \sin(3\theta) \qquad \text{Equation 3-1}$$

in which σ is the radial strain, θ is the SWCNT chiral angle, and mod(n-m,3) is the nanotube mod. In particular, the Fermi point is pushed away from or closer to the Brillouin zone vertices due to expansive strain depending on the mod of specific SWCNT species[126]. The mod-dependent behavior I observe (Figure 3-8) strongly suggests that strain induced from molecular encapsulation, rather than change in the local dielectric environment, is the primary cause of the observed spectral shifts.
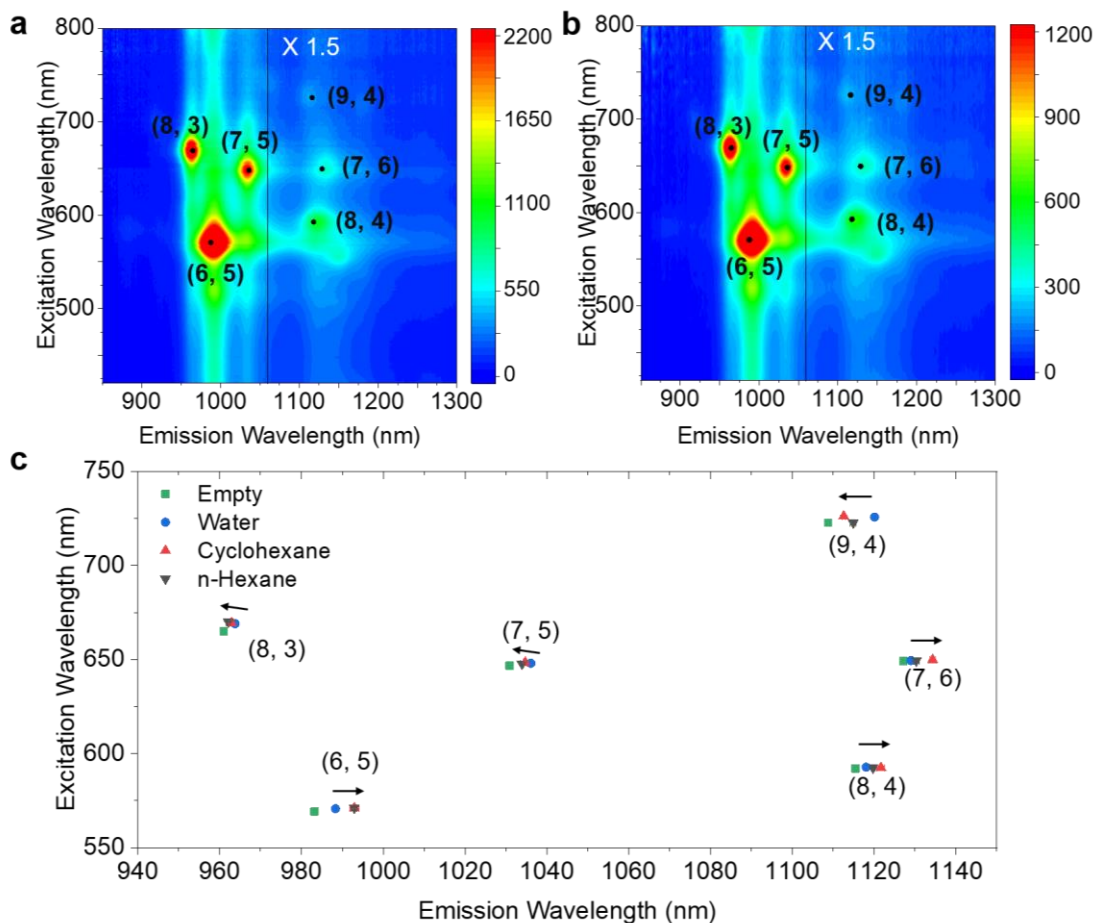
Figure 3-8. Response of nanotube photoluminescence to filling molecules. Excitation-emission PL maps of SWCNTs that are incubated with a, cyclohexane and b, n-hexane. Note that the black dots mark the PL peak position of water-filled SWCNTs. The PL intensity beyond 1060 nm is plotted at 1.5× scale to make the minority nanotube species visible. c, Peak position of the E_{11} PL for SWCNTs incubated with cyclohexane (red) or n-hexane (black), and those filled with water (blue) or empty (green). The arrows indicate the direction of the spectral shift between water and alkane-filled species.

I also conducted Raman spectroscopy to further confirm that the observed PL shift is indeed induced by strain (see Supplementary Note 3-3). I observed a ≈ 3 cm⁻¹ downshift of the G-band (Figure 3-2b) and ≈ 4 cm⁻¹ upshift of the radial breathing modes (RBMs) of the n-hexane-filled (6,5)-SWCNTs (Figure 3-2c) compared with the

water-filled control. These shifts are indicative of n-hexane generating strain on the nanotube sidewalls, consistent with previous observations[130, 133].

I defined the spectral shift between n-hexane- and cyclohexane-incubated SWCNTs as $\Delta E_{11} = E_{11, \text{cyclohexane}} - E_{11, \text{n-hexane}}$, and plot ΔE_{11} as a function of the pore diameter for each filling molecule (Figure 3-9, van der Waals pore sizes are provided in Table 3-1). I find that for mod 1 nanotubes ((6,5), (8,4), and (7,6)) ΔE_{11} becomes more negative with increasing pore diameter, as shown by the orange curve in Figure 3, while for mod 2 chiralities ((8,3), (7,5), and (9,4)) ΔE_{11} becomes more positive. These trends unambiguously support a strain-induced electronic effect[132] due to the molecular filling. Interestingly, I observed a ΔE_{11} of ≈ 0 meV for (6,5)-SWCNT, while for larger diameter nanotubes $\Delta E_{11} \neq 0$ meV. This occurs because when incubating (6,5)-SWCNT with cyclohexane it was not cyclohexane, but trace contaminant n-hexane that filled the nanotube. Even though the labeled purity for the commercially available high purity cyclohexane is 99.9 %, n-hexane exists as a trace impurity that is difficult to remove completely, as I confirmed by composition analysis using gas chromatography coupled with a mass spectrometer (GC-MS) (Figure 3-10). In contrast, both n-hexane and cyclohexane can fit in larger diameter SWCNT hosts, such as (8,3), (7,5), and (8,4), and cause the mod-dependent PL shifts (Figure 3-9).
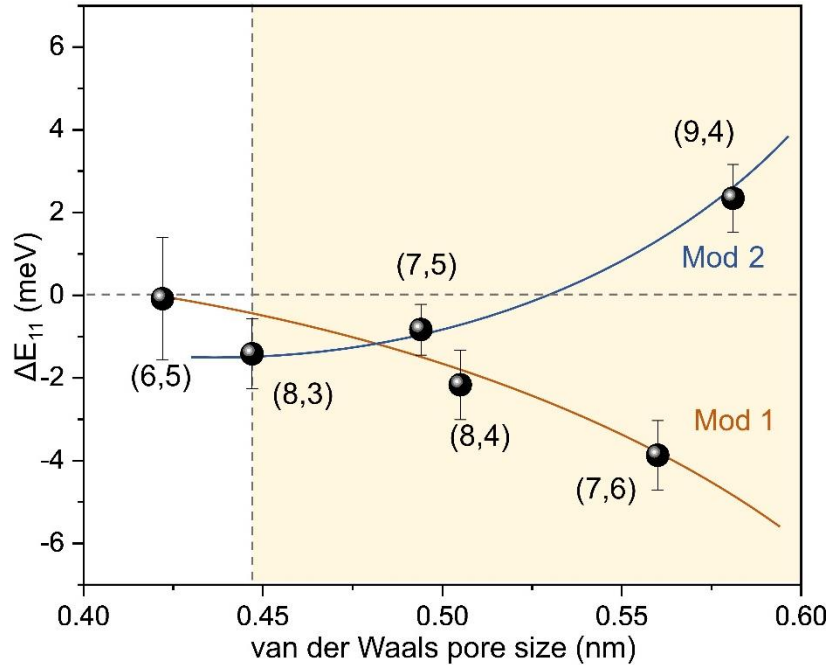
Figure 3-9. Molecular filling of nanotube pores is size dependent. The PL energy differences between cyclohexane (99.9%)- and n-hexane-incubated end-opened SWCNTs ($\Delta E_{11} = E_{11, \text{cyclohexane}} - E_{11, \text{n-hexane}}$) obtained from experiments are plotted as a function of the van der Waals pore size of the nanotubes. Both n-hexane and cyclohexane can fit in those nanotube pores in the yellow colored area, while only n-hexane can enter the (6,5)-SWCNT pore, suggesting the existence of a threshold pore size below which n-hexane can enter but cyclohexane cannot. Note that the curves are added to guide the eye. The curves connect nanotubes of Mod 1, with mod(n-m,3)=1, and Mod 2 (mod(n-m, 3)=2). The error bars represent the standard deviation of the E_{11} emission peak position measured from multiple different SWCNT samples. Uncertainty in the calculated points are represented by error bars equal to one standard deviation.

Table 3-1. van der Waals pore sizes of the nanotubes used

SWCNT chirality	carbon center-to-center diameter (nm)[134]	van der Waals pore size (nm)*
(6,5)	0.757	0.422
(8,3)	0.782	0.447
(7,5)	0.829	0.494
(8,4)	0.840	0.505
(7,6)	0.895	0.560
(9,4)	0.916	0.581

* calculated by subtracting the van der Waals diameter of carbon atom from the carbon center-to-center diameter of SWCNTs. Note that the van der Waals diameter of carbon atom used here is the interlayer spacing in graphite (0.335 nm). The diameter of (n,m)-SWCNT is calculated from $d_t = \frac{\sqrt{3} l_{C\text{-}C}}{\pi} \sqrt{n^2 + m^2 + mn}$ based on wrapping a graphene sheet with a C-C bond distance $l_{C\text{-}C}$ of 1.44 Å.
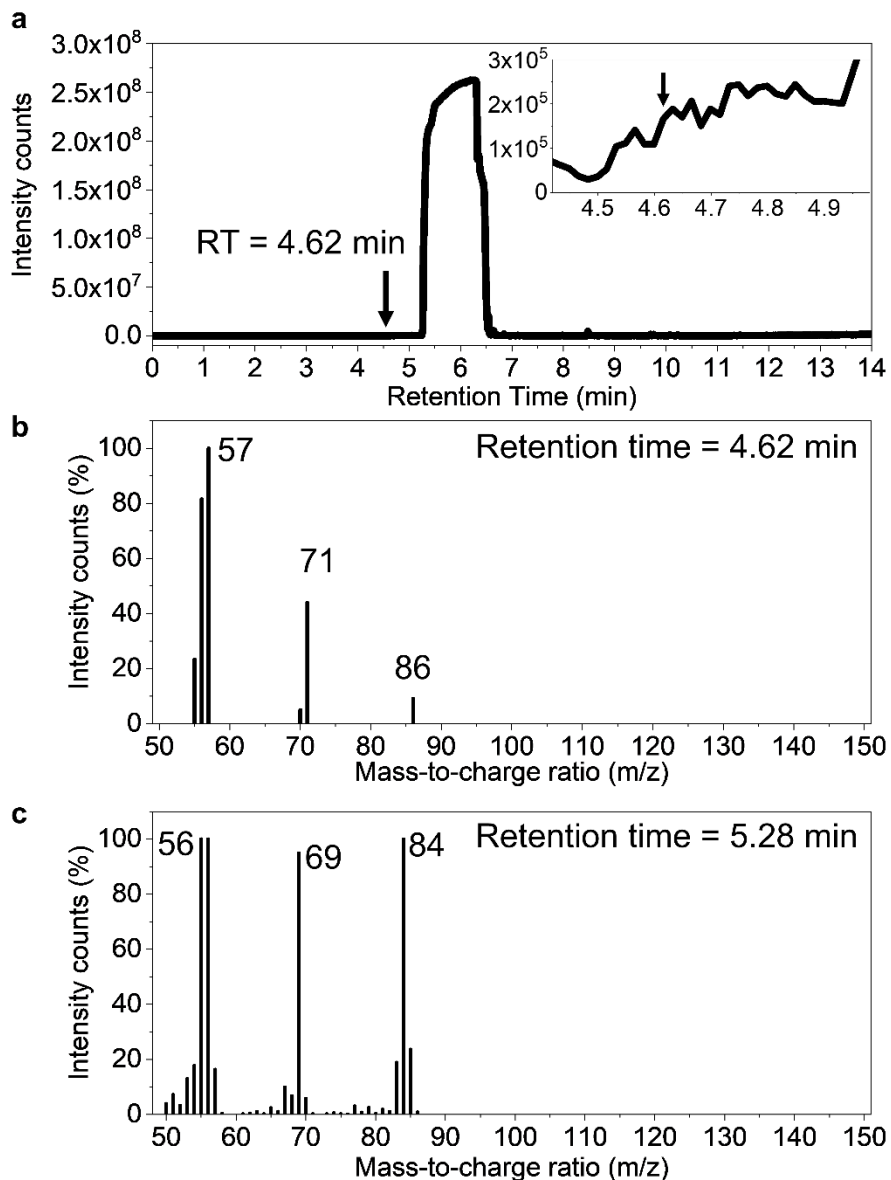
Figure 3-10. GC-MS analysis of a commercial cyclohexane solvent (purity ≥ 99.90 %). a, Gas chromatogram of the cyclohexane. b, Mass spectrum of the component eluted at 4.62 min, which is assigned to n-hexane. Although there is no obvious peak in the gas chromatogram, the trace amount of n-hexane can be detected by the coupled JEOL high resolution magnetic sector mass spectrometer with an EI ion source (the detection sensitivity is on the order as low as 1 femtogram). c, Mass spectrum of the component eluted at 5.28 min, which is assigned to the majority cyclohexane component.

3.2.3 *Molecular Sieving of n-Hexane from Cyclohexane*

As cyclohexane and n-hexane are nearly identical in chemical identity, the pair serves as an excellent model system to challenge the ability of nanotube pores for possible molecular sieving. I prepared a mixture of 0.1 % (by volume) n-hexane in 99.9 % cyclohexane solution, in which I incubated end-opened SWCNTs composed of primarily (6,5)-SWCNTs at room temperature (Figure 3-11). After incubation with different amounts of SWCNTs, the nanotubes were removed from the solvent mixture by filtration and the purity of cyclohexane was quantified by GC-MS. Figure 3-11b shows the cyclohexane purity (%, vol/vol) and n-hexane concentration (μmol/mL) as a function of the SWCNT mass added per unit volume. Note that the removal of n-hexane occurs only with open-ended SWCNTs (Figure 3-12a). These experiments demonstrate that the n-hexane was selectively removed by the addition of the end-opened SWCNTs. I estimated the percentage of the pore volume occupied by n-hexane inside the (6,5) nanotubes was in the range of (52-82) % for the SWCNT concentrations measured, as shown in Figure 3-11. The detailed calculation is described in Supplementary Note 3-2.

Our series of experiments provide unambiguous evidence that (6,5)-SWCNTs can be selectively filled with n-hexane. However, the widely used concept of KD failed to capture this phenomenon. This observation thus challenges our current understanding of the nanotube pore and may have broad implications for nanopore applications where molecular filling is the critical first step to selectivity and transport.
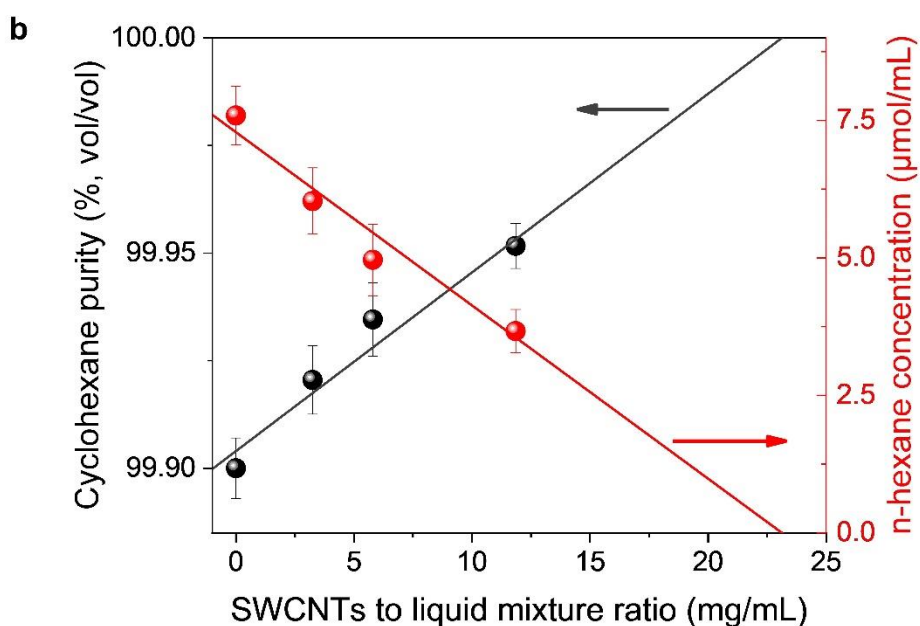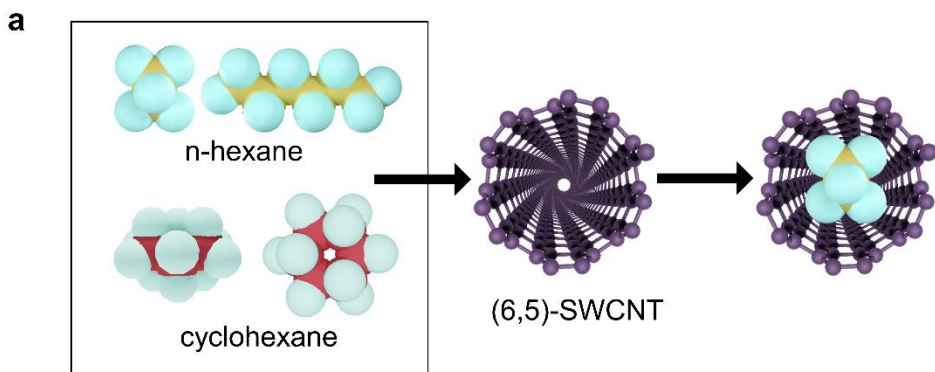
Figure 3-11. Molecular sieving of n-hexane from cyclohexane. a, Schematic of the molecular sieving of n-hexane and cyclohexane by (6,5)-SWCNTs. Only n-hexane molecules can enter the nanopore of (6,5)-SWCNTs. Note that for clarity the carbon atoms are displayed in two different colors: golden (n-hexane) and red (cyclohexane). b, Molecular sieving of n-hexane from 99.9 % (volume/volume) cyclohexane by (6,5)-SWCNTs. Plotted are cyclohexane purity and n-hexane concentration as a function of the nanotube mass per unit volume added to purify the mixture. The cyclohexane purity was determined by quantitative GC-MS. The two trendlines are added to guide the eye assuming linear extrapolation. Uncertainty in the calculated points are represented by error bars equal to one standard deviation.
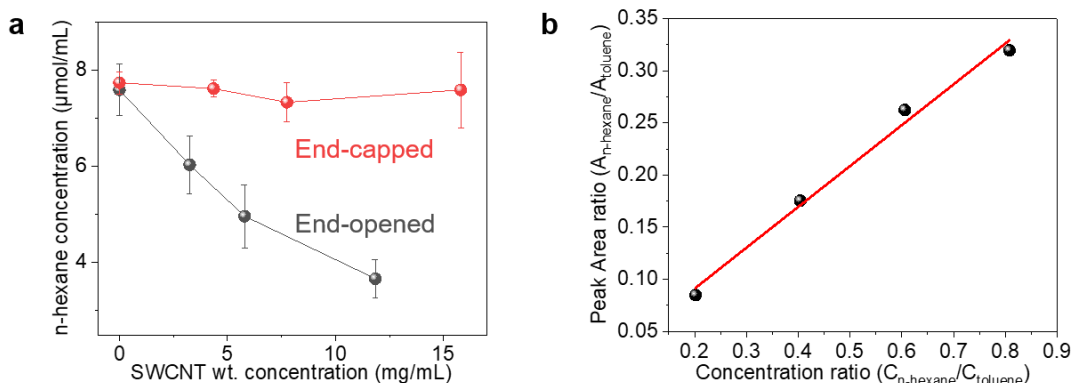
Figure 3-12. GC-MS experiment for n-hexane concentration measurement. a, Selective adsorption of n-hexane comparison between end-closed and uncapped nanotubes. b, GC-MS calibration curve of concentration. The peak area ratio of hexane and toluene ($A_{\text{n-hexane}}/A_{\text{toluene}}$) is plotted as a function of the concentration ratio ($C_{\text{n-hexane}}/C_{\text{toluene}}$). The slope of the fitting curve is the response factor, which is $\approx$ 0.3918. $R^2 = 0.99$. Uncertainty in the calculated points are represented by error bars equal to one standard deviation.

3.2.4 Molecular Dynamics and ab-initio Molecular Dynamics Simulations

To understand how hexane enters the tight pore, I performed molecular dynamics (MD) and *ab initio* MD simulations. I terminated the nanotube ends with hydroxyl (-OH) groups, as expected from oxidative end-uncapping, and held the tube in place with graphene walls. I then kept the SWCNT in an n-hexane/cyclohexane bath at 300 K, as shown in Figure 3-13, and modeled the system as an isothermal-isobaric ensemble, in which the number of molecules, pressure, and temperature were held constant. Because the curvature effects[135] become so pronounced in these small diameter nanotubes, the concept of van der Waals radii of atoms[136, 137], which model atoms as hard spheres, and the kinetic diameter of molecules[121], which are calculated based on the van der Waals radii, cannot fully capture the nanopore-molecule interactions. I incorporate these effects by performing *ab initio* MD where the electronic structure calculations are combined with all atom MD (see Methods for

57

details) and calculate the projected radial distance (Δ) between n-hexane atoms and the SWCNT carbons in the molecule filled nanotube (Figure 3-14). By subtracting Δ from the nanotube diameter I can define an accessible pore size (Φ) that can be directly compared with the minimum projected diameter of the filling molecule (Figure 3-15). For the n-hexane filled (6,5)-SWCNT, I obtain a Δ of 0.244 nm and an accessible pore size of 0.269 nm for (6,5)-SWCNT. Interestingly, n-hexane enters (6,5)-SWCNT only when it is in the stretched state, whereas the un-stretched n-hexane is excluded from the pore of (6,5)-SWCNT (Figure 3-16). Compared to the relaxed state (i.e., the most probable configuration) in the bulk solution, the n-hexane molecule is stretched by 11.2 % (elongated along the length) inside the (6,5)-SWCNT pore (Table 3-2). MD simulations on (6,5)-SWCNT, (8,3)-SWCNT as well as other SWCNTs (Supplementary Note 3-5) corroborate experimental observations (shown in Figure 3-9) that there exists a threshold pore diameter below which only n-hexane enters the pore whereas cyclohexane cannot.
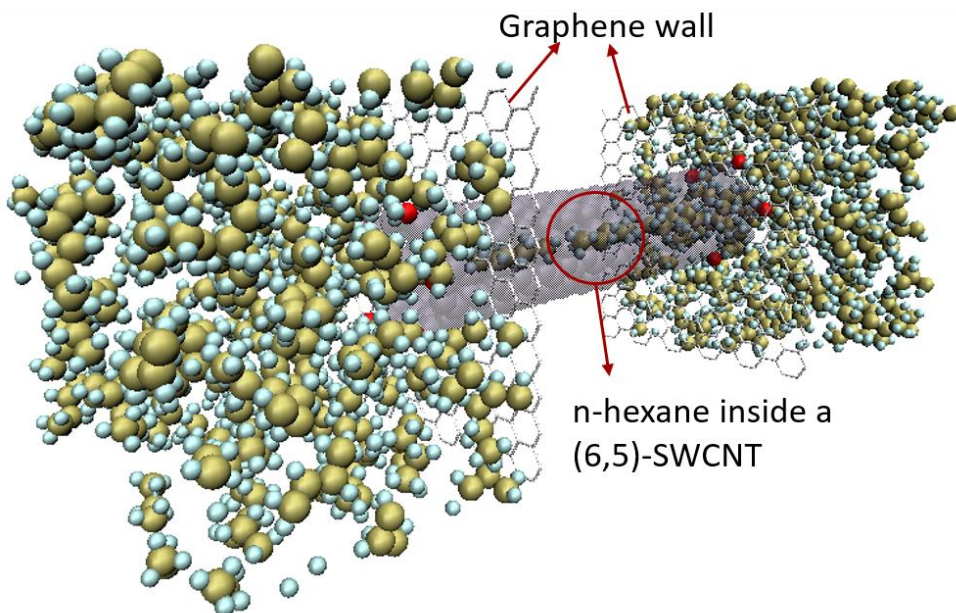
Figure 3-13. The system used in the MD simulations, with SWCNTs emptying into cyclohexane (or n-hexane) baths kept at 300 K and 1 atm pressure. The ends of the SWCNT are terminated with hydroxyl (-OH) groups. Note that completely relaxed angle parameters are used for n-hexane in this simulation. The dimension of the cyclohexane (or n-hexane) bath is $2.5 \times 2.5 \times 2.5$ nm^3, and the length of the SWCNT is 4 nm.
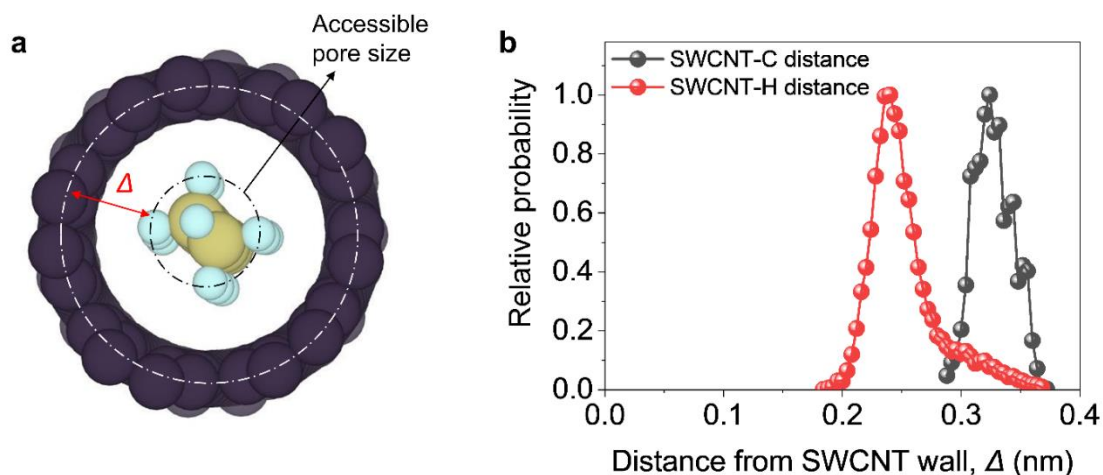
Figure 3-14. Accessible pore size from AIMD simulations. a, Schematic of the accessible pore size, which is defined as the nanotube diameter subtracting the minimal atom-center-to-center distance between the (6,5)-SWCNT wall and n-hexane hydrogens. b, Probability distribution of the projected radial distance ($\varDelta$) between the carbon and hydrogen atoms of the n-hexane molecule and the (6,5)- SWCNT wall.
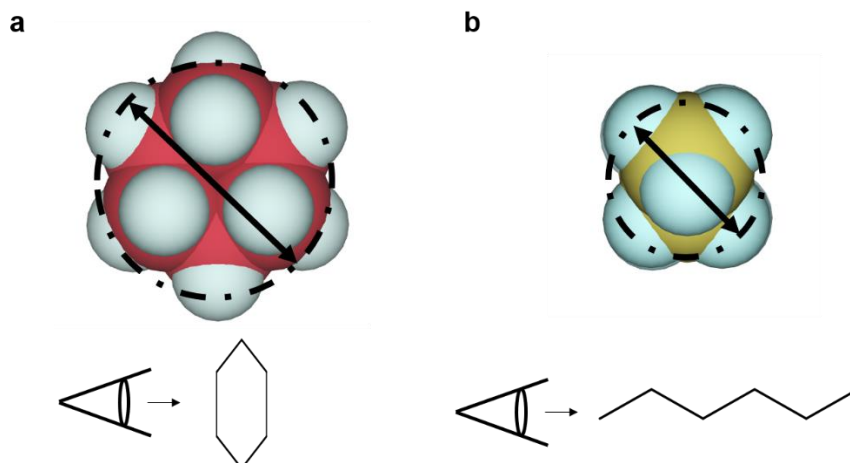
Figure 3-15. Schematic showing the minimal projected diameter of a molecule. a, cyclohexane. b, n-hexane. Note, the projected diameter calculated in our simulations are atom center-to-center distance. Geometries for n-hexane and cyclohexane are optimized using Density Functional Theory (DFT).

n-hexane at
initial timestep

Un-stretched
n-hexane at
final timestep

Stretched
n-hexane at
final timestep
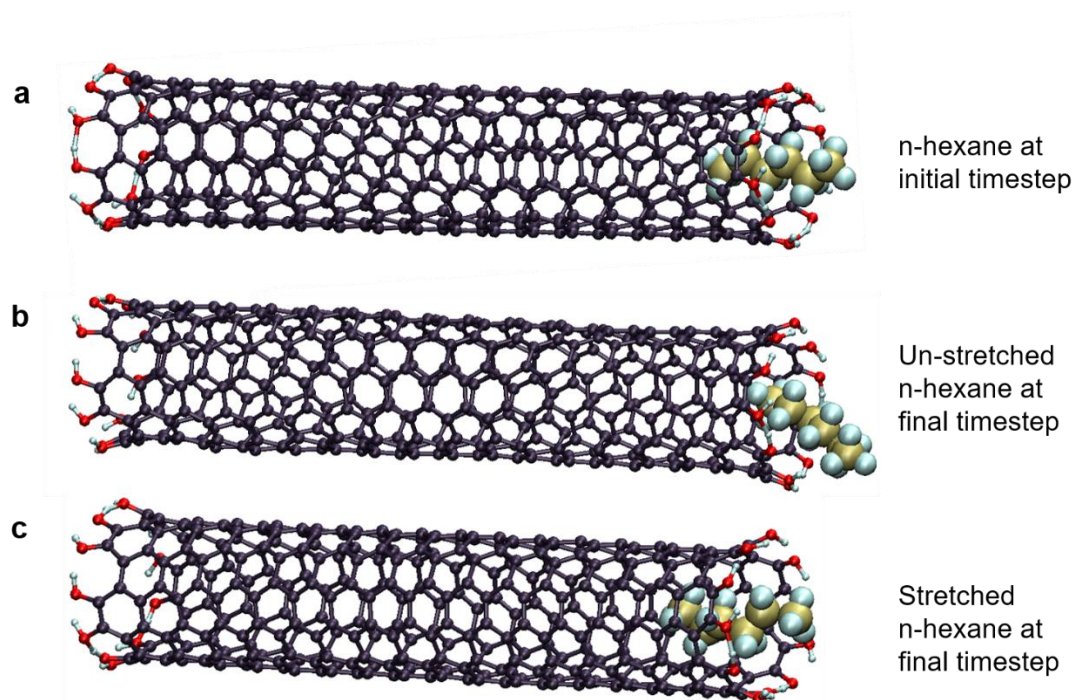
Figure 3-16. AIMD simulations of filling a (6, 5)-SWCNT with stretched and un-stretched n-hexane. a, The n-hexane molecule is placed in the pore mouth at t = 0. b, The final configuration of un-stretched n-hexane at the end of the simulation at t = 2 ps. c, The final configuration of the stretched n-hexane at the end of the simulation at t = 2 ps. The AIMD simulations were performed at 300 K.

60

Table 3-2. The molecular configurations of n-hexane under the confinement of (6,5)-SWCNT (stretched) and in the bulk solution (un-stretched) at 300 K and 1 atm. These values are calculated by averaging the respective bond lengths and angles for one sample configuration of stretched and un-stretched n-hexane (provided in the supplementary file). The sample configuration for stretched n-hexane is obtained when n-hexane is under confinement of (6,5)-SWCNT and for un-stretched n-hexane is obtained from the most probable configuration of n-hexane in the bulk solution at 300 K, 1 atm. These values are obtained from MD with systems described in the Methods section.

	C-C bond length (Å)	C-H bond length (Å)	C-C-C bond angle	C-C-H bond angle	H-C-H bond angle	length of n-hexane (Å)*	minimum projected diameter (Å)
un-stretched	1.52	1.09	114.287˚	106.657˚	109.833˚	8.084	2.80
stretched	1.52	1.09	144.723˚	101.165˚	115.244˚	9.045	2.510

*Lengths of n-hexane molecules are end-to-end hydrogen distances.

To further understand the stretched molecule size, I calculate the minimum projected diameter of n-hexane in each of its different molecular configurations, or stereoisomers, and observe that the most probable configuration occurs at a minimum projected diameter of 0.28 nm (Figure 3-17). Importantly, I find that the stretched configuration of n-hexane (with a minimum projected diameter of 0.251 nm) exists in the bulk solution at 300 K and overall there is a 28.5 % probability (blue-shaded area in Figure 3-17) for a free n-hexane molecule to exist in molecular configurations that are smaller than the (6,5)-SWCNT's accessible pore diameter (0.269 nm). In contrast, for cyclohexane, the minimum projected diameter for the most probable configuration is 0.398 nm and there is zero probability for the molecule to exist at a configuration that is smaller than the (6,5)-SWCNT's accessible pore size, which explains its complete exclusion from the nanopore.
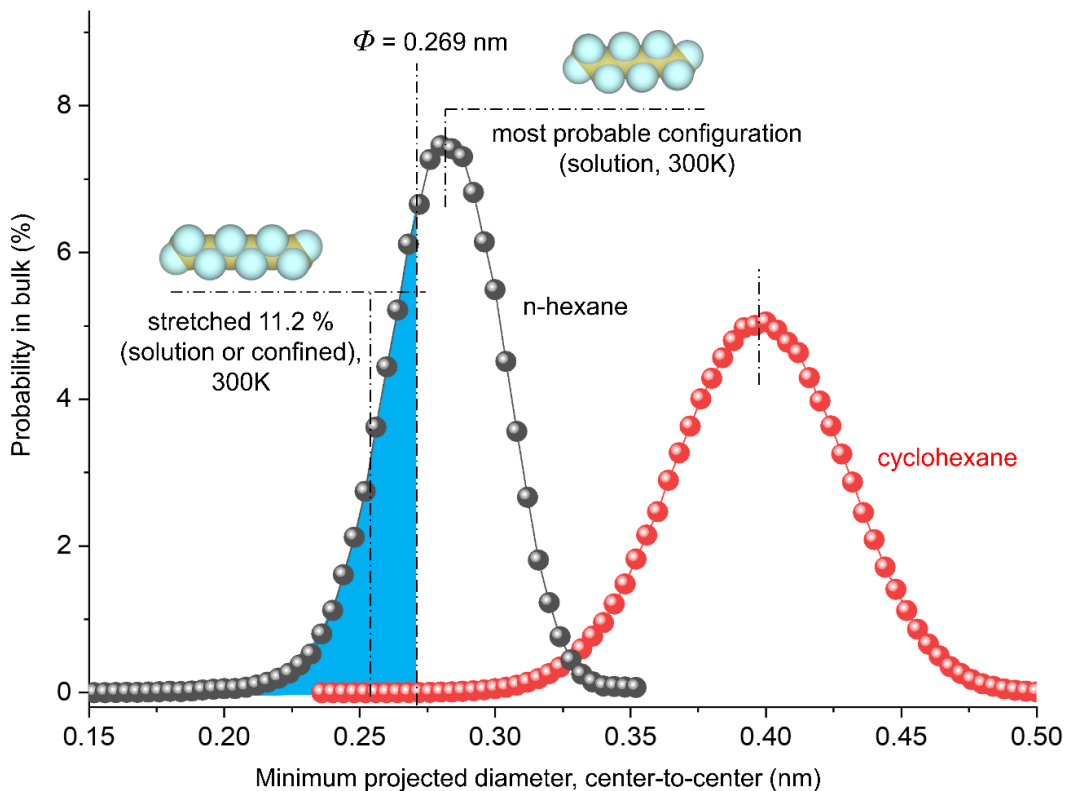
Figure 3-17. Molecular dynamics simulations revealing that n-hexane adapts a stretched molecular configuration to enter a tight pore. Plotted are the distributions of the minimum projected diameter for each stereoisomer of n-hexane (black dots and line) and cyclohexane (red dots and line) in bulk solution at 300 K, which are sampled from a total of 222039 and 1131188 molecular configurations for n-hexane and cyclohexane, respectively. The molecular models are also shown for the most probable configuration of n-hexane in solution and in its stretched state (in bulk solution or under confinement of the (6,5)-SWCNT pore). The n-hexane molecule extensionally stretched 11.2 % with a minimum projected diameter 0.251 nm which is smaller than the accessible pore size of the (6,5)-SWCNT (Φ = 0.269 nm). The overall probability that any particular free n-hexane molecule exists in a conformation sufficiently narrow to enter the (6,5)-SWCNT interior, calculated through the ratio of the integral of the shaded blue area in the figure to the entire minimum projection curve, is 28.5 %, as highlighted by the blue shaded area. In contrast, there is zero probability for cyclohexane to exist at a molecular configuration smaller than the pore size of (6,5)-SWCNTs.

3.3 Discussion

KD is a concept that has been widely used to represent the molecular size in the field of molecular sieving[138-140]. Our work, however, provides an example that this static view of molecular size fails to capture the flexible nature of molecules in entering a tight space. The structural rigidity of SWCNTs allows us to study the foundation of such observation by isolating the flexibility of the absorbate (n-hexane or cyclohexane in our case) from the pore deformation which could occur with flexible pores such as metal organic frameworks due to the structural motions of ligands and lower Young's modulus[141]. Instead of using the KD, I simulate the dynamic changes of the molecules in solution to obtain the minimal projected diameter, which resolves the discrepancy and better captures the molecular origin of such a molecular sieving phenomenon.

3.4 Conclusions

In summary, I experimentally observed molecular sieving between two competing molecules that are both larger than the pore size of a precision nanopore defined by a carbon nanotube. MD simulations show that n-hexane enters the tight nanopore at its stretched state (elongating by nearly 11.2 %), which exists with an overall probability of 28.5% in the bulk solution at 300 K. The encapsulated molecules cause a strain-induced PL shift that I used as a sensitive optical signature to directly resolve the molecular filling along the length of individual nanotubes by hyperspectral imaging. These unexpected observations provide insights on nanopore selectivity[110] and suggest a strategy for molecular separation[108, 109] by exploiting the molecular degrees of freedom.

3.5   Supplementary Notes

3.5.1   Supplementary Note 3-1: Estimation of the numbers of filled n-hexane molecules in (6,5)-SWCNTs based on hyperspectral imaging

To estimate the number of filled n-hexane molecules, I have to consider the diffraction limit. The pixel size (≈ 160 nm) is smaller than the diffraction limit, which stands at ≈ 580 nm in our case (calculated form $\frac{\lambda}{2\text{NA}}$, where λ is the wavelength of the 980 nm emission from (6,5)-SWCNT, and NA $= 0.85$ is the numerical aperture of the objective used). For this work I used long nanotubes (> 3 μm) to achieve sufficient spatial resolution of PL imaging. It is not possible to completely deconvolute the complexity formed by so many emitting nanotube segments when they are partially filled. However, I may estimate the number of n-hexane molecules in each pixel based on the assumption that strain and PL shift correlation is linear.

In the case of n-hexane filling, the major cause of the photoluminescence (PL) shift is the strain, which is described by Yang's model[126] and other literature reports[142]. The PL shift (ΔE) is observed to be linearly proportional to the strain[131]. Due to the single-file packing, I can consider the system as one dimensional such that the strain is linearly correlated with the number of filled molecules. If this assumption holds, the strain and resulting PL shift is then directly proportional to the number of n-hexane molecules within the nanotube pore.

By considering a linear scaling of the PL peak shift for the empty (0 %) up to the fully filled (100 %) nanotubes, I can obtain the percentage (P) of the nanotube filled with n-hexane from the E_{11} peak wavelength by the following relation:

$$P = kE_{11} - b \qquad \text{Equation 3-2}$$

where E_{11} is the PL emission peak wavelength in nm, k and b are two constants due to the linear relationship of strain and resulting PL. I then substitute ($E_{11} = 982$, $P = 0\%$) and ($E_{11} = 998$, $P = 100\%$) into the equation to obtain k (= 0.0625) and b (= 61.375) for this case. When one n-hexane fills inside a nanotube segment, the length of this segment is roughly equal to the length of the stretched n-hexane (1.14 nm, based on the atom center-to-center length of n-hexane, 0.90 nm, plus the van der Waal radii of the two hydrogen atoms, 2 x 0.12 nm = 0.24 nm). Based on these, the numbers of n-hexane can be derived. For example, for pixels that have an E_{11} peak of 990 nm in Figure 2b, I can calculate the percent filling of the nanotube is 50% n-hexane by plugging in $E_{11} = 990$ nm. I can further derive that on average there are ≈ 0.43 hexane molecules per nanometer length of (6,5)-SWCNT.

I note that the peak positions (Figure 3-4a,b) used in the above calculations are from fitting the spectra with a Gaussian profile. The spectra are best fit with a Voigt distribution function which is a result of the convolution of a Gaussian profile (inhomogeneous broadening) and a Lorentzian profile (homogeneous broadening).[33] Although the linewidths are different, all these functions give the same peak positions in our case, as shown in Figure 3-3. Because the Voigt function is computationally more expensive to implement to fit the cubes from hyperspectral imaging, I have used a Gaussian function for the spectral fitting when only the peak position is needed, including Figure 3-4a, 2b and Figure 3-5. In all the other cases, a Voigt function is used.

3.5.2 Supplementary Note 3-2: Estimation of the percentage of the pore volume of the tubes filled with n-hexane.

In Figure 3-11, I show that the n-hexane can be removed from the mixture by (6,5)-SWCNTs. To estimate the filled pore volume, I assume all the SWCNTs are (6,5)-SWCNTs, though I note the nanotube raw material is synthesized as a mixture of different chiralities, with (6,5)-SWCNTs being the major component. I also considered the SWCNT purity ($\approx$ 77.1 mass % based on the manufacturer's product specs).

Adsorption of n-hexane should result in the n-hexane molecules packing single-file inside the (6,5)-SWCNTs due to the size limitation. Therefore, I can estimate the percentage of the pore volume filled with n-hexane based on the length of the molecule and that of the SWCNTs. Since only stretched n-hexane can enter (6,5)-SWCNTs, the molecular configuration that fits the nanotube has a length of 1.14 nm. Therefore, I can estimate when 100 % filled, these nanotubes can densely encapsulate at least 2.07 µmol/mL, 3.68 µmol/mL, 7.52 µmol/mL of n-hexane inside 2.51 mg/mL, 4.47 mg/mL, 9.13 mg/mL (6,5)-SWCNTs, respectively. The actual amount of n-hexane removed was experimentally determined to be 1.56 µmol/mL, 2.63 µmol/mL, 3.92 µmol/mL, respectively (Figure 3-11). From the ratios, I obtained the percentage of the filled space to range from 52% to 82 % for the experiments performed here. These data suggest that the molecules are loosely packed inside the nanotube pore.

3.5.3 Supplementary Note 3-3: Raman spectroscopy

I conducted Raman spectroscopy to further investigate the effect of SWCNT strain. The D peak of SWCNTs, which originate from the structural disorder, are

commonly located at $\approx$ 1355 cm^{-1}, while G peaks are at $\approx$ 1585 cm^{-1} and represent the ordered graphitic structure. Supplementary Figure1a shows the G and D peaks of the Raman spectra from the end-opened and end-capped nanotubes. After the end opening process, the D/G ratio slightly increases from 0.021 to 0.032. This low increase of disorder suggests the amount of nanotube oxidation during the opening process was small. Furthermore, such oxidative defects are known to quench the SWCNT photoluminescence (PL).[143] However, I observed bright PL from the nanotubes (Figure 3-4 and Figure 3-5), indicating the effect of changing PL properties in terms of peak wavelength and intensity caused by these defects was negligible.

Figure 3-2b shows the G peaks of n-hexane- and water-filled (6,5)-enriched SWCNTs. Note: Due to the ensemble averaging, the G-band and D band signal may be convoluted with contributions from other minor species, such as (8,3) and (7,5). The downshift (3 cm^{-1}) of the G peak of the n-hexane-filled SWCNTs compared to the water-filled nanotubes indicates endohedral encapsulation of n-hexane creates radial expansive strain on the nanotube sidewalls, which is consistent with ref.[130]. The radial breathing mode (RBM) peak of the n-hexane-filled (6,5)-SWCNTs is $\approx$313 cm^{-1}, which is upshifted 4 cm^{-1} compared with the water-filled control (Figure 3-2c).

3.5.4   Supplementary Note 3-4: Grid size used in simulation

To have more confidence on the inferences I might have made from the 1x1x4 grid, I performed additional simulations to compare the energies obtained from using a finer grid. I find that the energies obtained from the 4x4x1, 2x2x2 and 4x4x4 grid differ from the values obtained from the 1x1x4 by around 0.005 eV (Table 3-3). These finer grids have higher number of k-points, making them computationally impractical and

too expensive to perform AIMD simulations since the number of atoms (N) in the system exceeds 400 and the computational cost scales as ~O(N3). However, the energies obtained from the 1x1x4 grid are close to those from the finer grids. I also note that the value used for the cut-off energy (400 eV) is right on the border of where the plot in Figure 3-18b starts converging. Using 400 eV, the error in the energy from its converged value of -3963.3562 eV is 0.07%, which makes it a reasonable balance between precision and computing cost.

Table 3-3. Grid size and corresponding total electronic energy (eV) in AIMD

Grid size	Total electronic energy (eV)
1x1x4	-3963.3504 eV
2x2x2	-3963.3556 eV
4x4x1	-3963.3554 eV
4x4x4	-3963.3562 eV
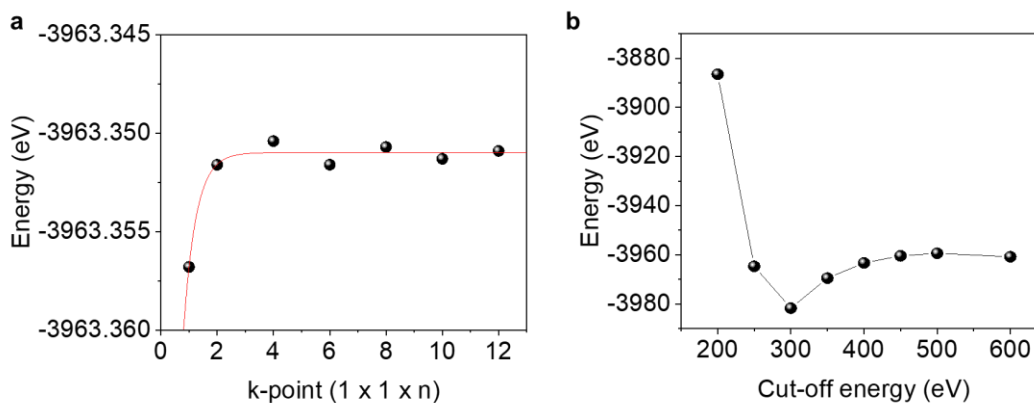
Figure 3-18. Convergence from AIMD. a, Convergence as a function of grid size. b, Convergence as a function of cut-off energy

3.5.5 Supplementary Note 3-5: Conformational changes of n-hexane in MD simulation

OPLS-AA potential[144] is used to model n-hexane and cyclohexane, which determines the bond lengths, angles and dihedrals of these molecules. This potential

68

allows for small deformations about the mean for bond lengths, angles and dihedrals. However, completely relaxing angle parameters (while keeping the bond and dihedral parameters the same as the OPLS-AA model), achieved by setting the force constants (k_θ) of all angles in n-hexane and cyclohexane to zero, allows for large conformational changes in these molecules, thereby allowing them to freely stretch and compress. Only after relaxing the angle parameters, I observed that n-hexane molecules could enter (6,5)-SWCNT, with cyclohexane still being excluded and this result is consistent with AIMD calculations. To estimate the threshold at which the hexane enters whereas cyclohexane cannot, a range of SWCNTs in increasing order of diameter, i.e., (6,5)-, (8,3)-, (7,5)-, (8,4)-, (7,6)- and (9,4)-SWCNT ((van der Waals pore size ranging from 0.422 nm to 0.581 nm) were investigated. I then kept the SWCNT in an n-hexane/cyclohexane bath at 300 K, as shown in Figure 3-13, and modeled the system as an isothermal-isobaric ensemble, in which the number of molecules, pressure, and temperature were held constant. The MD results corroborate our experimental observations that (8,3)-SWCNT and large diameter nanotubes exhibit no selectivity (both n-hexane and cyclohexane are observed to enter the SWCNT (Figure 3-19) while (6,5)-SWCNT exhibits selectivity allowing only n-hexane to enter the nanopore.
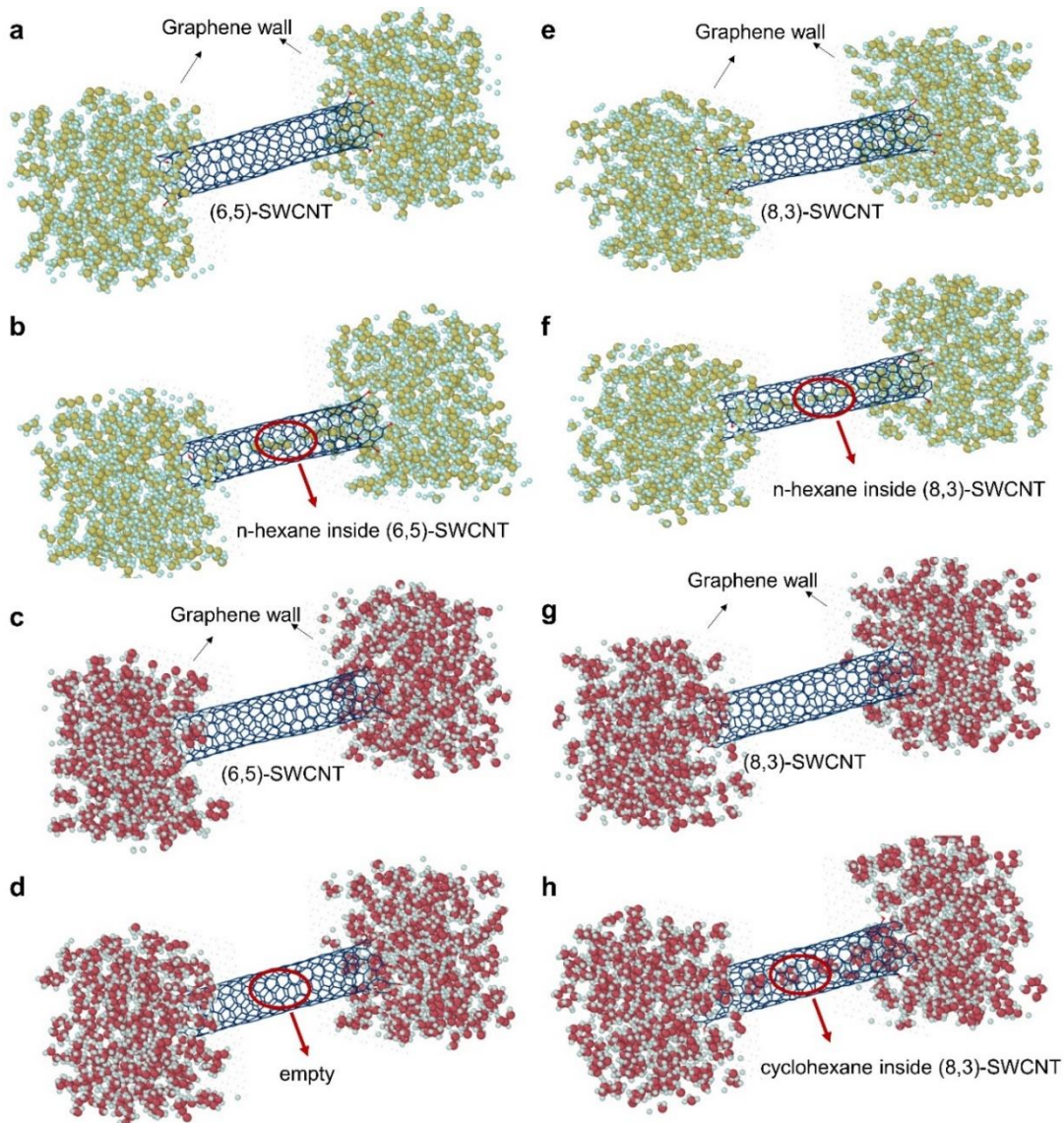
Figure 3-19. MD simulations at 300 K, 1 atm of (6,5)- and (8,3)-SWCNT incubated with n-hexane or cyclohexane. a, A (6,5)-SWCNT placed in an n-hexane bath at t=0. b, Single file of n-hexane molecules filling in the pore of (6,5)-SWCNT at the final step t ≈ 200 ps (Supplementary movie 3). c, A (6,5)-SWCNT placed in a cyclohexane bath at t=0. d, Empty (6,5)-SWCNT at the final step t ≈ 200 ps (Supplementary movie 4). e, A (8,3)-SWCNT placed in an n-hexane bath at t=0. f, Single file of n-hexane molecules filling the (8,3)-SWCNT at the final step t ≈ 200 ps (Supplementary movie 5). g, A (8,3)-SWCNT placed in a cyclohexane bath at t=0. h, Single file of cyclohexane molecules filling the (8,3)-SWCNT at the final step t ≈ 200 ps (Supplementary movie 6). In all these snapshots, carbon atoms of n-hexane are depicted in yellow, carbon of cyclohexane depicted in maroon, hydrogen in light blue, (6,5)- and (8,3)-SWCNTs in dark blue. Note that the dimension of the cyclohexane (or n-hexane) bath is $2.5 \times 2.5 \times 2.5$ nm^3, and the length of the SWCNT is 4 nm.

70

3.6 Methods

3.6.1 Process to Uncap the Carbon Nanotubes

To enable filling of SWCNTs, I modified a published procedure[130] to maintain the nanotube length while removing the capped ends. 60 mg of cobalt-molybdenum catalyst (CoMoCat) SG65 SWCNTs (Sigma Aldrich, lot MKBS9734V)[145] were placed on a glass slide and oxidized at $\approx$300 $^\circ$C in air for 30 min and kept at the same temperature under 0.1 MPa (1 atm) of argon for 30 min, resulting in a 15 % mass loss.

3.6.2 Endohedral Filling of Alkanes

A powder of the uncapped SWCNTs ($\approx$50 mg) was placed in a 10 mL round bottom flask with 5 mL n-hexane ($\geqslant$ 99.0 % Uvasol®, Sigma Aldrich, lot K49581572804) or 5 mL cyclohexane (99.9 %, Fisher Scientific, lot 176413), which was then incubated at 55 $^\circ$C for 48 h. The mixture was then incubated for 48 h at 55 $^\circ$C, which is below the boiling points of both n-hexane and cyclohexane, with the aid of a condenser to minimize evaporation. Post incubation, the mixtures were filtered (Millipore VVLP membrane, 0.1 μm pore size) to separate the bulk liquid from the solid nanotubes. The resulting cake, (2 to 10) mg, was manually crumbled loose and placed in a vacuum chamber for 24 h at room temperature to evaporate any residual alkane sticking to the outer walls of the nanotubes.

3.6.3 Carbon Nanotube Dispersion Process

For ensemble spectroscopy measurements, I dispersed ≈ (1 to 2) mg nanotubes in 2 mL of 10g/L sodium deoxycholate (DOC) in D_2O by ultrasonication with a power of 4 W and at 10 °C for 30 min, followed by centrifugation at 25000 g (1717 rad/s, 16400 rpm) for 1 h (Eppendorf centrifuge 5417 R). In the case of separating empty nanotubes from water-filled ones by density gradient ultracentrifugation (as described in the next section), the ultrasonication power was lowered to 0.5 W/mL solution.

To obtain long and molecule-filled nanotubes for hyperspectral imaging, I performed a superacid surfactant exchange (S2E), as previously reported[146], in order to avoid ultrasonication that can cut nanotubes. Briefly, the alkane-incubated SWCNTs were dissolved in chlorosulfonic acid (Sigma-Aldrich, 99.9 %) at a concentration of ≈ 0.2 mg/mL and the mixture was then added drop-by-drop to a solution of 0.75 mol/L NaOH and 0.8 g/L DOC (Sigma-Aldrich, ⩾ 97 %) aqueous solution until the solution pH decreased to ≈ 8. To concentrate the SWCNTs, the pH of the solution was then tuned to ≈ 6 by adding HCl (1 mol/L) to coagulate the SWCNTs. The precipitates were then collected and redispersed in Nanopure™ water by increasing the pH to ≈ 7 to 8 with NaOH solution (1 mol/L). The final concentration of DOC was 20 g/L. Undissolved particulates were then removed by centrifuging the solution at 23264 g (1467 rad/s, 14000 rpm) for 60 min on a benchtop centrifuge (Eppendorf Centrifuge 5810R). (Safety note: the neutralization process of the chlorosulfonic acid is extremely aggressive and should be performed in a fume hood with proper personal protective equipment, including goggles, lab coats, and acid-resistant gloves, due to the generation of a significant amount of heat and fumes.)

3.6.4 Separation of End-Capped SWCNTs by Density Gradient Ultracentrifugation

To obtain the end-capped empty SWCNTs, I used a density gradient ultracentrifugation procedure[127] to separate the empty SWCNTs from those that were water-filled based on their density differences. Due to the absence of end-capped empty SWCNTs in CoMoCat SG65, which was only available as chemically purified material, I used raw HiPco SWCNTs (NoPo Nanotechnologies, LOT: R118-0810) dispersed at a concentration of 20 g/L ($\approx$ 2 %) DOC/H_2O by mild sonication (45 min, 6 mm tip, $\approx$ 0.9 W/mL) then centrifugation for 2 h with a JA-20 rotor at 39086 g (1885 rad/s, 18000 RPM) to prepare a stock solution for this purpose. The SWCNTs in 2 % DOC were layered on top of 4 mL of 10 % (mass/volume) iodixanol (OptiPrep, Aldrich), 1 % DOC/H_2O and centrifuged using a VTi 65.2 rotor (Beckman-Coulter) operated at 414829 g (6807 rad/s, 65000 RPM) for 1 h at 20 ^{o}C. The enriched empty SWCNTs were collected from the top of the band in the middle of the tube. The iodixanol was removed by ultrafiltration through a 30 kDa membrane (Millipore 8003).

3.6.5 Characterization

To probe the optical properties at the ensemble level, the filled-SWCNTs were further diluted in 2 mL of 10 g/L DOC in D_2O. Samples were diluted in 10 g/L DOC in D_2O to avoid the absorption of H_2O at $\approx$ 1200 nm, which is very close to the SWCNT PL emission range.

The PL was collected using a NanoLog spectrofluorometer (Horiba Jobin Yvon). The samples were excited with a 450 W Xenon source dispersed by a double-

grating monochromator. The slit width set bandpass of the excitation and emission beams were both set to 10 nm. PL spectra were collected using a liquid-N_2 cooled linear InGaAs array detector. The emission spectra were collected with excitation light at the E_{22} wavelength of each specific chirality. The integration time for the 1D and 2D spectra were 2 s to 60 s and 5 s, respectively. Note that all samples had an optical density at the E_{11} band of less than 0.5 (A/cm), measured using a PerkinElmer Lambda 1050 spectrophotometer with a broadband InGaAs detector.

The Raman spectroscopy was performed using a LabRAM ARAMIS Raman microscope (Horiba Jobin Yvon) with an 1800 or 2400 groove/cm grating, 532 nm laser excitation (46 mW), and a 1.0 neutral density filter to prevent sample damage. The integration time was 1 s, taken 10 times in total. The dispersed nanotube solution was precipitated with ethanol and then deposited on a Si substrate, which simultaneously served as a reference with the Si peak at 520.7 cm-1 during the measurement.

To demonstrate the selective filling, the samples were prepared for GC-MS analysis as follows. 50 μL of n-hexane was mixed with 50 mL cyclohexane to prepare a 0.1 % n-hexane in cyclohexane (vol:vol) solution. A powder of end-opened SWCNTs (from CoMoCat SG65 nanotubes, which contains a mixture of chiralities, but the majority of the sample is (6,5)-SWCNT) with different masses was placed in 3.7 mL vials with magnetic stir bars. 2 mL of the 0.1 % n-hexane in cyclohexane solution was added to each vial. The vials were sealed with a cap and Parafilm®. The whole system was stirred at room temperature for 7 days to ensure it reaches equilibrium. Note: the boiling points of n-hexane and cyclohexane are 68.7 °C and 80.7 °C, respectively.

Therefore, a sealed system was used to minimize any potential bias possible from differential evaporation. After incubation with different amounts of SWCNTs, the nanotubes were removed by filtration using a Millipore VVLP membrane (0.1 μm pore size). The purity of cyclohexane was analyzed in a GC auto sampler vial within 5 min to minimize the evaporation

The GC-MS measurements were performed on an Agilent 6890N system coupled with a JEOL high-resolution magnetic sector mass spectrometer (JMS-700 MStation) with an electron ionization (EI) source (70 eV). The mass spectrometer was operated in the mode of high scan speed with a mass range from (50 to 200) Daltons. A silica capillary column (Agilent DB-17MS, 30 m length, 250 μm I.D.) was used in the experiments with helium (at 1 mL/min) as the carrier gas. The analysis was performed as follows: injection volume = 1 μL, splitless mode for the 99.9% pure commercial cyclohexane (Fisher Scientific, certified ACS, Lot 176413) and split mode (ratio = 1:20) for the mixture of n-hexane (Sigma Aldrich, Lot K49581572) and cyclohexane (volume:volume = 0.1:99.9), the front inlet temperature was 250 °C, the column temperature was programmed from 40 °C at 2.0 min, increased to 150 °C at a rate of 25 °C/min, then increased to 280 °C at a rate of 50 °C/min, and held at 280 °C for another 1.0 min. I used the fragmentation patterns obtained by EI to identify the structures of ions observed in the mass spectra based on the NIST mass spectral library[147]. To obtain the absolute concentration of n-hexane after the SWCNTs were incubated in the liquid mixture, I used toluene as an internal standard with a volume concentration of 0.1 % (volume/volume) to construct the calibration curve (Figure 3-12). The concentration of n-hexane was then calculated with the following equation:

$$C_{\text{n-hexane}} = \frac{A_{\text{n-hexane}}}{A_{\text{toluene}}} \times \frac{C_{\text{toluene}}}{\text{RF}} \qquad\qquad \text{Equation 3-3}$$

in which $C_{\text{n-hexane}}$ and C_{toluene} are the concentration in units of μmol/mL for n-hexane and toluene, respectively, and $A_{\text{n-hexane}}$ and A_{toluene} are the peak areas for n-hexane and toluene, respectively, and RF is the response factor.

3.6.6 Hyperspectral Photoluminescence Imaging

To collect single nanotube PL images, the filled-SWCNTs were dispersed in 10 g/L DOC in D_2O with an optical density (OD) of ≈0.1 at the E_{11} peak wavelength of (6,5)-SWCNT, then diluted 10-fold with 10 g/L DOC in D_2O. 5 μL of the diluted solution was then drop-cast onto a polystyrene coated Au on Si substrate. The polystyrene layer acts as an insulating layer to prevent the SWCNTs from contacting with the Au, which would quench the PL. The Au layer is added as a mirror to double the excitation and emission light. The hyperspectral imaging was performed on a custom-built microscope[128]. In the current experiments, I used an infrared optimized 100x objective (LCPLN100XIR, numerical aperture (NA) = 0.85, Olympus) along with a continuous wave laser at 730 nm (Shanghai Dream Lasers Technology Co., Ltd.) or 561 nm (Jive[TM] Cobolt AB, Sweden) as the excitation light source. Fluorescent emission from the sample was filtered through a long pass dichroic mirror (875 nm edge, Semrock, USA), which removed the elastic laser scattering from the sample, and dispersed by a volume Bragg grating (VBG; Photon Etc, Inc. Montreal, Canada). Only the diffracted light with a narrow bandwidth of 3.7 nm was collected on the detector to form a spectral image.

I exported the PL spectra from the hyperspectral cube and read out the coordinate or location for each fluorescent nanotube. The E_{11} peak position was obtained by fitting the spectrum from each pixel with a Gaussian profile (see Supplementary Note 1 and Figure 3-3) and I then reconstructed the peak positions along with spatial information as a color map image by MATLAB.

3.6.7 Molecular Dynamics (MD)

MD simulations were performed to simulate the molecular filling and calculate the distribution of the minimum projected diameter (Figure 3-17) of n-hexane and cyclohexane in bulk. These simulations used the Large-scale Atomic/Molecular Massively Parallel Simulator (LAMMPS)[148] MD toolkit. To simulate organic molecules in MD, I use the all-atom optimized potentials for liquid simulation (OPLS-AA) potential[149] to model carbon-carbon and carbon-hydrogen interactions. The atoms in the SWCNT are simulated using the Adaptive intermolecular reactive empirical bond order potential (AIREBO)[150]. Interactions between carbon in the SWCNT and carbon and hydrogen in hexane and cyclohexane are modeled using the Lennard-Jones potential[151] with parameters given in Table 3-4. The parameters for carbon were taken from ref.[150] and hydrogen were taken from ref.[152] and oxygen were taken from ref.[153]. The SWCNTs are terminated with -OH groups, and the pressure is maintained at 0.1 MPa (1 atm) and temperature at 300 K to model the experimental conditions. To identify the threshold at which the hexane enters whereas cyclohexane cannot, MD simulations were performed for the cyclohexane, hexane, and SWCNT systems ((6,5)-, (8,3)-, (7,5)-, (8,4)-, (7,6)-, (9,4)- SWCNT) with the angle parameters for n-hexane and cyclohexane completely relaxed to account for large conformational changes in

these molecules (Figure 3-13 and Figure 3-19). The configurations to calculate the distribution of the projected diameter in Figure 3-17 were collected from the simulations of n-hexane/cyclohexane placed in a bath of volume $2.5 \times 2.5 \times 2.5$ nm^3 at 300 K and 0.1 MPa (1 atm). The simulations are equilibrated for 5 ns, before post-processing is done to bin the molecules based on their projected diameter. A time step of 0.25 fs was used, with data being sampled every 100 timesteps and the system was run until enough statistics were obtained to ensure a smooth distribution (n-hexane system was run for $\approx$ 125 ps and the cyclohexane system for $\approx$ 600 ps). The damping parameters used in LAMMPS for the thermostat and barostat are 2.5 fs and 25 fs, respectively, under the NPT ensemble during the production run.

Table 3-4. Lennard-Jones parameters used in MD simulations.

Atom pairs	σ (Å)	ε (eV)
C-C	3.4	0.00286
C-O	3.024	0.0049
C-H	2.9	0.00192
O-H	3.166	0.00667
O-O	3.166	0.00667
H-H	2.4	0.00129

3.6.8 Density Functional Theory (DFT)

DFT was used to optimize the geometries used in AIMD simulations (described in the next section) and to verify that the minimum projected diameter of n-hexane and cyclohexane in their relaxed state (most probable configuration) match with the results obtained from MD. These simulations are performed using the Vienna Ab initio Simulation Package (VASP)[154]. The Perdew−Burke-Ernzerhof (PBE) functional[155] is used for exchange correlation energy. A $1 \times 1 \times 4$ grid has been used in these simulations along with an energy cut-off of 400 eV. Convergence with respect to the

grid size and the energy cut-off is shown in Supplementary Figure 14. I note that using

400 eV, the energy difference is 2.91 eV from the converged value, which occurs at an

energy cut-off of 500 eV, but the latter simulation is $\approx$ 40 % more expensive, which

is why 400 eV was chosen as a compromise. It was verified that the optimization of the

n-hexane and cyclohexane geometries leads to positive vibrational frequencies only

and that the projected diameters of the most probable configurations of n-hexane and

cyclohexane are in agreement with those obtained from MD (0.28 nm and 0.4 nm,

respectively).

3.6.9   Ab initio Molecular Dynamic Simulations (AIMD)

AIMD simulations were performed to show that n-hexane moves into (6,5)-

SWCNT only when it is stretched (Figure 3-16) and to calculate the accessible pore

size of (6,5)-SWCNT (Figure 3-15). These simulations were performed for the n-

hexane and (6,5)-SWCNT systems starting from two configurations: (1) n-hexane

(both stretched and unstretched) is placed at the pore mouth; (2) stretched n-hexane

placed inside the SWCNT, away from the hydroxyl groups at the pore mouth. The

modeled (6,5)-SWCNT has 1-unit cell consisting of 364 carbon atoms, with an

additional 44 atoms of hydroxyl groups (-OH) at the end of the nanotube. In total, the

systems have 428 atoms with the volume of the simulation box being 22.5×22.5×80

Å^3. The starting geometry of the stretched n-hexane molecule is calculated from MD

simulations by relaxing all the angle parameters, allowing the molecule to freely stretch

within the nanotube pore. AIMD simulations were performed in VASP and all the

parameters used were same as those used for geometry optimization in DFT (mentioned

in the previous section). In addition, the isothermal-isobaric ensemble was used, with

79

the temperature and pressure maintained at 300 K and 0.1 MPa (1 atm). For the system

described in the first configuration, the simulations were performed until it was

sufficient to determine whether the molecule was being excluded or not, which is ≈ 2

ps as shown in Figure 3-16.

4 Reconfiguring Organic Color-Centers on the sp^2 Carbon Lattice of Single-Walled Carbon Nanotubes

This chapter is adapted from the following published manuscript: Qu, H.; Wu, X.; Fortner, J.; Kim, M.; Wang, P.; Wang, Y., Reconfiguring Organic Color Centers on the sp^2 Carbon Lattice of Single-Walled Carbon Nanotubes. ACS Nano 2022, 16, 2077-2087.

Y.H.W., and H.Q., conceived and directed the research. H.Q., and X.W., performed the experiments, H.Q., K.M., and J.F. performed DFT simulations. All authors contributed to data analysis. H.Q. and Y.H.W. wrote the manuscript with inputs from all co-authors.

4.1 Introduction

Organic color-centers (OCCs) are quantum defects that can be synthetically incorporated into single-walled carbon nanotube (SWCNT) hosts by covalently attaching organic functional groups to the sp^2 carbon lattice.[55, 58, 59, 156, 157] These sp^3 defects are exciton traps that produce bright photoluminescence (PL) in the shortwave infrared. This defect emission, labeled as E$_{11}$$^-$, is distinctly different and redshifted from the E$_{11}$ exciton PL native of the nanotube host.[59, 65] Notably, the E$_{11}$$^-$ PL emission energy can be molecularly tuned in the near-infrared range by changing either the OCC functional group or nanotube chirality.[59, 158] Furthermore, some OCCs have been shown to generate single photons at room temperature with a high purity of 99% along with excellent photostability.[21, 159] Additionally, these single photons can occur in the telecom O-band with high indistinguishability,[19] making OCCs a promising candidate for solid-state quantum technologies.[160] However, all known chemistries used to

generate OCCs produce a variety of bonding configurations that result in a broad distribution of multiple emission peaks,[55, 58, 59, 64-66, 68, 70, 157] which pose a significant materials and synthetic challenge to solid-state quantum technologies.

The diverse atomic configurations of OCCs arise from addition reactions to the double bonds of the graphitic host, which can produce a pair of functional groups for every OCC in various possible bonding configurations. For example, diazonium chemistry, the most widely used approach for generating OCCs,[59, 62, 65, 66] is believed to leave a reactive carbon at either the adjacent (ortho) positions or three carbons away (para) from the first bonding carbon.[67] These reactive species then presumably bond to an available H or OH group to complete the reaction.[20, 67] This pair of functional groups may take one of many possible positions on the sp^2 carbon lattice, resulting in a large number of bonding configurations that are chemically, thermodynamically, and energetically distinct.[20, 68, 69] As a result, multiple OCC emission peaks are observed when carbon nanotubes, such as (6,5)-SWCNTs, are modified with diazonium chemistry, producing a broad distribution of OCC emission peaks in the range of 1100–1350 nm, even for the same functional groups on the same (6,5) chirality.[70] Previous work by us and others have shown that the bonding configurations can be reduced by choosing atomically symmetric SWCNT hosts (*i.e.*, (n, 0) nanotubes),[20] divalent bonding groups,[58, 161] or via thermal annealing (at 500 °C for over 80 min).[162] However, these methods only work for zig-zag SWCNTs, which have a low abundance and purification yield,[52] or result in significant loss of the material (25–34% by weight) and substantial removal of OCCs from the SWCNT surfaces.[162] Furthermore, none of these approaches allows for localized control of the bonding configuration, which will be

required to study the coupling effect of identical quantum defects. A method that can be generally applied to all semiconducting SWCNT hosts to reconfigure the defect structure, ideally locally so it could potentially be integrated with molecular patterning,[163] would provide a powerful means for controlling the atomic configuration and thus quantum emission and coupling of OCCs.[55, 156]

Herein, I show that laser irradiation of OCC-SWCNTs can locally convert kinetic configurations of the OCC functional group pair to the more thermodynamically stable structure, leading to a single defect PL peak. This process is driven by a laser that resonantly excites the SWCNT host at its E_{22} excitonic transition to promote local rearrangement of the OCC bonds while keeping the carbon lattice intact (Figure 4-1). I confirmed this structural transformation by measuring the change in the OCC PL at both the ensemble and individual nanotube levels, which show significantly narrowed distribution of the OCC emission peaks by ~26%. Density functional theory (DFT) and time-dependent DFT (TD-DFT) simulations suggest that OCCs with kinetic configurations transform into the more thermodynamically stable ortho structure upon laser irradiation, with the calculated spectral shifts resulting from this structural rearrangement in good agreement with the observed experimental trends. These findings demonstrate the feasibility to locally reconfigure OCCs, providing a possible synthetic approach to achieve identical quantum emitters.
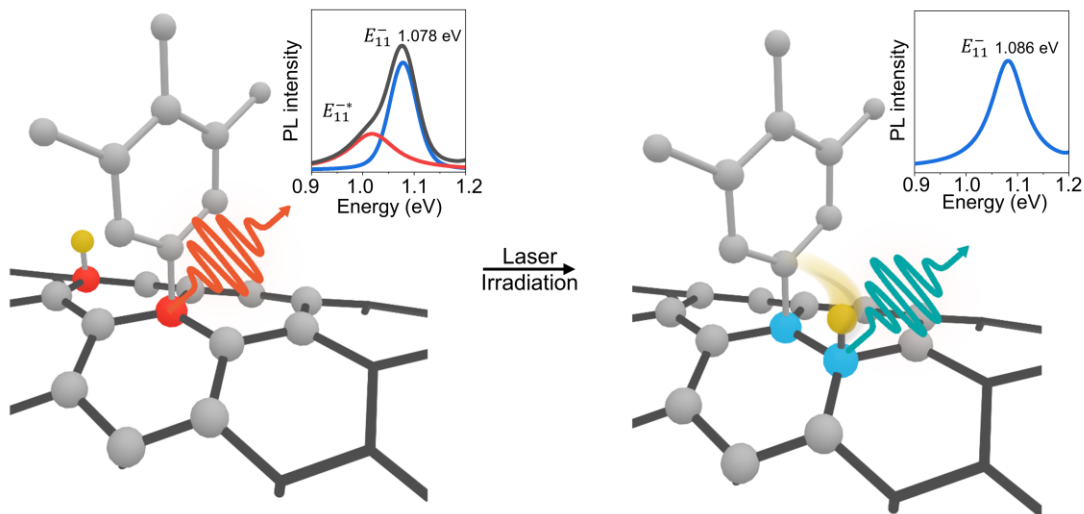
Figure 4-1. Laser irradiation transforms kinetic bonding configurations of OCCs to the thermodynamically stable structure on the sp2 carbon lattice of semiconducting carbon nanotubes. The schematic shows an OCC that consists of an aryl group along with a pairing –H group (yellow atom) covalently attached to the sidewall of a (6,5)-SWCNT. The pairing -H group can attach to carbon at different location (an example of para configuration is shown on the left), such variety of possible bonding configurations can generate multiple emission peaks (left inset). However, irradiation with an E22 resonant laser restructures the OCC, changing the pair of functional groups from the kinetic to thermodynamic configuration (e.g., from para to ortho bonding). As a result, the OCC PL emission narrows and blueshifts (insets).

4.2 Results and Discussion

I synthesized model OCC-SWCNTs by covalently attaching 3,4,5-trifluoroaryl groups on CoMoCat (6,5)-SWCNTs using a scalable, aqueous diazonium chemistry[65] followed by purification (see Methods for more details). Excitation-emission PL mapping of the resulting OCC-(6,5)-SWCNT solution revealed three major peaks (Figure 4-2a), including the E_{11} PL of the nanotube host at ~987 nm and convoluted OCC PL bands centered at ~1150 nm (E_{11}^-), as well as a sideband extending from 1200 nm to ~1300–1400 nm, which we label as E_{11}^{-*}. These defect-induced emissions are broad and complex. However, I found that continuous irradiation of the OCC-(6,5)-SWCNT solution at room temperature with 565 nm light, which resonantly excites the

E_{22} band of the (6,5)-SWCNT host (Figure 4-2b), changes both the position and intensity of the OCC peaks (Figure 4-3a). Over the course of irradiating the sample (265 s), I observed 2 stages in the change of E_{11}^- in real-time. During the first 50 seconds of irradiation, the intensity of the E_{11}^- emission decreased, followed by a gradual increase of the intensity (Figure 4-3b). Meanwhile, the E_{11}^- wavelength blueshifted from 1153 nm (1.075 eV) to 1142 nm (1.085 eV) over the first 50 s and then stabilized at ~1142 nm (Figure 4-3c). Notably, the E_{11}^{-*} sideband centered at 1218 nm (1.018 eV), which can be better resolved by fitting the PL spectra with Voigt functions (Figure 4-4), disappeared after irradiation. I observed a similar reduction of E_{11}^{-*} with 4-nitroaryl OCCs on (6,4)-SWCNTs (Figure 4-5), suggesting this phenomenon may be generalizable to other chiralities and OCCs. However, in this work, I chose to focus on 3,4,5-trifluoaryl OCCs on (6,5)-SWCNTs as a model system, since 3,4,5-trifluoaryl is less prone to possible polymerization,[164] which can complicate the interpretation, while (6,5)-SWCNT is the most studied chirality in the literature.
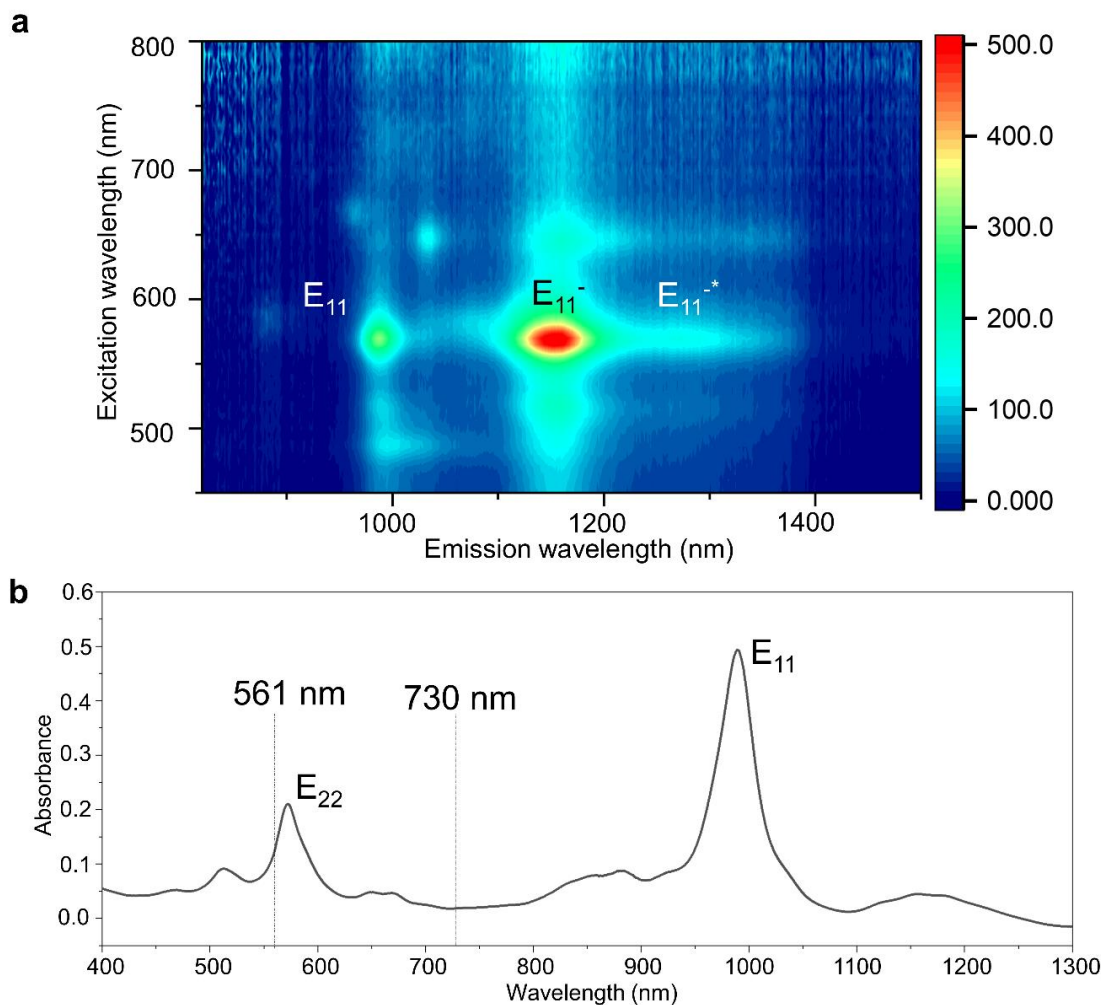
Figure 4-2. The optical properties of the OCC-(6,5)-SWCNTs. a, A PL map of the OCC-(6,5)-SWCNTs. b, The absorption spectrum of OCC-(6,5)-SWCNTs after purification. The E_{22} band peaks at ~570 nm and the E_{11} band peaks at ~988 nm. The molar extinction coefficient at 561 nm is 10-times higher than that at 730 nm.
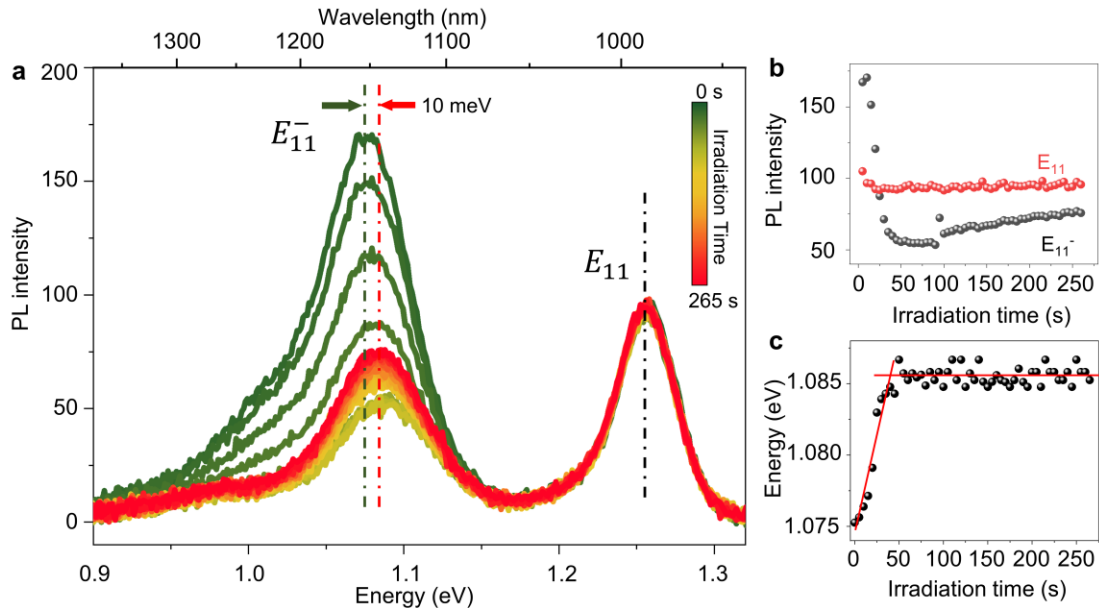
Figure 4-3. Spectral shifts in the OCC peak emission under light irradiation. a, Ensemble PL measurements of OCC-(6,5)-SWCNTs dispersed in 2 w/v% DOC/H_2O solution and irradiated by 565 nm light at ~10mW/cm^2 for increasing time. Unlike the native SWCNT E_{11} emission peak at 988 nm, which remains unchanged, the OCC E_{11}^- wavelength shifts from ~1153 nm to ~1142 nm over 265 s of laser excitation. Additionally, the overall OCC emission intensity decreases. b, Comparison of the E_{11} and E_{11}^- emission intensity as a function of the irradiation time. c, Evolution of the E_{11}^- peak wavelength as a function of the irradiation time.
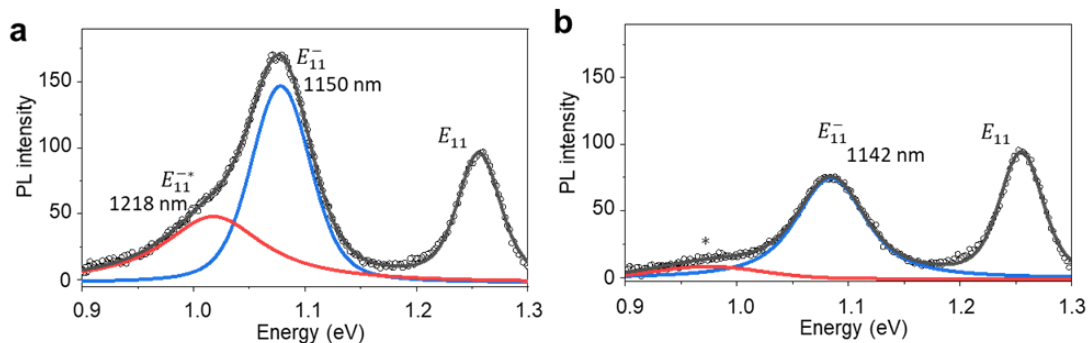
Figure 4-4. Deconvolution of the ensemble PL spectra of OCC-(6,5)-SWCNTs. a, The OCC emission before laser irradiation showed two OCC peaks at 1150 nm (E_{11}^-) and 1218 nm (E_{11}^{-*}), respectively. b, The OCC emission after 265 s of irradiation with 565 nm light at ~10 mW/cm^2, in which only the E_{11}^- peak at 1142 nm remains. The integration time of each spectrum was set to 0.01 s to minimize changes to the OCCs during the spectral measurement. The black circles indicate the original data points, while the black curve is the cumulative curve obtained from the Voigt fittings of E_{11} (not shown), E_{11}^- (blue), and E_{11}^{-*}(red). The small tail (marked by *) may be due to minor amounts of (8,4)-SWCNT impurities in the solution. Our individual SWCNT PL measurements did not observe this small peak from OCC-(6,5)-SWCNTs.

87
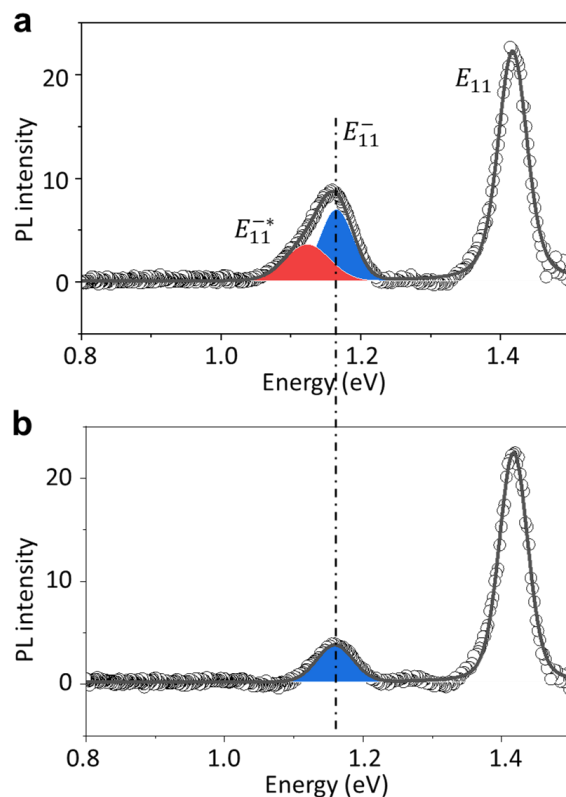
Figure 4-5. Ensemble PL spectra of OCC-(6,4)-SWCNTs irradiated with 570 nm light for 300 s. PL spectra of (6,4)-SWCNTs functionalized with 4-nitroaryl groups (a) before and (b) after irradiation with 570 nm light for ~300 s to demonstrate that this irradiation effect can be adapted to other chiralities and functional groups. The E_{11}^{-*} intensity decreases and the E_{11}^{-} peak remains after irradiation. This is consistent with the observation in 3,4,5-trifluorobenzene functionalized (6,5)-SWCNTs.

To identify the reason behind these observed changes in the defect PL upon irradiation with 565 nm light, I first ruled out several possibilities. I note the 3,4,5-trifluoaryl group is resistant to further chemical reactions due to its strong C-F bonds,[164-166] making it unlikely that the OCC functional group itself has changed during the irradiation process. I further prevented ultraviolet (UV) photon-triggered side reactions[64, 167-170] by removing the UV photons from the incident light source using a 400 nm long path filter. The irradiation of 565 nm light on pristine (6,5)-SWCNTs under our experimental condition does not generate defect emissions (Figure 4-6). I also coated the SWCNTs with sodium deoxycholate (DOC), a surfactant known to

prevent other potential reactants in solution from gaining access to the graphitic surface. Furthermore, I removed the excess diazonium reactant by ultrafiltration. Other possibilities that may contribute to the observed defect PL include trions[171, 172] and aryl-group-localized radical pairs.[173] Although our work does not fully rule out these possibilities, radicals from aryl OCC-tailored (6,5)-SWCNTs should be undetectable above 200 K.[173] Furthermore, I note that light-induced global heating effects should not be a major factor, as a previous study found the solution temperature remained nearly unchanged (within 0.6 °C) even after irradiating the sample using a 561 nm laser at ~1 W/cm^2 for 60 minutes.[174] Since the power density that I used here (Figure 4-3) is 100-times lower, I can conclude that the observed PL emission changes were not due to a global heating effect. Additionally, the stability of the E_{11} emission during irradiation further suggests that neither the endohedral nor exohedral environments of the nanotubes have changed.[34]
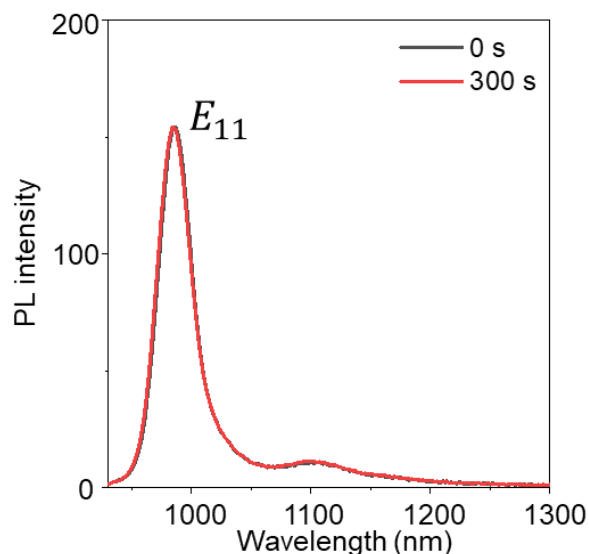
Figure 4-6. Control experiment ruling out potential side reactions due to laser irradiation. Pristine (6,5)-SWCNTs in 2 w/v % DOC solution were irradiated using the same conditions in Figure 2 for 300 s. No change in the PL spectrum was

observed, indicating irradiation alone does not generate new PL features. Note that the small peak at ~1100 nm is the phonon band of (6,5)-SWCNTs.

Having ruled out these other possibilities, I hypothesize the observed spectral changes of the OCCs are due to bonding reconfigurations triggered by the E_{22} resonant irradiation of the nanotube hosts. Excitation of the (6,5)-SWCNT E_{22} transition generates mobile excitons that are known to relax to the nanotube's lower E_{11} energy level, as shown in Figure 4-7. The intrinsic E_{11} emission displays a low quantum yield of just ~1%,[54] with ~99% of the absorbed photon energy lost to the dark states and releasing as heat that is expected to heat up the entire length of the nanotube. Alternatively, in the presence of OCCs, the E_{11} excitons can be efficiently channeled to these defect sites, where the excitons are trapped at the lower E_{11}^- or E_{11}^{-*} energy levels, with the difference in energy compared to the original E_{11} state of the mobile exciton being locally released as heat at the OCC sites.[69] Although I cannot rule out the possibility of an exciton-induced photoreaction that could cause reconfiguration of the OCC bonding, if this does occur, it will be a surprisingly rare example that is triggered by an exciton rather than direct excitation with a photon. For these reasons, I hypothesize that the thermal energy generated locally at the OCC sites (as opposed to the temperature of the bulk solution) could be sufficient to trigger rearrangement of different kinetically-derived bonding configurations of the OCCs to fewer, more thermodynamically stable structures that would result in the observed narrower distribution of the defect PL peaks.
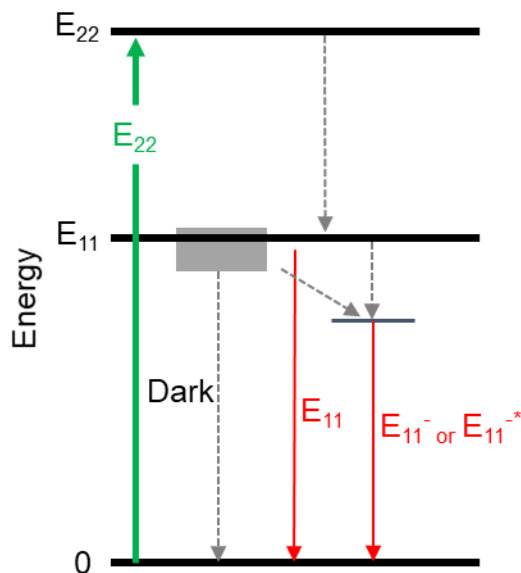
Figure 4-7. Jablonski diagram of OCC-(6,5)-SWCNTs. The solid arrows depict the optical excitation and emission transitions of interest. The dashed arrows denote nonradiative relaxation, which generates heat. The energy level of OCCs may shift due to change in bonding configuration.

During irradiation, these less stable OCCs appear to rearrange in two steps into a more stable bonding configuration that emits at 1140 nm. The first step is evidenced by the decreasing intensity of the E_{11}^- and E_{11}^{-*} peaks during the first 50 s of irradiation, narrowing into a single E_{11}^- peak (Figure 4-4). The second step is characterized by the slow increase of the E_{11}^- intensity in addition to the peak's slight blueshifting (12 meV) upon continued 565 nm irradiation (> 50 s) (Figure 4-3). These results suggest that the number of kinetic bonding configurations is reduced, eventually converging into the most thermodynamically stable structure, as exemplified by the single, narrowed, and somewhat blueshifted E_{11}^- emission peak that remains at the end of the irradiation process. This phenomenon could explain why E_{11}^- is typically observed as a major peak in OCC-functionalized (6,5)-SWCNTs synthesized by light-accelerated chemistries,[62, 64] in which the kinetically stable OCCs may already be converted into thermodynamically stable OCCs.

91

To more directly follow the evolution of the OCC configuration, I conducted *in situ* hyperspectral PL imaging of individual OCC-(6,5)-SWCNTs deposited on a substrate (see Methods).[175] To separate the irradiation effect from the PL measurement, I performed laser irradiation at a relatively high-power density of 184 W/cm^2 using a 561 nm laser, which resonantly excites the E_{22} band of the (6,5)-SWCNT host. Then I probed the PL at a low power density of 42 W/cm^2 using a 730 nm laser, which off-resonantly excites the nanotubes without changing the OCCs (Figure 4-2b and Figure 4-8). Figure 4-9a shows a PL image of an individual OCC-(6,5)-SWCNT with 2 OCC sites emitting at >1100 nm (1.13 eV) (indicated by the yellow circles) before and after 561 nm laser irradiation. The corresponding PL spectra from these 2 OCC sites before (top) and after (bottom) laser irradiation are shown in Figure 4-9b and Figure 4-9c, respectively. At site 1, I observed two peaks in the initial OCC emission, E_{11}^- at 1187 nm (1.044 eV) and E_{11}^{-*} at 1246 nm (0.995 eV). After irradiation for 30 min, the intensity of the E_{11}^{-*} peak significantly decreased, while the E_{11}^- peak blueshifted to 1171 nm (1.059 eV). Figure 4-10 shows more examples of the blueshifted E_{11}^- peak and decrease of E_{11}^{-*}. Out of 91 nanotubes investigated, I observed a blueshift of 34-58 meV from E_{11}^{-*} to E_{11}^- (Figure 4-10b-e and Figure 4-11). Additionally, no further changes were observed after the first 30 min of irradiation (Figure 4-10c). These trends are consistent with our ensemble solution-based measurements (Figure 4-3). However, the spectra of individual emitting sites, as shown in Figure 4-9a, demonstrate the diverse OCC structures that can be generated by the diazonium chemistry. Unlike at site 1, where both E_{11}^- and E_{11}^{-*} are present, site 2 only features the E_{11}^- peak, which blueshifts by 10 meV from 1124 nm (1.103 eV) to 1114 nm (1.113 eV) upon laser

irradiation (Figure 4-9c). Despite the observed spectral heterogeneity of the starting material, these findings further demonstrate the ability to modify the OCC emission wavelength by resonantly exciting the SWCNT host to predominantly achieve the E_{11}^- emission.
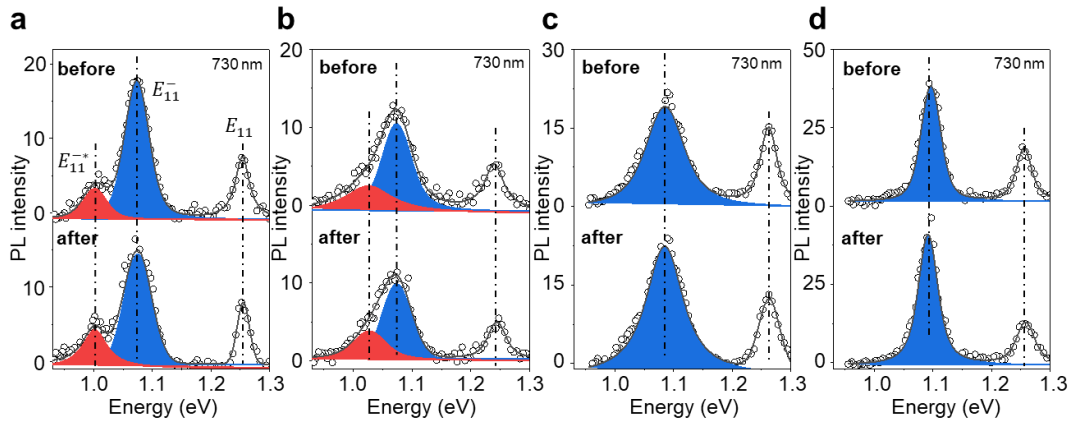
Figure 4-8. 730 nm laser excitation at 42 W/cm^2 does not induce OCC reconfiguration. PL spectra from four individual OCC-(6,5)-SWCNTs (a-d) with one or two OCC emission peaks during two consecutive spectral measurements with 730 nm excitation (top and bottom). In all cases, the OCC peaks show negligible change, confirming that the 730 nm laser does not modify the OCC emission.
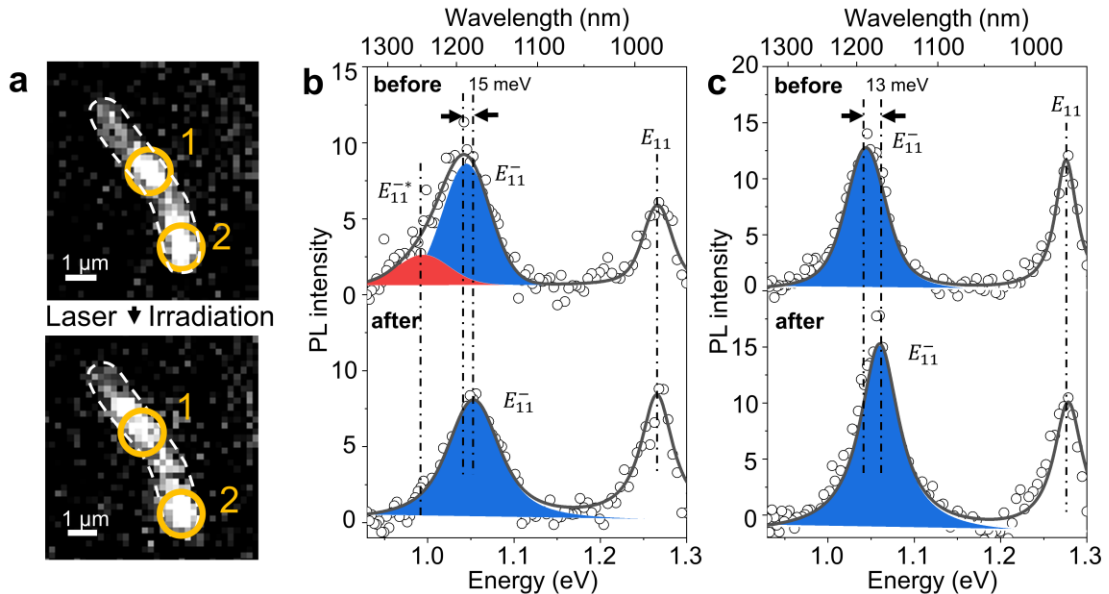
Figure 4-9. Changes in the PL of individual OCCs upon 561 nm laser irradiation. a, PL images of an individual OCC-(6,5)-SWCNT before (top) and after (bottom) irradiating with a 561 nm laser at a power density of 184 W/cm^2 for 30 min. These PL images were taken with a 1100 nm longpass filter and 730 nm excitation. b, The PL

spectra from site 1 (shown in (a)) before (top) and after (bottom) irradiation, in which the E_{11}^{-*} peak at 0.995 eV disappears while E_{11}^{-} blueshifts by 15 meV. c, PL spectra from spot 2 (shown in (a)) before (top) and after (bottom) irradiation, in which the E_{11}^{-} emission blueshifts by 13 meV.
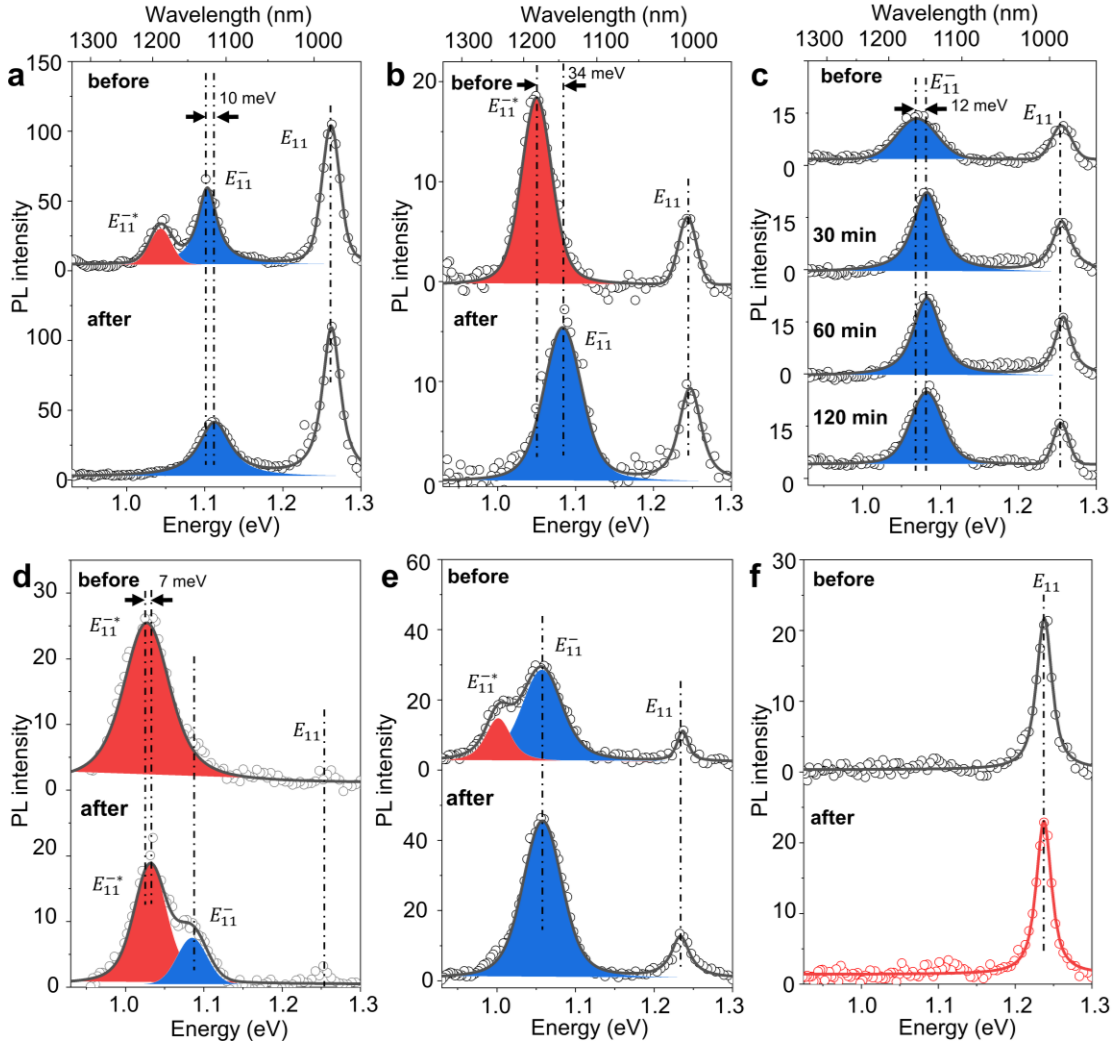
Figure 4-10. PL spectra of individual OCC-(6,5)-SWCNTs before and after laser irradiation. PL spectra of two individual OCC-(6,5)-SWCNTs (a-b) before (top) and after (bottom) irradiating with a 561 nm laser at a power density of 184 W/cm^2 for 30 min. (a) Irradiation removes E_{11}^{-*} at 1187 nm (1.044 eV), while E_{11}^{-} blueshifts by 10 meV, from 1124 nm (1.103 eV) to 1114 nm (1.113 eV). (b) The blueshift of E_{11}^{-*} to E_{11}^{-} after laser irradiation was 34 meV, specifically from 1181 nm (1.050 eV) to 1145 nm (1.083 eV). (c) PL spectra from an individual OCC-(6,5)-SWCNT before (top) and after (bottom) longer irradiation of up to 2 h using a 561 nm laser at a power density of 184 W/cm^2. These results demonstrated that under these conditions the OCC change occurs within the first 30 min and becomes stable after that. (d) PL spectra of an individual OCC-(6,5)-SWCNT predominantly featuring E_{11}^{-*} emission before (top) and after (bottom) irradiating with a 561 nm laser at a power density of ~37 mW/cm^2 for 30 min, which is comparable to the light power density of ~10

mW/cm^2 used in Figure 2. (e) PL spectra of an individual OCC-(6,5)-SWCNT featuring E$_{11}$$^-$ and E$_{11}$$^{-*}$ before (top) and after (bottom) irradiating with a 561 nm laser at a power density of ~1 W/cm^2 for 30 min. (f) The pristine (6,5)-SWCNT control shows that the irradiation process does not generate OCC defects, nor cause structural damage to the nanotube host.
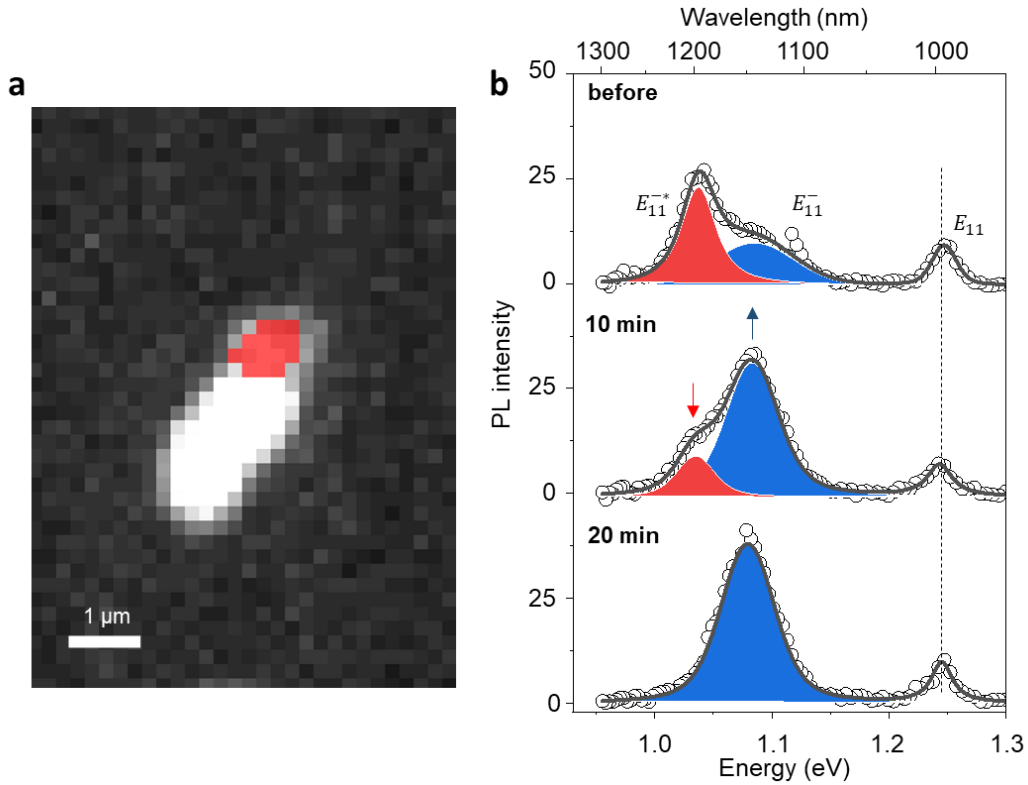
Figure 4-11. Conversion of E$_{11}$$^{-*}$ to E$_{11}$$^-$ on an individual OCC-(6,5)-SWCNT. a, A broadband image from 850–1550 nm of an OCC-(6,5)-SWCNT with the OCC emission (red) superimposed. b, PL spectra from the red area in (a) before and after 10 min and 20 min of 561 nm irradiation at a power density of 184 W/cm^2.

Additionally, as with the bulk measurements, the single-nanotube hyperspectral PL imaging showed the native E$_{11}$ peak of the majority of OCC-(6,5)-SWCNT remained nearly identical before and after irradiation (Figure 4-9, Figure 4-10, and Figure 4-11). Similarly, irradiating the pristine (6,5)-SWCNTs with 561 nm light caused no defect-induced emission peaks to appear and the position of the native E$_{11}$ emission was maintained (Figure 4-10f). The stability of the E$_{11}$ emission in the hyperspectral imaging experiments provides further evidence that the laser excitation

does not add nor remove OCC defects on the SWCNTs in these nanotubes. Therefore, the observed shifts and changes in intensity of E_{11}^- and E_{11}^{-*} are due to rearrangement of the OCC bonding configurations. I note in some rare cases (e.g., Figure 4-9b) the E_{11} intensity increases, while E_{11}^{-*} disappears, suggesting the removal of these OCCs. I also note that these defects are often characterized by Raman scattering as well, as shown previously.[59] However, due to the sparse density of defects on each nanotube, our Raman instrument does not have the sensitivity to detect the change that provides an unambiguous correlation with our PL measurements.

I wanted to further explore the mechanism behind these observed PL shifts and intensity changes of the E_{11}^- and E_{11}^{-*} peaks due to possible OCC bond rearrangement in the individual nanotube measurements. Once again, I were curious whether a global or local heating effect was the cause behind the observed shifts. During irradiation, I estimated that the nanotube temperature increased by less than 1 °C (Supplementary Note 4-1). Therefore, I can again exclude a global heating effect, which suggests the observed OCC bonding rearrangement is instead triggered by the local thermal energy generated by exciton trapping and relaxation at the OCC sites.

I further performed the irradiation using the 561 nm laser at two different power densities (Figure 4-10d-e). Irradiating an individual SWCNT that predominantly showed E_{11}^{-*} using the 561 nm laser at a power density of 37 mW/cm^2 caused the intensity of E_{11}^{-*} to decrease while the E_{11}^- peak at 1142 nm (1.085 eV) appeared (Figure 4-10d). Similarly, an individual OCC-(6,5)-SWCNT showed the E_{11}^{-*} intensity decreased while the E_{11}^- intensity increased after irradiation with 561 nm light at a power density of just 1 W/cm^2 for 30 min. Furthermore, I observed a gradual conversion

of E_{11}^{-*} to E_{11}^{-} when irradiated with 561 nm light at 184 W/cm^2 for 10-20 min (Figure 4-11). After 20 min irradiation, the E_{11}^{-*} peak completely disappeared while the intensity of E_{11}^{-} increased, becoming the dominant OCC emission. Meanwhile, the intensity of E_{11} did not change, indicating no new OCC defects had been added or removed. These results further suggest that the irradiation process converts OCCs that emit at E_{11}^{-*} to that emits at E_{11}^{-}.

To better quantify the impact of laser irradiation on the OCC emission shifts, I statistically assessed the OCC peaks of 67 individual nanotubes (Figure 4-12). I found the laser irradiation narrowed the OCC peak distribution by ~26%, reducing from 166 meV, which includes E_{11}^{-} (1129–1238 nm) and E_{11}^{-*} (1221–1330 nm), to 123 meV (1107–1245 nm) with E_{11}^{-} only. In general, I observed 3 types of nanotubes in terms of the change in their OCC emissions: (a) 38 out of the 67 nanotubes I measured exhibited only one OCC peak (E_{11}^{-}) and blueshifted by 9–34 meV after irradiation; (b) 23 of the 67 nanotubes showed both E_{11}^{-} and E_{11}^{-*} peaks, in which E_{11}^{-} blueshifted and E_{11}^{-*} diminished upon irradiation; (c) finally, OCCs from 6 of the nanotubes showed only E_{11}^{-} emission that remained stable (without shifting) upon laser irradiation (example is shown in Figure 4-13). This range of the E_{11}^{-} peak position even after irradiation can be attributed to the different environments of the nanotubes, both exterior and interior, in which the water molecules may partially evaporate from the SWCNT interiors at varying amounts (Supplementary Note 4-2).[34, 50] It is also worth pointing out that low-temperature PL measurements[68] in combination with single-defect spectroscopy[175] may provide additional details on the evolution of these OCCs under laser irradiation, which require future experiments. However, there is a clear trend from both ensemble and

individual nanotube PL measurements suggesting that the OCC configuration changes from a kinetically-derived structure to a more thermodynamically stable one upon irradiation with E_{22} resonant light.
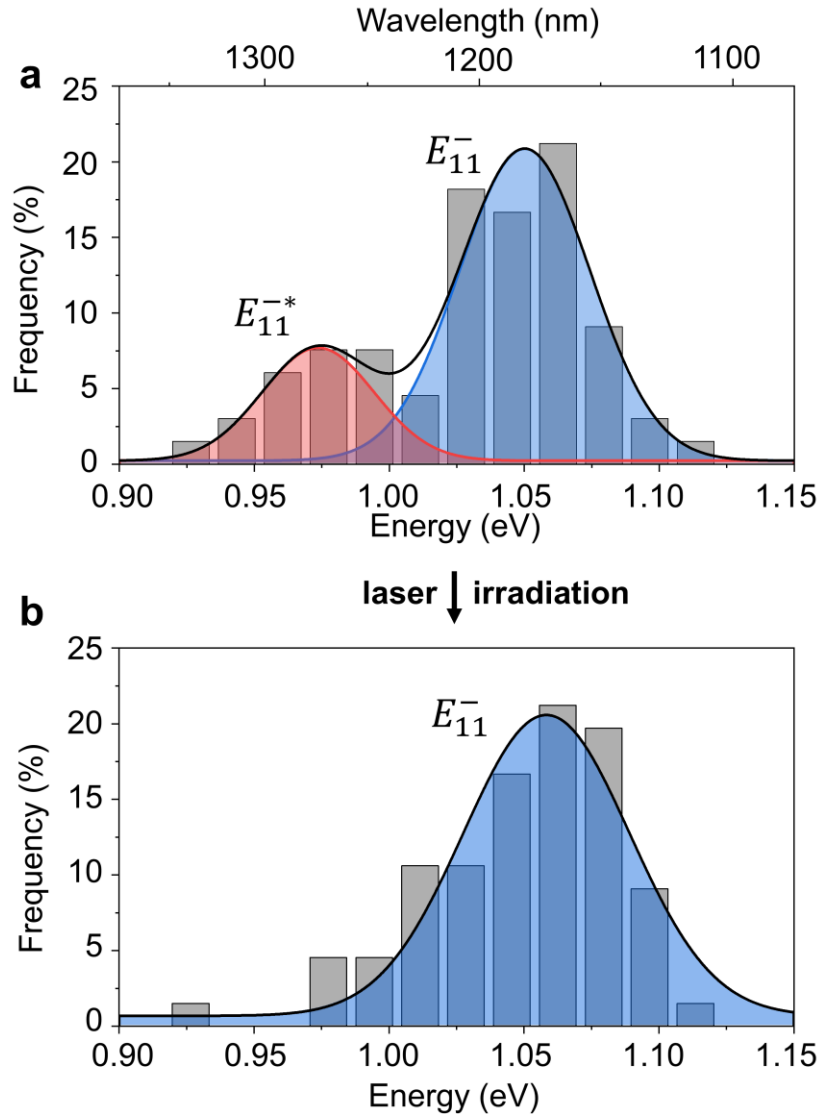
Figure 4-12. Statistical analysis of the OCC emission of 67 individual OCC-(6,5)-SWCNTs before and after laser irradiation. Histogram of the different E_{11}^- and E_{11}^{-*} emission energies observed of individual nanotubes a, before and b, after irradiating with a 561 nm laser at a power density of 184 W/cm^2 for 30 min. In total, 90 OCC peaks in these 67 (6,5)-SWCNTs were observed before irradiation, including 67 that featured the E_{11}^- peak and 23 that displayed E_{11}^{-*}. After irradiation, 13 of the E_{11}^{-*} peaks diminished and the number of OCC sites emitting at E_{11}^- increased by 6.
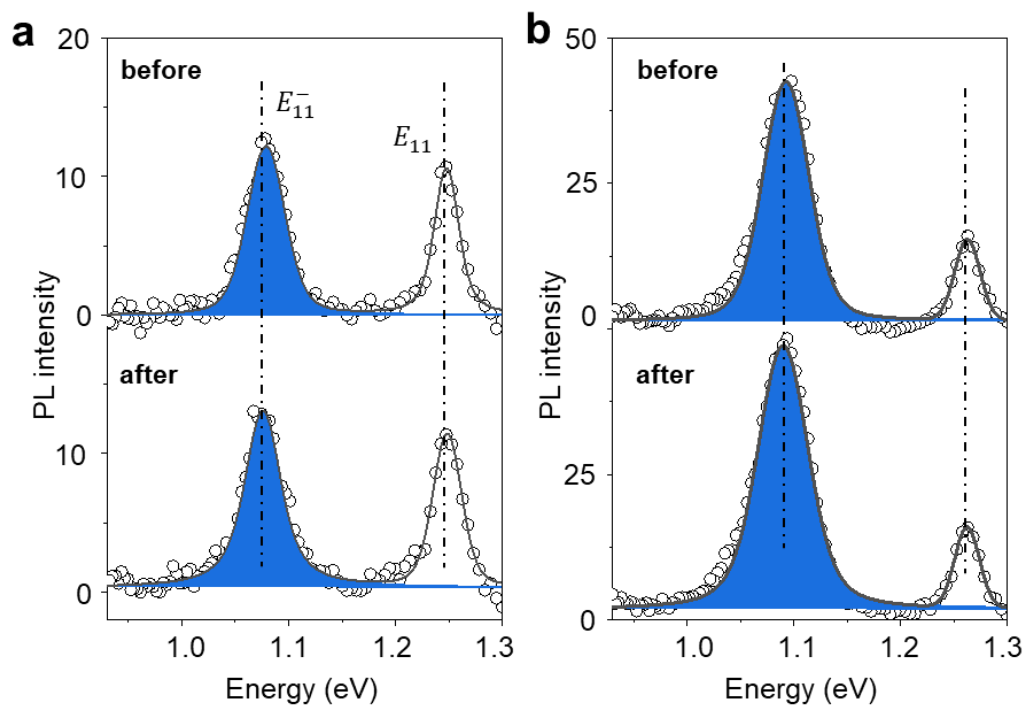
Figure 4-13. Examples of unchanged OCC emission after laser irradiation. a, PL spectra from two individual OCC-(6,5)-SWCNTs (a, b) before (top) and after (bottom) irradiating with a 561 nm laser at a power density of 184 W/cm^2 for 30 min.

To understand the configurational change of these quantum defects upon laser irradiation, I simulated the system energy of the OCC-SWCNTs using DFT calculations. I propose a naming convention to describe the rich structures afforded by these quantum defects, particularly OCC defect pairs. This naming system is inspired by the Miller index-like description of the sp^2 carbon lattice, which is widely used to distinguish the different (n,m) chiralities of tubular structures, such as carbon nanotubes and hexagonal boron nitride nanotubes, as well as graphene ribbons.[71] I define the position of the first defect as the origin, (0,0). The atomic configuration of an OCC can then be uniquely determined by the pairing position, PP(x,y), which follows $\overrightarrow{PP(x,y)} = x\,\overrightarrow{a_1} + y\,\overrightarrow{a_2}$, where $\overrightarrow{a_1}$ and $\overrightarrow{a_2}$ are the two base vectors for the sp^2 carbon lattice. With this naming system, I can identify each of the para and ortho defects, and any other

99

atomic configuration, for a specific nanotube host. For example, an "ortho" defect can actually take up to three distinct atomic configurations, which can be differentiated as PP(1/3, 1/3), PP(1/3, -2/3), and PP(-2/3, 1/3) on a (6,5)-SWCNT host (Figure 1-7). Similarly, the "para" configurations[72, 73] include PP(4/3, -2/3), PP(-2/3, -2/3), and PP(-2/3, 4/3). This naming system can be readily expanded to associate each atomic bonding position with the specific functional group along with the chirality of the nanotube host. A comparison of our naming system and existing ones[20, 68] is shown in Table 1-1. I note that such a rich structural variability may also occur with other low dimensional materials such as transition metal dichalcogenides and graphene ribbons,[74-76] and this naming system can similarly be applied to this increasingly rich family of atomic defects on different hosts.

I modeled six different configurations that contained the 3,4,5-trifluoroaryl group at the center of a 12 nm long (6,5)-SWCNT and a pairing hydrogen group attached to the adjacent carbon atoms, including 3 ortho positions (PP(1/3, -2/3), PP(-2/3, 1/3), and PP(1/3, 1/3)) and 3 para positions (PP(4/3, -2/3), PP(-2/3, -2/3), and PP(-2/3, 4/3)), as shown in Figure 4-14. I performed the geometry optimization of each OCC-SWCNT structure and calculated the system energies (see Methods). The ortho PP(-2/3, 1/3) configuration resulted in the lowest system energy among the tested structures, indicating it is the most thermodynamically stable bonding configuration. These results align with a previous simulation study by Tretiak and co-workers using H and 4-bromoaryl pairs as OCCs.[72] I found in our case that other configurations were 90–400 meV destabilized with respect to the ortho PP(-2/3, 1/3) position (Table 1). The difference in the total system energies suggest the structural stability of the OCC-

SWCNTs depends on the relative bonding configuration between the OCC and its pairing group. Furthermore, TD-DFT calculations confirm that each OCC bonding configuration produces an E_{11}^- emission 27 to 418 meV lower in energy compared to E_{11} (Table 4-1 and Figure 4-15).
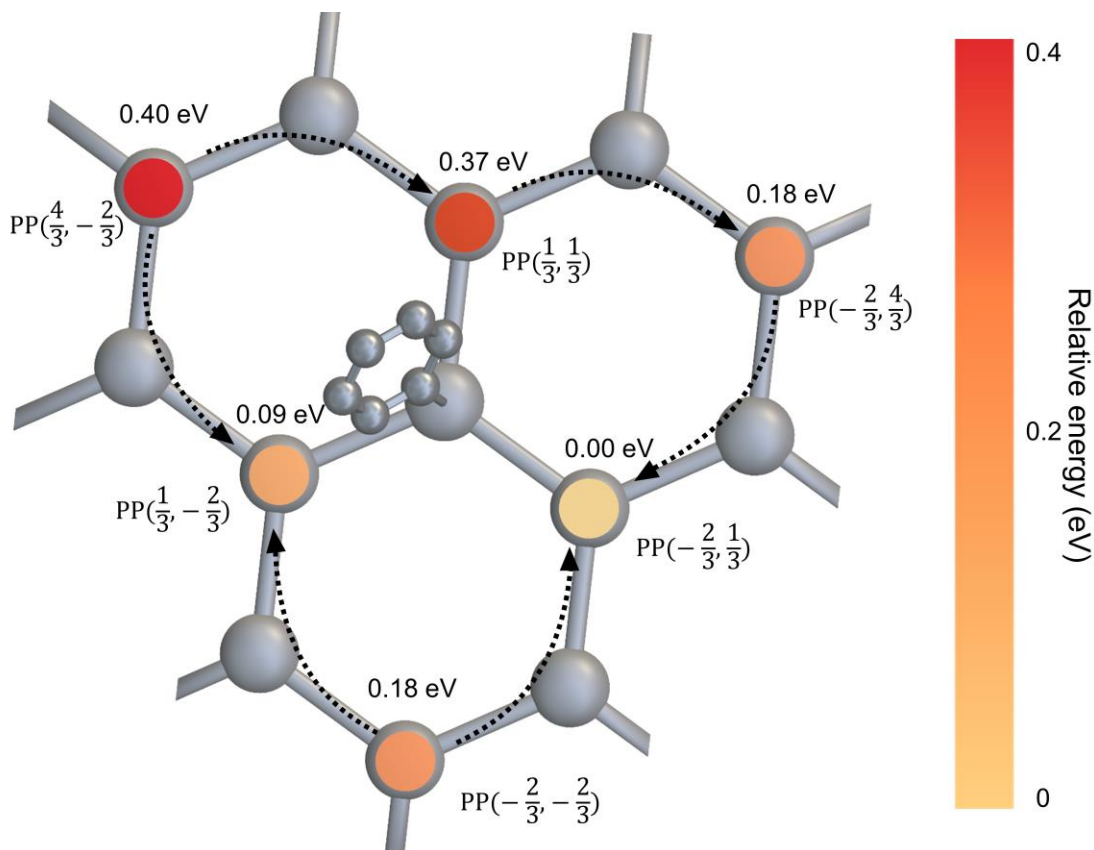
Figure 4-14. The relative energies of the different bonding configurations of an OCC composed of 3,4,5-trifluoroaryl and –H groups on a (6,5)-SWCNT. The 3,4,5-trifluoroaryl is attached to the center carbon (0,0) position. The –H pairing group was then bonded at three ortho ((PP(1/3, 1/3), PP(-2/3, 1/3), and PP(1/3, -2/3)) and three para positions (PP(4/3, -2/3), PP(-2/3, 4/3), and PP(-2/3, -2/3)). The possible reconfiguration routes are shown as dashed arrows. The colored circles represent the relative energy of each bonding configuration, located at the carbon that bonds to the –H group. The color, and the numbers labeled represent the relative system energy compared to the thermodynamically most stable bonding configuration, PP(-2/3, 1/3).
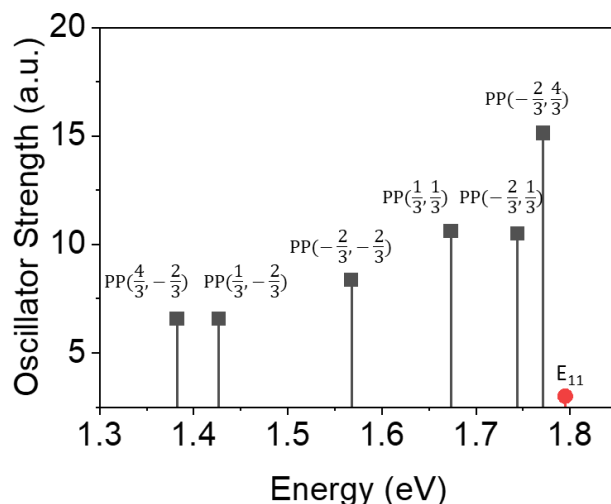
Figure 4-15. Optical transitions of OCCs simulated by TD-DFT. The simulated OCC peaks for different bonding configurations are shown, in which the aryl functional group is located at the center of the carbon lattice and the pairing -H group bond is located at the ortho configurations of the PP(1/3, 1/3), PP(1/3, -2/3), and PP(-2/3, 1/3) and para configurations of the PP(4/3, -2/3), PP(-2/3, -2/3), and PP(-2/3, 4/3) carbon atoms. E_{11} is simulated from a pristine (6,5)-SWCNT.

Table 4-1. Relative energies of the simulated bonding configurations.

Bonding Configuration	Relative System Energy (eV)*	OCC Emission Energy (eV)
PP(-2/3, 1/3)	0	1.744
PP(1/3, -2/3)	0.0906	1.427
PP(1/3, 1/3)	0.3688	1.673
PP(-2/3, 4/3)	0.1839	1.771
PP(- 2/3, -2/3)	0.1837	1.567
PP(4/3, -2/3)	0.3961	1.382

* Relative system energies are reported relative to the ortho PP(-2/3, 1/3) structure, which has the lowest energy.

To assign the experimentally observed OCC peak shifts, I correlated the system energy with the optical transition energy of each bonding configuration from DFT and TD-DFT, respectively, and identified possible routes of such rearrangement. In each OCC, the bond energy of C-H is weaker than that of the $C(sp^3)$-C(aryl) bond, and thus

I considered the transition of the OCC bonding configuration based on H migration on the sp^2 carbon lattice around the aryl group. The –H group was allowed to rearrange 2 carbons away each time, constituting the para to ortho transition and vice versa. Although the transition states between each bonding configuration were not simulated due to the high computational costs., the laser irradiation induced defect bond breakage and formation has been previously demonstrated with larger diameter SWCNTs.[176] Following this method, I consider the bonding reconfiguration occurring from higher energy configurations to lower energy ones until the lowest energy structure is reached (Figure 4-14). I then performed TD-DFT calculations and compared the difference in the emission energy between the initial and final OCC configurations to determine whether any of these values matched the experimentally observed spectral shifts.

With this approach, I identified eight thermodynamically favorable routes for bonding reconfiguration (Figure 4-14 and Table 4-2). Four of these eight routes, from higher energy structures including ortho PP(1/3, 1/3), para PP(-2/3, 4/3), para PP(-2/3, -2/3), and para PP(4/3, -2/3) to the lower energy configurations of ortho PP(-2/3, 1/3) and ortho PP(1/3, -2/3), reduce in system energy by 0.18–0.40 eV, which I used to find an assignment of the blueshifted OCC peaks. Specifically, the PP(1/3, 1/3) ortho configuration has previously been associated with the experimentally observed E_{11}^- emission at ~1150 nm (1.078 eV),[20, 161, 177] which I found to blueshift upon laser irradiation. Based on our calculations, the transformation most likely occurs following the energy descending ortho PP(1/3, 1/3) → para PP(-2/3, 4/3) → ortho PP(-2/3, 1/3) route. In contrast, para PP(-2/3, 4/3)→ ortho PP(-2/3, 1/3) would result in redshifted OCC emissions, which were not observed experimentally, suggesting para PP(-2/3,

4/3) OCCs are rarely formed during the OCC synthesis, which is consistent with a previous study by Tretiak, Doorn, and co-workers.[20] Para PP(-2/3, -2/3) can directly convert to ortho PP(-2/3, 1/3), also leading to a blueshift in its emission based on our calculations. Alternatively, para PP(-2/3, -2/3) can convert to ortho PP(1/3, -2/3), however, it would lead to a redshift in its emission based on TD-DFT calculations, which I did not observe experimentally.

Table 4-2. Proposed routes for bonding reconfigurations.

Route of bonding reconfiguration	Relative energy change* (eV)	Change in OCC emission
PP(1/3, 1/3) → PP(-2/3, 4/3) → PP(-2/3, 1/3)	-0.3788	Blueshift
PP(4/3, -2/3) → PP(1/3, 1/3) → PP(-2/3, 4/3) → PP(-2/3, 1/3)	-0.3961	Blueshift
PP(4/3, -2/3) → PP(1/3, -2/3)	-0.3055	Blueshift
PP(-2/3, -2/3) → PP(-2/3, 1/3)	-0.1837	Blueshift
PP(-2/3, -2/3) → PP(1/3, -2/3)	-0.0931	Redshift
PP(-2/3, 4/3) → PP(-2/3, 1/3)	-0.1839	Redshift
PP(-2/3, 1/3) → PP(-2/3, 1/3)	0	None
PP(1/3, -2/3) → PP(1/3, -2/3)	0	None

* Relative energy change = the relative system energy of the final bonding configuration – the relative system energy of the initial bonding configuration.

From our experiments, I also observed the intensity of E_{11}^{-*} emitting in the range of 1221–1330 nm (0.932–1.015 eV) reduced upon laser irradiation. I speculate that this E_{11}^{-*} peak is related to PP(1/3, -2/3), whose emission occurs at a longer wavelength compared to E_{11}^{-} (< 1.0 eV after correction according to previous study[178]) based on our TD-DFT calculation. Upon irradiation, this E_{11}^{-*} peak disappears, suggesting its associated bonding configuration is eliminated or rearranges to non-emissive structures, such as PP(4/3, -5/3) (shown in Figure 1-7) or even further to more than 3 carbon atoms away from the aryl site.[179] However, the non-emissive structure

PP(4/3, -5/3) has a much higher relative energy of ~1.58 eV compared to the para and other bonding configurations, making it inaccessible under our experimental conditions.

Taken together, our simulation and experimental observations suggest the bonding configurations synthesized before laser irradiation can be ortho configurations of PP(1/3, 1/3), PP(1/3, -2/3), and PP (-2/3, 1/3) and para configurations of PP(4/3, -2/3) and PP(-2/3, -2/3), with different thermodynamic stability. However, after laser irradiation, most of the kinetic configurations convert to the thermodynamically stable ortho PP(-2/3, 1/3) configuration, resulting in the observed single PL peak at a blueshifted wavelength.

4.3   Conclusions

The chemical synthesis of OCCs on the sp^2 carbon lattice of a SWCNT host creates many bonding configurations that result in a broad distribution of the quantum defect PL peaks. I show that resonant excitation of the nanotube host with light can convert the kinetic bonding structures to the thermodynamically stable configuration, leading to a single PL peak. I followed this structural reconfiguration on 3,4,5-trifluoroaryl OCC-tailored (6,5)-SWCNTs as a model system using *in situ* ensemble spectroscopy as well as single nanotube hyperspectral PL imaging. The results suggest the initially generated OCCs tend to form kinetically favorable though thermodynamically less stable bonding configurations during synthesis but can be removed or transformed into a more thermodynamically stable form by laser irradiation using a wavelength resonant with the E_{22} transition of the nanotube host. I also performed DFT simulations to reveal the possible pathways for the OCC conversion

from the kinetic structures to the thermodynamically stable one. This study provides a synthetic route to control the atomic configurations of OCCs on sp^2 carbon lattices, which may ultimately enable the synthesis of identical quantum light sources for quantum information science, molecular sensing, and bioimaging.

4.4 Supplementary Notes

4.4.1 *Supplementary Note 4-1. Estimate of the nanotube temperature on the polystyrene (PS)/Au/Si substrate under irradiation of 561 nm laser at a power density of 184 W/cm^2.*

The laser in our hyperspectral imaging system is shaped with a beam shaping module to homogeneously irradiate a wide field with a diameter of 0.153 mm on the sample surface.[175] For a surfactant encapsulated individual nanotube that is deposited on the polystyrene (PS)/Au/Si substrate and under irradiation of 561 nm laser at a power density of 184 W/cm^2, I can estimate the nanotube temperature by considering the time-dependent energy balance[11] between the laser energy absorbed by the nanotube and the heat transfer to the surroundings:

$$(\pi R^2 L)\rho C_p \frac{dT(t)}{dt} = q_{laser} 2RL\alpha_{561nm} - \frac{2RLk_{PS}(T(t) - T_{PS})}{H} - 2\pi RLh_{Air}(T(t) -$$

$$T_{Air}) - 2\pi RLG\big(T(t) - T_{surfactant}\big) \qquad (1)$$

where R is the radius of the SWCNT, L is the SWCNT length, H is the PS thickness of ~ 100 nm. ρ is the density of the nanotube with an average value of 1.8 g/cm^3,[180] C_p is the SWCNT specific heat with a value of ~670.98 J/(kg·K) for nanotubes with a diameter of 0.757 nm,[181] $T(t)$ is the temperature of the nanotube

depending on the irradiation time t, k_{PS} is the thermal conductivity of PS (0.04 W/(m·K)),[182] h_{Air} is the heat transfer coefficient between the nanotube surface and air with a value of ~7.5 × 10^4 W/ (m^2·K) for a nanotube with diameter of ~0.8 nm,[183] and $G = \sim 1.2 \times 10^7$ W m^{-2} K^{-1} is the interfacial thermal conductance between nanotube and surfactant.[184] T_{PS}, T_{Air} and $T_{surfactant}$ are the temperatures of PS, air and surfactant, which I assumed were around the room temperature of 298 K due to the utilization of a large sized bulk substrate (0.5 x 0.5 cm^2) compared to the size of an individual SWCNT as well as the gold layer beneath the PS layer, which serves as a good thermal conductor, thus the heat should not accumulate. q_{laser} is the power density of the laser (184 W/cm^2). $\alpha_{561nm} = \frac{I}{I_0} = e^{-\sigma ln}$ is the absorption of 561 nm light by the (6,5)-SWCNTs, where σ is the absorption cross section of (6,5)-SWCNTs at the excitation wavelength.[185] Finally, l and n are the unit length of the nanotube and number of carbon atoms per unit length, respectively.

Solving equation (1) gives the temperature change as follows:

$$\Delta T = \frac{2q_{laser}\alpha_{561nm}}{2\frac{k_{ps}}{H}+2\pi h_{air}+2\pi G} = 1\ K \tag{2}$$

Furthermore, I also estimated the temperature increase of the SWCNTs using another model describe in Wang et al.[174] as follows:

$$\Delta T(r,t) = \frac{Q}{4\pi K}\ln\left(\frac{2LGt}{\rho C_v r^2} - 0.5772\right) \tag{3}$$

where Q is the energy input from the laser, L, ρ and C_v are the length, the density and heat capacity, respectively, of the surrounding molecule, G is the interfacial thermal conductance for the surrounding surfactant molecule ($G = \sim 1.2 \times 10^7$ W m^{-2} K^{-1})[184] and t is time. By plugging in the constants, I obtained maximum ΔT values of

0.41 K. Both models suggest when (6,5)-SWCNTs are irradiated with 184 W/cm^2 561 nm light, the temperature at these nanotubes does not significantly increase.

4.4.2 *Supplementary Note 4-2. Water-filling-caused spectral heterogeneity in the OCC emission.*

The nanotubes were dispersed with 2 w/v% DOC aqueous solution, in which water molecules can spontaneously enter the interior of the SWCNTs as the nanotube ends are typically opened during solution processing.[49, 50] For the hyperspectral imaging measurements, I deposited the OCC-(6,5)-SWCNTs on a dry substrate. As a result, some of the water within the nanotubes may partially evaporate, causing the observed differences in the E_{11} values from nanotube to nanotube (ranging from 992 to 973 nm (1.250–1.275 eV)). In contrast, the exterior environment is dominated by the DOC surfactant. As the OCC emission mechanism is enabled by the creation of a local potential well upon covalent modification of the nanotube[69] (*i.e.*, the OCC E_{11}^- or E_{11}^{-*} emission energy is approximately the E_{11} energy subtracted by the depth of the potential well), the change in the E_{11} energy will also affect the OCC E_{11}^- or E_{11}^{-*} emission energy. However, the endohedral environment of each SWCNT does not change upon irradiation as the E_{11} peak of each OCC-(6,5)-SWCNT remained unchanged (Figure 4-3 and Figure 4-8).

4.5 Materials and Methods

4.5.1 Synthesis of OCCs.

I synthesized 3,4,5-trifluorobenzenediazonium tetrafluoroborate and 4-nitrobenzenediazonium tetrafluoroborate from 3,4,5-trifluoroanaline and 4-nitroaniline, respectively (Sigma Aldrich) as previously described.[59] In brief, 3.0 mL of Nanopure[TM] water and 2.6 mL of tetrafluoroboric acid solution (48 wt.% in water, Sigma Aldrich) were added to a round bottom flask (RBF) which was then cooled in an ice bath. To the cooled RBF was added 4.8 mmol of aniline. I then dissolved 9.71 mmol of sodium nitrite (Sigma Aldrich, ≥97.0%) in 2 mL of Nanopure[TM] water, which was added dropwise to the RBF with stirring. The precipitated tetrafluoroborate salt was washed with 200 mL of diethyl ether under vacuum filtration for ~20 minutes while being protected from light.

I synthesized the OCCs on semiconducting SWCNTs based on a method described in our previous work.[65] In brief, 0.020 mg of raw SWCNTs (CoMoCat SG65i) were dissolved in 1 mL of chlorosulfonic acid (Sigma Aldrich, 99%) followed by the addition of ~100 μL of 3,4,5-trifluorobenzenediazonium tetrafluoroborate (~4 mg/mL) in chlorosulfonic acid. In the case of 4-nitrobenzenediazonium tetrafluoroborate, a low [diazonium salt]:[C] ratio of ~1:2000 was used to minimize potential branching reactions on the OCC benzene ring. The SWCNT/acid mixture was then added drop-by-drop to Nanopure[TM] water while stirring vigorously using a Teflon-coated magnetic stir bar. (Safety Note: This reaction process aggressively generates heat and acidic smog. The experiment should be performed in a fume hood with proper

personal protective equipment, including goggles/facial mask, lab coat, and acid-resistant gloves.) The resulting SWCNTs subsequently precipitated out of the solution and were collected on a polyvinylidene fluoride membrane (MilliporeSigma VVLP membrane, 0.1 μm pore size) and then rinsed with ~50 mL of Nanopure™ water. The product was a powder of OCC-SWCNTs, which was then dried in a vacuum oven at room temperature overnight.

4.5.2   Individual dispersion of long OCC-SWCNTs.

The dry OCC-SWCNT powder was dispersed in a 2% (w/v) DOC (Sigma Aldrich, > 97%) aqueous solution by superacid-surfactant exchange.[65, 146] Briefly, the OCC-SWCNT dry power was dissolved in chlorosulfonic acid to obtain a 0.02 mg/mL solution. I then added ~2 mL of the OCC-SWCNT/chlorosulfonic acid solution drop-by-drop into 320 mL of NaOH (0.75 M) containing ~0.08% (w/v) DOC aqueous solution with vigorous stirring until a pH of ~8 was reached to obtain a black or gray solution of SWCNTs. The solution was stirred for at least another 30 min followed by the addition of several drops of concentrated HCl to protonate the DOC surfactant molecules, which coalesce into a gray precipitate along with the wrapped SWCNTs. The precipitate was filtered with a polyvinylidene fluoride filtration membrane (MilliporeSigma SVLP membrane 5 μm pore size). Then ~12.8 mL of Nanopure ™ water and several drops of 1 M NaOH were added to the precipitate and the solution pH was tuned to ~7–8. The mixture was further stirred for at least 1 day followed by centrifugation at ~25000 g for 90 min (Eppendorf centrifuge 5417R) to remove any undissolved SWCNT bundles. The average length of these nanotubes as described[146] is ~ 1.3 μm.

4.5.3 Purification of OCC-tailored (6,5)-SWCNTs.

I adapted the aqueous two-phase extraction (ATPE) method[52, 53] with some modifications to generate a chirality-sorted solution of OCC-(6,5)-SWCNTs. In detail, I first mixed 1 mL of the OCC-SWCNT aqueous solution dispersed by 2% (w/v) DOC (obtained after the superacid-surfactant exchange) with 0.3 mL of 50% (w/w) polyethylene glycol (PEG) (M.W. 6000 Da, Alfa Aesar) aqueous solution and 0.3 mL of 20% (w/w) dextran (M.W. 70000 Da, TCI) aqueous solution using a vortex mixer, followed by centrifugation (Eppendorf centrifuge 5810R) at 4000 g for 1 min to induce phase separation, in which the OCC-SWCNTs preferentially stay at the bottom phase (dextran rich). The DOC surfactants were then gradually exchanged to 0.9% (w/w) sodium cholate and 0.7% (w/w) sodium dodecyl sulfate (SDS) according to a published procedure.[53] Then ~20 µL of 1 M NaSCN (99%, Sigma Aldrich) solution was added as the phase modifier to induce metallic/semiconducting OCC-SWCNT sorting. After centrifuging the solution at 4000 g for 1 min, the OCC-(6,5)-SWCNTs preferentially stay at the top PEG-rich phase. The OCC-(6,5)-SWCNT solution was then pipetted out followed by centrifugal ultrafiltration (Amicon Ultra-15, 100 kDa) to remove the PEG polymers and residual diazonium salts. ~13 mL of 2% (w/v) DOC in H_2O was used to rinse the OCC-(6,5)-SWCNT solution 5 times during the ultrafiltration, resulting in the OCC-(6,5)-SWCNTs dispersed in 2% (w/v) DOC/H_2O.

4.5.4 Ensemble Spectroscopy Characterization.

The ensemble PL spectra were collected with a NanoLog spectrofluorometer (Horiba Jobin Yvon). The samples were excited with a 450 W Xenon source dispersed

by a double-grating monochromator. The power density of the 565 nm light was ~10 mW/cm^2. The slit width of the excitation and emission beams were 10 and 20 nm, respectively. A 400 nm longpass filter (FGL400S, Thorlabs) was installed in the excitation pathway to remove the potential UV light. The PL spectra were collected using a liquid-N$_2$ cooled linear InGaAs array detector. The emission spectra were collected with excitation light at the E$_{22}$ wavelength (565 nm for (6,5)-SWCNTs). The integration time to collect each spectrum was set to 0.01 s to minimize any change in the OCCs by light irradiation. Thus, during the collection of the PL spectra, the SWCNT samples were at most excited for 0.02 s. Each spectrum was taken *in situ* immediately after irradiating the nanotube solution with 565 nm light from the spectrofluorometer for 5 s, which added up to a total of 265 s. Note that all samples had an optical density (OD) of less than 0.5 at the (6,5) E$_{11}$ band, measured using a PerkinElmer Lambda 1050 spectrophotometer with a broadband InGaAs detector.

4.5.5   *Hyperspectral imaging.*

To collect single nanotube PL images, 5 μL of the OCC-(6,5)-SWCNTs in 2% w/v DOC/D$_2$O solution was spin-coated at 3000 RPM for 1 min onto a ~150-nm thick polystyrene layer on top of a ~50 nm-thick Au layer on a Si substrate. The polystyrene layer acted as an insulating layer to prevent the SWCNTs from contacting with the Au, which would quench the PL. The Au layer was added as a mirror to double the excitation and emission light. The hyperspectral imaging was performed on a custom-built microscope.[40] I used an infrared optimized 100x objective (LCPLN100XIR, numerical aperture = 0.85, Olympus) along with a continuous wave laser at 730 nm (Shanghai Dream Lasers Technology Co., Ltd., power density of 42 W/cm^2) as the

excitation light source for obtaining the PL spectra, as well as a 561 nm laser (JiveTM Cobolt AB, Sweden, power density of 341.79 W/cm^2) with a neutral density filter (Edmund Optics, OD 0.3, OD 0.9, OD 2.5 and OD 4.0.) to adjust the power density for irradiating the SWCNTs. The excitation power density at the sample was measured with an optical power meter (Newport 1916-C) and silicon detector (Newport 918-SLOD3). I note that the power density reported here does not consider the mirror effect of the Au layer, which may double the power density. Fluorescent emission from the sample was filtered through a longpass dichroic mirror (875 nm edge, Semrock, USA) to remove the elastic laser scattering and then dispersed by a volume Bragg grating (Photon Etc, Inc. Montreal, Canada). Only the diffracted light with a narrow bandwidth of 3.7 nm was collected on the detector to form a spectral image. The PL spectra were fitted by Voigt profiles. Note the PL images of the OCC emissions in Figure 3a are taken with a 1100 nm longpass filter (FELH1100, Thorlabs).

4.5.6 DFT and TD-DFT Calculations.

All DFT calculations were performed with Gaussian 09 software.[186] I built OCC models by implanting a pair of groups (3,4,5-trifluoroaryl and hydrogen) in the center of a 12 nm (6,5)-SWCNT in 3 ortho and 3 para positions, as shown in Figure 7. The geometries of all structures were optimized using the Coulomb-attenuated B3LYP (CAM-B3LYP) functional[187] and 3-21G basis set.[188] This methodology has been successfully implemented previously by Gifford et al. to calculate optical transitions of functionalized SWCNTs.[72] The optical transitions were computed using TD-DFT with the same functional and basis set as in DFT. We analyzed the natural transition orbitals (NTOs)[189] with Gaussian 09 software and confirmed that the NTOs were strongly

localized at the OCC, further verifying the defect origin of the optical transitions (Figure 4-16). I note the simulated peaks are higher in energy compared to the experimental data due to the vacuum environment used in the simulation and finite length of the SWCNTs. However, we did not correct the simulated peaks against experimental spectral data as proposed by Tretiak and co-workers[178] since this correction is a qualitative adjustment and does not change the relative emission energy ordering of the OCCs with different bonding configurations.
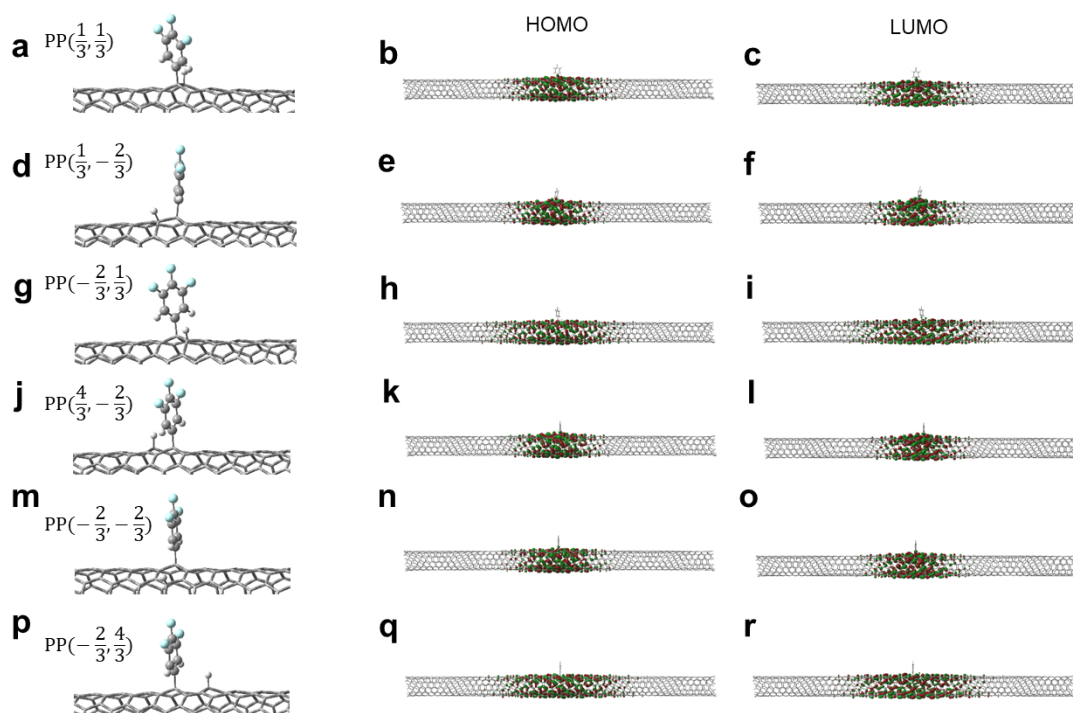
Figure 4-16. Natural transition orbitals of OCCs with different bonding configurations. (a) Zoomed-in molecular model, (b) HOMO, and (c) LUMO of PP(1/3, 1/3). (d) Zoomed-in molecular model, (e) HOMO, and (f) LUMO of PP(1/3, -2/3). (g) Zoomed-in molecular model, (h) HOMO, and (i) LUMO of PP(-2/3, 1/3). (j) Zoomed-in molecular model, (k) HOMO, and (l) LUMO of PP(4/3, -2/3). (m) Zoomed-in molecular model, (n) HOMO, and (o) LUMO of PP(-2/3, -2/3). (p) Zoomed-in molecular model, (q) HOMO, and (r) LUMO of PP(-2/3, 4/3). Note that only the NTO pairs that dominantly contribute to the transition ($> 60\%$) are included in the plots.

5   Thermally-Controlled [2+2] Cycloaddition Produces

Divalent Organic Color-Centers in Single-Walled Carbon

Nanotubes with Fewer Atomic Configurations

This chapter is adapted from the following published manuscript: Qu, H.; Wu, X.;

Fortner, J.; Wang, Y.

Y.H.W., and H.Q., conceived and directed the research. H.Q., and X.W., performed the experiments, H.Q., and J.F. performed DFT simulations. All authors contributed to data analysis. H.Q. and Y.H.W. wrote the manuscript with inputs from all co-authors.

5.1   Introduction

OCCs are molecularly tunable functional groups[58, 59, 64, 158] covalently attached to the sidewalls of semiconducting SWCNTs that produce new optically-allowed states (E_{11}^- and E_{11}^{-*}) redshifted from the SWCNT band-edge emission (E_{11}) in the near infrared.[59, 65] These OCC emissions display a number of intriguing properties,[55] such as the ability to trap diffusive excitons,[190, 191] higher quantum yields compared to the E_{11} state, [59, 192 22, 54] and the emission of single photons at room temperature.[19, 21, 159] The synthesis of OCCs using current monovalent-based chemistries (e.g., diazonium chemistry,[59] diazoether chemistry,[63] reductive alkylation,[58] and photoactivated radical addition[64]) can generate up to six different bonding configurations (Figure 5-1a).that result in heterogeneous emissions,[20, 193] because the addition of these moieties to the SWCNT double bond yields an unpaired electron that typically bonds with a H or OH group available in solution to close the valence state [67] For example, OCCs synthesized by the commonly used diazonium chemistry show multiple, convoluted OCC emission

115

peaks that span from ~1100 nm to ~1400 nm for (6,5)-SWCNTs. Furthermore, the rotation of the functional groups around the single bond connecting to the nanotube may broaden the emission linewidth. As a result, the spectral inhomogeneity of current OCCs limit their use in applications that require uniform emission, such as chemical sensing,[16] single photon sources for quantum information,[194] and bioimaging.[195, 196]

One possible solution to the problems created by the multiple bonding configurations of monovalent OCCs is the use of divalent functional groups, in which two bonds are created during covalent functionalization of the nanotube. However, current syntheses of divalent OCCs (e.g., functionalized by 1,2-diiodobenezene) produce multiple OCCs emission from a mixture of both monovalent and divalent functional groups[58, 64] as the reactive sites on aryl OCC produced step-wisely by the two iodine and the steric hinderance obstruct the second bond formation.

An alternative to divalent reactions is cycloaddition. The two bonds are created simultaneously reducing the possibility of forming a monovalent OCC. In this chemistry, the divalent functional group provides its own pairing bond, which helps decrease the structural heterogeneity caused by the bonding of H or OH. For example, the Diels-Alder reaction, which is activated by light or heat and typically features [4+2] cycloaddition between a diene and dienophile.[197-200] However, this cycloaddition reaction can also proceed via a [2+2] pathway, which Star et al. shows that the light activated cycloaddition preferentially occur on SWCNTs compared to the less stable [4+2] products.[201] A [2+2] cycloaddition reaction on SWCNTs would reduce the number of possible OCC bonding configurations to just 3, as shown in Figure 5-1b. Furthermore, the rotational constraint of such divalent OCCs compared to monovalent

counterparts may further reduce the emission linewidth.[72] An added advantage is the fact that this cycloaddition reaction does not require a catalyst, nor does it generate byproducts[197] that can affect the nanotube emission properties.

In this study, I demonstrate the synthesis of divalent OCCs on (6,5)-SWCNTs via [2+2] cycloaddition using enophiles such as methylmaleimide (N-MMI), maleic anhydride (MA), and 4-cyclopentene-1,3-dione (CPD) (Figure 5-1b). I observed three distinct OCC PL peaks centered at 1112 nm (1.115 $\pm$ 0.008 eV), 1139 nm (1.089 $\pm$ 0.006 eV), and 1213 nm (1.022 $\pm$ 0.012 eV), whose predominance can be controlled by the reaction temperature. I found at lower temperature (80 ^{o}C), the ~1139 nm peak was favorably synthesized, while at 120 ^{o}C, the 1112 nm peak became dominating. These three OCC emissions are in good agreement with DFT calculations on the three defect structures possible with [2+2] cycloadditions. This scalable synthesis and our improved understanding of divalent bonding on SWCNTs could help facilitate the application of OCCs where narrow, uniform emission is required.
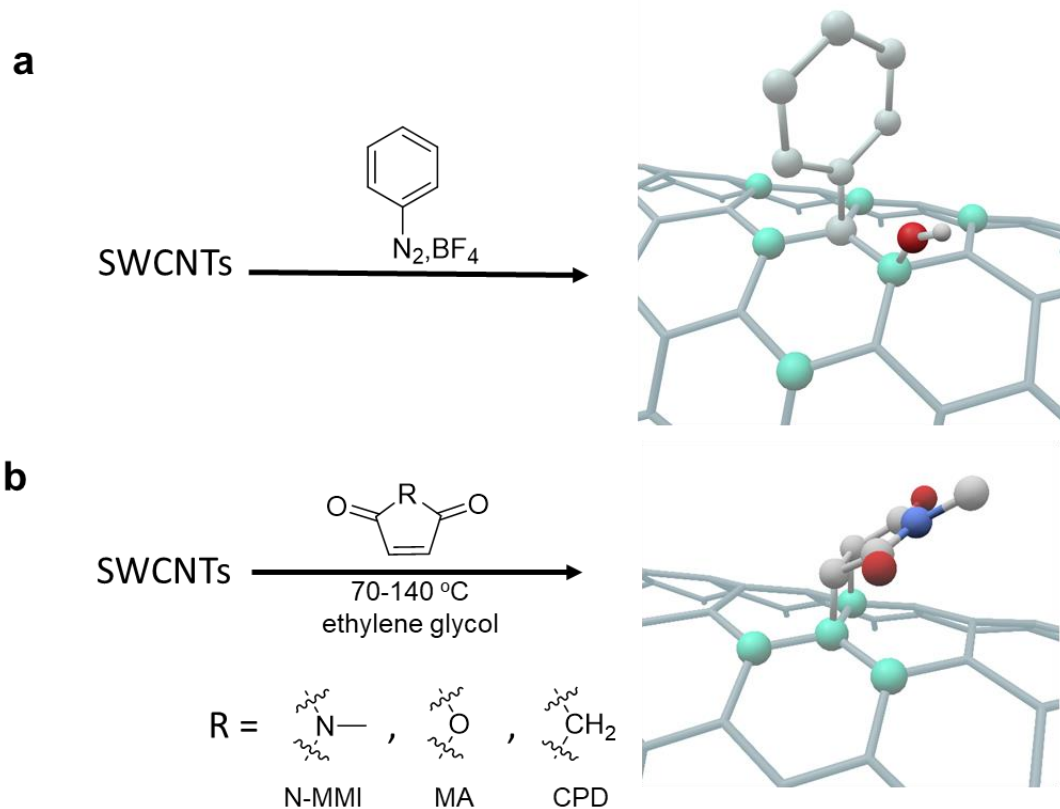
Figure 5-1. Schematic comparing monovalent vs. [2+2] cycloaddition divalent OCCs and the resulting bonding configurations. a, Monovalent chemistry using diazonium salt to functionalize SWCNTs. When SWCNTs are functionalized with diazonium salt, it generates 6 possible bonding configurations (shown in cyan atoms on the right).. The six possible bonding configurations of OCCs generated via an addition reaction on the sp2 carbon lattice. The gray atom at the center shows the first functional group attachment site, while the pairing group may add to the other 6 atoms shown in cyan. b, Divalent chemistry via [2+2] cycloaddition to functionalize SWCNT with. When SWCNTs are functionalized with enophile molecules, including N-MMI, MA, or CPD in ethylene glycol at elevated temperature, it can generate 3 possible bonding configurations (shown in cyan atoms on the right).

5.2   Results and Discussions

To synthesize the divalent OCCs via [2+2] cycloaddition, I used CoMoCat SG65i SWCNTs, which primarily consist of the (6,5) nanotube chirality, along with minor (8,3) and (7,5) components and a limited amount of larger diameter nanotubes, such as (7,6) and (8,4). Figure 5-2a shows a two-dimensional (2D) PL excitation-

118

emission map of the SG65i starting material, in which the E_{11} emissions of the different chiralities can be identified. To conduct the [2+2] cycloaddition reaction, 1–5 mg of this SWCNT powder was added to ethylene glycol, which is a highly viscous "solvent" that can kinetically suspend the SWCNTs by the shearing force created from a stir bar, in which the resulting suspension remains stable for ~2 days. I added 2–15 mg of the enophile molecules, such as N-MMI, MA, or CPD, to this SWCNT suspension under stirring, and then heated the mixture at different temperatures, ranging from 70 $^{\circ}$C to 140 $^{\circ}$C, to activate the reaction overnight. The resulting OCC-functionalized SWCNTs (OCC-SWCNTs) were then subsequently dispersed in 1 wt/v % sodium deoxycholate (DOC)/D_2O solution for further characterization (see Methods for details).

After the reaction, I measured the 2D excitation-emission map of the samples to determine whether OCCs were successfully added to the nanotubes. Figure 5-2b shows the ensemble PL results of the SWCNTs reacted with N-MMI (N-MMI-SWCNTs) at 100 $^{\circ}$C. Compared to the pristine starting material, the reacted SWCNTs show multiple OCC emissions convoluted at > 1100 nm.[193] In contrast, when I conducted the same reaction at 100 $^{\circ}$C but without the addition of N-MMI, I observed the same E_{11} SWCNT emission (Figure 5-2c) as the pristine nanotubes (Figure 5-2a). The PL emission spectra of the pristine SWCNTs, N-MMI-SWCNTs, and SWCNTs without the addition of N-MMI are shown in Figure 5-2d using 565 nm excitation, which is the E_{22} band of (6,5)-SWCNTs. I found a bright OCC emission generated peak at ~1130 nm (1.097 eV) with a shoulder band extending to 1400 nm (0.886 eV) for the SWCNTs reacted with N-MMI at 100 $^{\circ}$C. Similarly, several convoluted OCC emissions from the (8,3) and (7,5) chiralities can be observed with excitation of ~650–

670 nm (Figure 5-2b). In contrast, the control group (no N-MMI added) shows no significant increase in PL intensity in the range of > 1100 nm, though its E_{11} emission shows a marginal blueshift of ~1–2 nm compared to the pristine nanotubes. I also measured the 2D PL maps and emission spectra (565 nm excitation) for SWCNTs reacted with MA and CPD at 100 $^{\circ}$C (Figure 5-3). Similar to N-MMI, new OCC-induced emission was observed for both samples in the range of 1100–1300 nm.

I measured the Raman spectra of the reacted samples to further confirm the covalent functionalization of the SWCNTs rather than surface adsorption. The conversion of sp^2 hybridized carbon atoms into sp^3 results in the increase of the Raman D-band—a common measure of covalent functionalization in carbon nanotube chemistry.[38] Figure 5-2e shows the Raman spectra of the pristine SWCNTs and N-MMI-SWCNTs. After the reaction, the D/G ratio, which represents the number of defects, increased from 0.07 to 0.31. These results demonstrate the OCCs are covalently functionalized on the SWCNTs, which generates the optically allowed OCC emission in the observed redshifted range.[65, 175, 193]
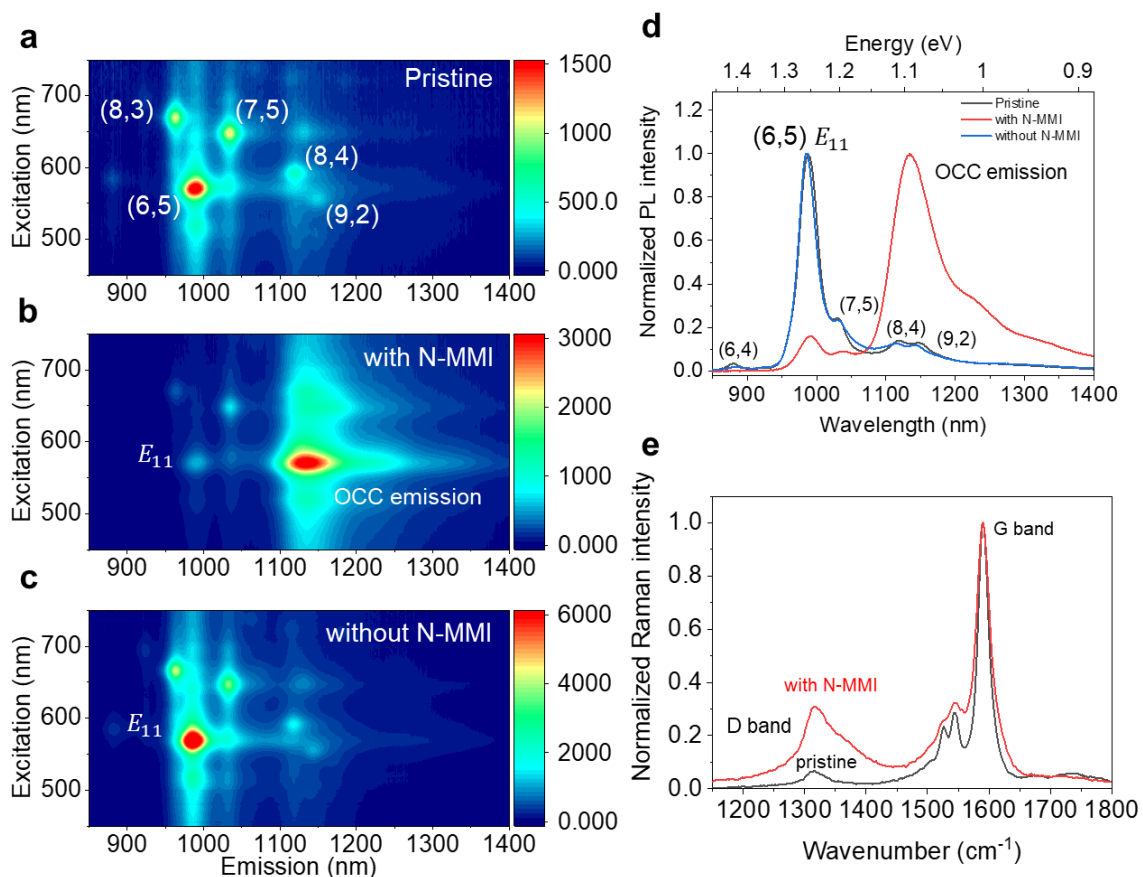
Figure 5-2. OCC generation on SWCNTs via cycloaddition using N-MMI. a, PL excitation map of the pristine SWCNT starting material, which primarily features the (6, 5) nanotube chirality, but also includes a mixture of other chiralities, including (8, 3), (7, 5), (8, 4), and (9, 2). b, PL excitation map of the nanotubes from (a) after reacting with N-MMI at 100 °C, showing OCC emission at wavelengths in the range of 1100–1300 nm. c, PL excitation map of the SWCNTs from (a) treated under the same conditions as in (b) at 100 °C, but without the addition of N-MMI. d, PL spectra of the pristine (6,5)-SWCNT starting material (black), after reaction with N-MMI (red), and after treatment to the same reaction conditions but without the addition of N-MMI (blue). The SWCNTs are excited at their E_{22} transition (565 nm). All the PL spectra were measured after dispersing the samples in 1 wt% DOC/D$_2$O. Note the small peaks in the starting material and control group emitting at ~880 nm, ~1030 nm, ~1118 nm, and ~1148 nm are the E_{11} emissions from pristine (6,4), (7,5), (8,4) and (9,2)-SWCNTs, respectively. e, Raman spectra of SWCNTs reacted with N-MMI (red) and the pristine SWCNT starting material (black). Note the PL spectra are normalized to the maximum peak intensity, and the Raman spectra are normalized to the G-band at ~1580 cm^{-1}.
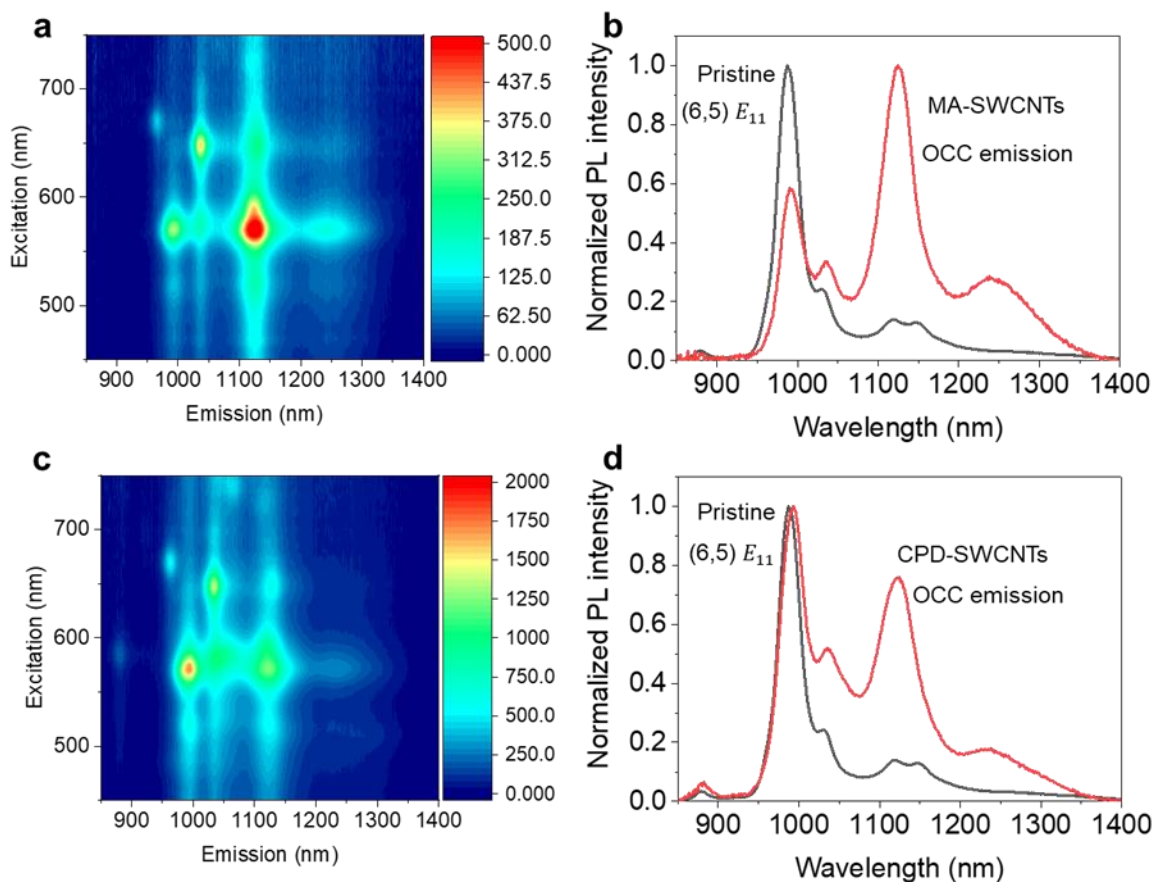
Figure 5-3. OCC generation with MA and CPD. a, PL excitation-emission map of SWCNTs reacted with MA. b, PL spectra of the pristine (black) and MA-SWCNTs excited at 565 nm. c, PL excitation-emission map of SWCNTs reacted with CPD. d, PL spectra of the pristine (black) and CPD-SWCNTs excited at 565 nm. Note the PL spectra are normalized to the maximum intensity.

To further investigate the convoluted emission of the N-MMI-SWCNTs prepared at 100 °C (1100–1300 nm, Figure 5-2b), I utilized hyperspectral PL microscopy to directly observed the PL of individual nanotubes. This method allows us to circumvent averaging effects in the ensemble PL to observe what individual emission may be occurring. To prepare the sample, I dispersed the nanotubes in 1 wt% DOC aqueous solution, which I deposited on a polystyrene (PS)-coated Au on Si substrate (see Methods). Note, ultrasonication was used during the dispersion step, which cuts the SWCNTs short, beyond the diffraction limit.[202] Therefore, the individual

nanotube PL appears as white spots rather than rod-like, as shown in Figure 5-4a. In addition to the tip sonication and centrifugation to individualize and remove nanotube bundles, the sample was diluted 1000-fold prior to deposition to ensure the SWCNTs were well-separated and individualized.

Unlike the ensemble PL, which featured convoluted OCC emission, the hyperspectral imaging statistically revealed 32 individual N-MMI-SWCNTs feature three distinct OCC peaks that appear at 1.089 ± 0.006 eV (~1139 nm; Figure 5-4b), 1.022 ± 0.012 eV (1225 nm; Figure 5-4c), and ~1.115 ± 0.008 eV (~1112 nm; Figure 5-4d). I denote these peaks as E_{11}^-, E_{11}^{-*}, and $E_{11}^{\sim}$, respectively (Table 5-1), all of which feature a similar full-width at half maximum (FWHM) of 0.032 ± 0.008 eV, 0.033 ± 0.007 eV, and 0.038 ± 0.010 eV. While some nanotubes displayed only one of these peaks, I also observed convoluted, multi-peak OCC emission from individual nanotubes (Figure 5-5). I also observed similar OCC emission for (8,3) and (7,5)-SWCNTs functionalized by the same cycloaddition reaction using N-MMI (Figure S4). These results suggest the three observed OCC emission peaks may be related to the three different possible bonding configurations of the [2+2] cycloaddition product, which is greatly reduced by 50% compared to the six distinct emission peaks from the six bonding configurations created by monovalent diazonium chemistry. [15, 29] Additionally, I hypothesize that more than one OCC of different bonding configuration can be present on the same SWCNT, which would explain the multi-peak emission observed from some of the individual nanotubes.

Table 5-1. PL peak energy and spectral shift (ΔE) of the N-MMI-(6,5)-SWCNTs based on single particle and ensemble measurements.

	Individual (6,5)-SWCNTs (eV)	ΔE (eV)*	Ensemble PL (eV)	ΔE (eV)*
$E_{11}^{\sim}$	1.115 ± 0.008	0.135 ± 0.007	1.121	0.132
E_{11}^{-}	1.089 ± 0.006	0.162 ± 0.010	1.102	0.151
E_{11}^{-*}	1.022 ± 0.012	0.228 ± 0.010	1.002	0.248

*$\Delta E = E_{OCCs\ emission} - E_{11}$.
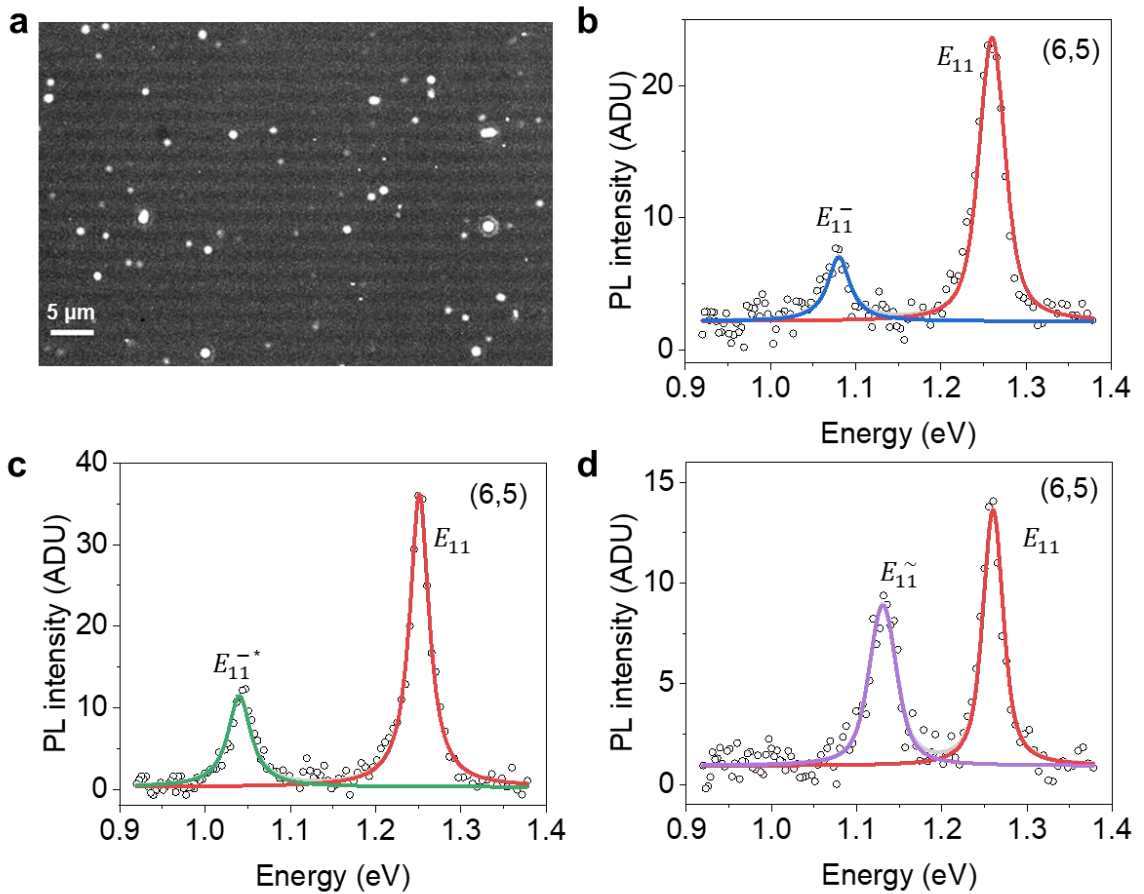
Figure 5-4. Hyperspectral PL imaging of individual N-MMI-(6,5)-SWCNTs. a, Hyperspectral image of N-MMI-SWCNTs. b-d, PL spectra of individual N-MMI-(6,5)-SWCNTs with different OCC emissions of (b) E_{11}^{-}, (c) E_{11}^{-*}, and (d) $E_{11}^{\sim}$.
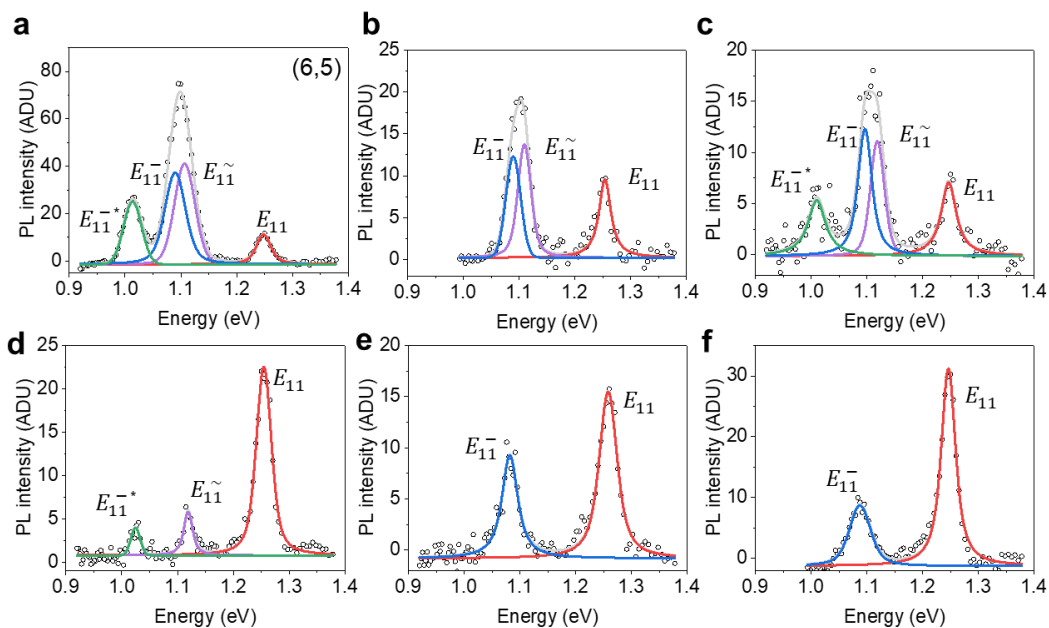
Figure 5-5. PL spectra of individual N-MMI-(6,5)-SWCNTs. a-c, PL spectra of individual (6,5)-SWCNTs d-f, PL spectra of individual (6,5)-SWCNTs The OCC emissions are color-coded: E_{11} (red), $E_{11}^{\sim}$ (purple), E_{11}^{-} (blue), and E_{11}^{-*} (green).

To further explore whether these 3 different OCC peak emissions may correspond to different bonding configurations of the [2+2] cycloaddition reaction, I aimed to thermodynamically control the reaction products using temperature. First, I functionalized SWCNTs at different temperatures ranging from 80–120 °C at a [N-MMI]: [C] ratio of 7:1 and measured the ensemble PL spectra (Figure 5-6) as well as the 2D PL maps (Figure 5-7). As the SWCNT samples were prepared and sonicated under aqueous conditions, there is some peak position variation that can be attributed to different degrees of water filling inside the nanotubes.[34] Therefore, a more accurate way to compare the relative energy of each bonding configuration is through the relative energy difference between the E_{11} peak and the OCC emission ($\Delta E = \Delta E = E_{OCC\ emission} - E_{11}$; Table 5-1), which corresponds to the OCC trapping depth.[69] Thus, when dealing with ensemble PL in the following sections, I deconvolute the mixed

OCC emissions based on ΔE rather than solely using the emission energies themselves. At the reaction temperature of 80 oC, the resulting OCC emission primarily features E11- at ~1130 nm (~1.097 eV) (Figure 5-6, Figure 5-7a). As I increase the temperature $\geq$ 90 oC, E_{11}^{-*} and $E_{11}^{\sim}$ begin to dominate the spectra. Specifically, at 120 oC, the OCC emission switches to $E_{11}^{\sim}$ at ~1111 nm (~1116 eV) along with E_{11}^{-*} at ~1228 nm (1.010 eV) (Figure 5-6, Figure 5-7d). Similarly, I investigated the temperature-dependence of OCC implantation using MA ([MA]:[C] = 20:1) at reaction temperatures of 70 ^{o}C to 140 ^{o}C (Figure 5-8). The lower reaction temperature (70–90 oC) favors E_{11}^{-}, while higher temperature (110–140 ^{o}C) favors the formation of $E_{11}^{\sim}$. E11-* is also synthesized at a medium temperature in this range, such as 90-110 ^{o}C. However, at a higher temperature of 140 ^{o}C, E_{11}^{-*} is less favorable and the main emission is $E_{11}^{\sim}$. These results suggest the formation of E_{11}^{-} is kinetically favored with a smaller activation energy compared to the other two OCC emissions and the formation of the $E_{11}^{\sim}$ and E_{11}^{-*} requires high activation energy (Figure 5-9). Furthermore, the activation energy for synthesis of $E_{11}^{\sim}$ and E_{11}^{-*} should be similar. But $E_{11}^{\sim}$ is more thermodynamically stable, which is favorable synthesized at high temperature compared to E_{11}^{-*}. Thus, the $E_{11}^{\sim}$ emission is likely to be from the most thermodynamically stable product compared to E_{11}^{-} and E_{11}^{-*}.
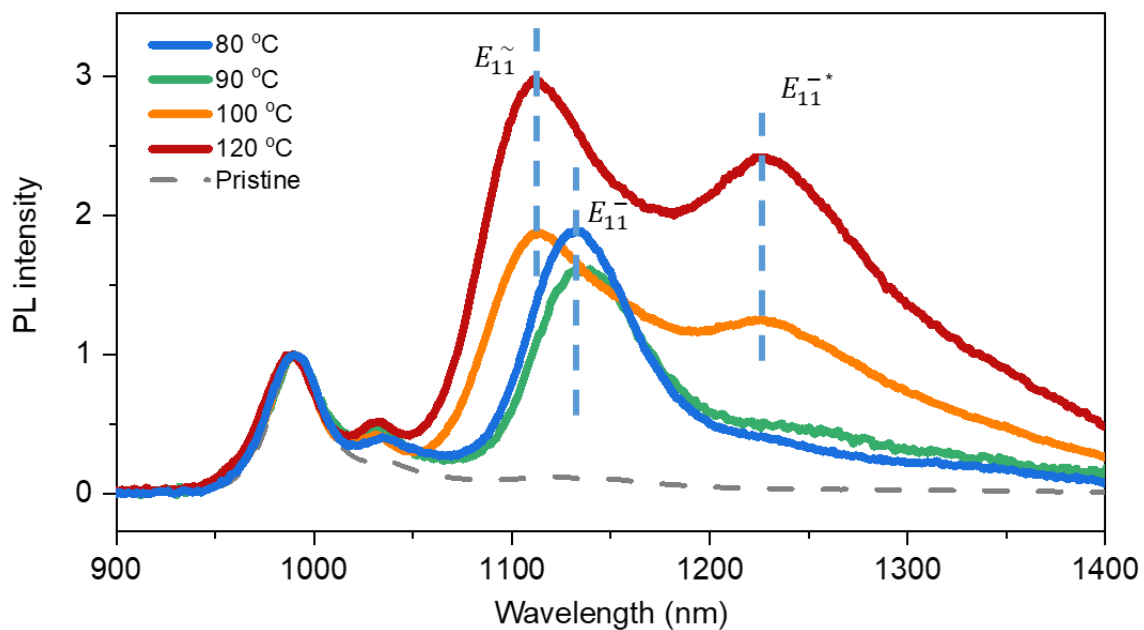
Figure 5-6. Temperature-dependent OCC emission from the reaction of (6,5)-SWCNTs with N-MMI at [N-MMI]:[C] = 7:1. PL spectra of (6,5)-SWCNTs reacted at 80 °C (blue), 90 °C (green), 110 °C (orange), and 120 °C (red). The PL spectrum of the pristine SWCNTs is shown by the dashed gray line. The PL spectra are normalized to the E_{11} emission of (6,5)-SWCNTs.
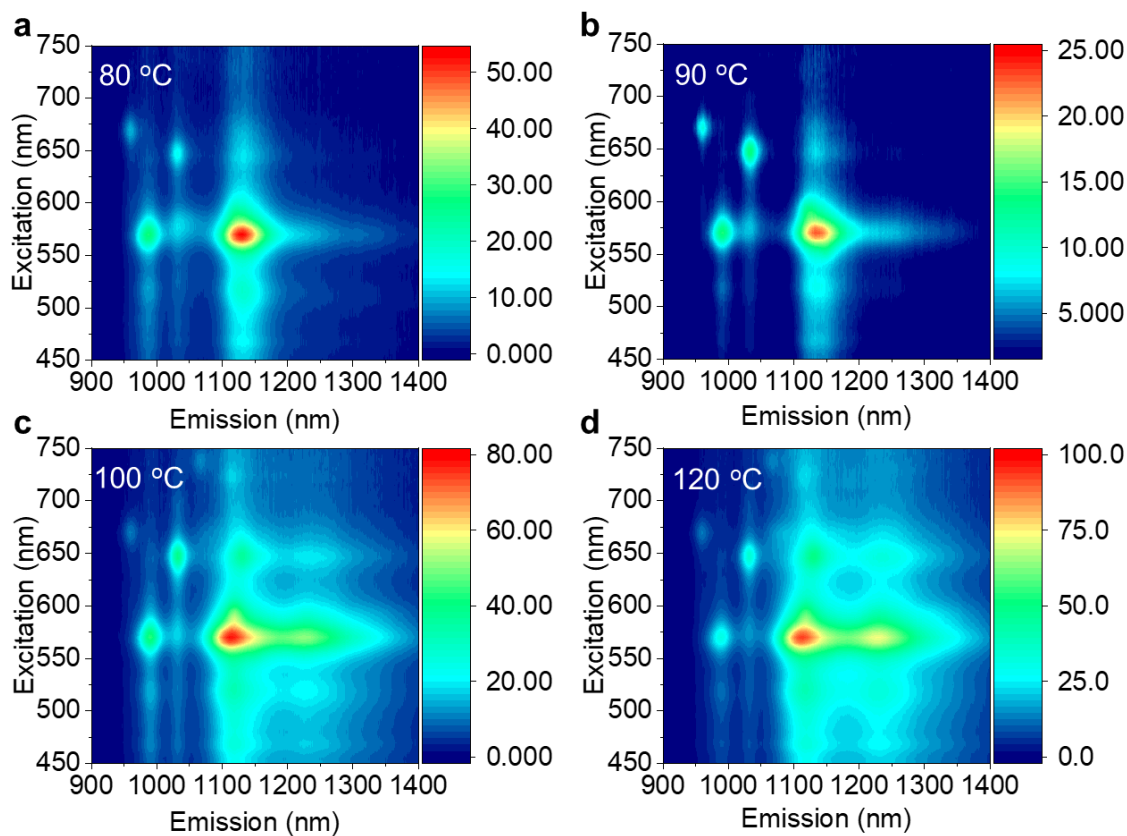
Figure 5-7. Temperature-dependent OCC emission from the reaction of (6,5)-SWCNTs with N-MMI. a-d, PL excitation-emission maps of SWCNTs reacted with [N-MMI] at [N-MMI]:[C] = 7:1 at 80 ºC (a), 90 ºC (b), 100 ºC (c), and 120 ºC (d).
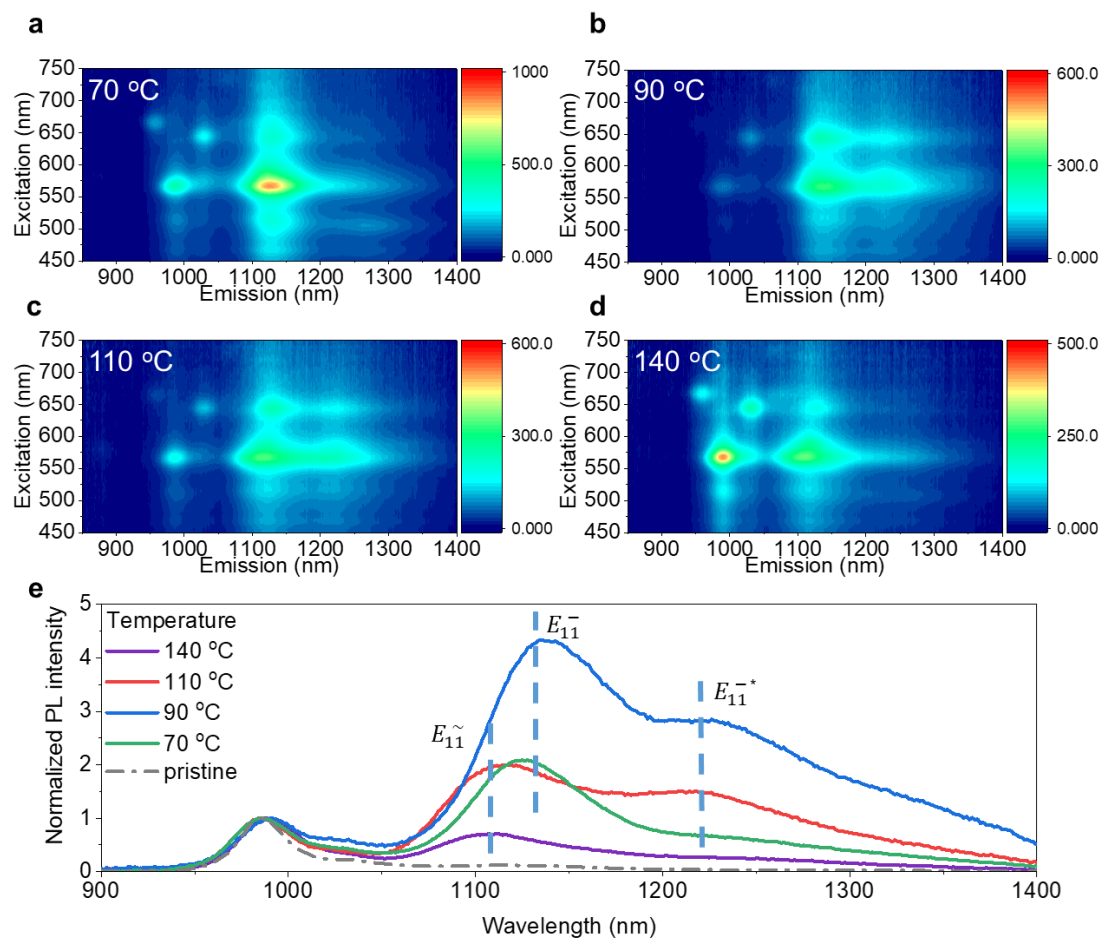
Figure 5-8. Temperature-dependent OCC emission from the reaction with MA. a-d, PL excitation maps of SWCNTs reacted with [MA] with [MA]:[C] = 20:1 at 70 °C (a), 90 °C (b), 110 °C (c), 140 °C (d). e, PL spectra of (6,5)-SWCNTs reacted at 70 °C (green), 90 °C (blue), 110 °C (red), 140 °C (purple). The PL spectra are normalized to the E_{11} emission of (6,5)-SWCNTs. Note that the E_{11} peak position of these 4 samples are slightly different, causing the E_{11}^-, $E_{11}^{\sim}$ and E_{11}^{-*} OCC emissions to vary compared to themselves.
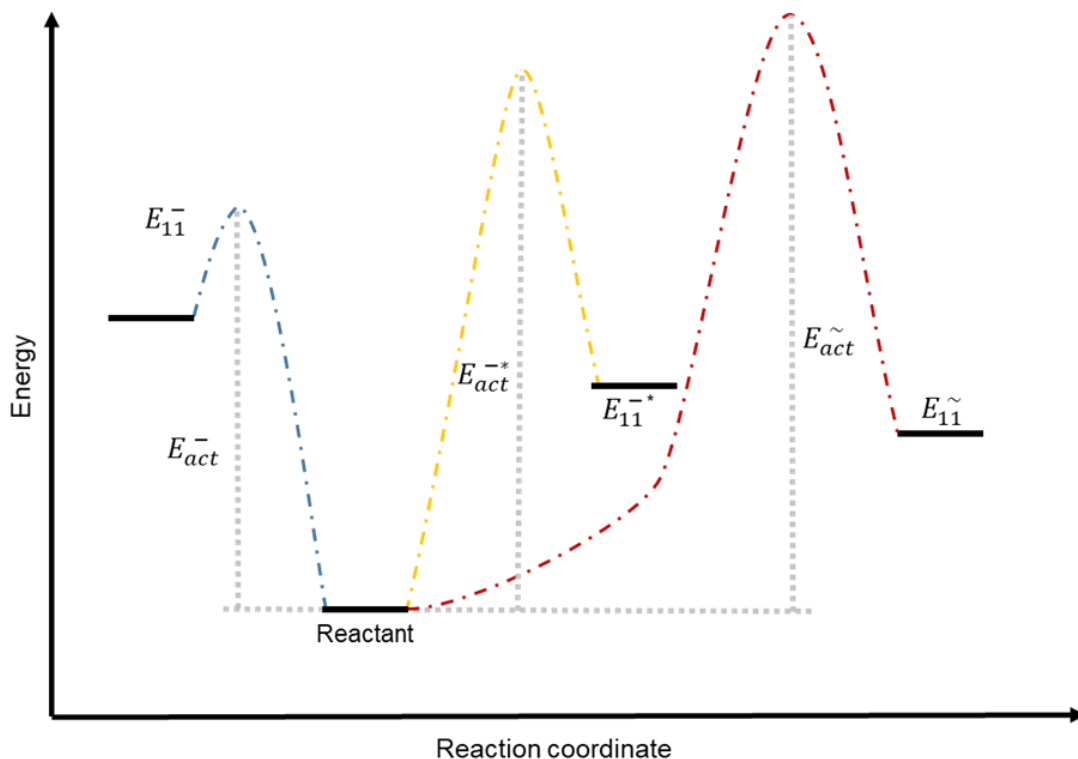
Figure 5-9. Schematic of reaction coordinate. The activation energy of 3 pathway to synthesize bonding configurations that emit at E_{11}^-, E_{11}^{-*} and $E_{11}^{\sim}$ are E_{act}^-, E_{act}^{-*}, and $E_{act}^{\sim}$. Note that the relative energy between reactant and each product was determined by DFT

To better understand the three OCC emissions, I utilized DFT and TD-DFT to calculate the optical properties of the N-MMI-(6,5)-SWCNTs. Three isomers of 10 nm long (6,5)-SWCNTs were installed with N-MMI OCCs via the [2+2] cycloaddition mechanism[200] at different pairing positions of PP(1/3, 1/3), PP(-2/3, 1/3), and PP(1/3, -2/3), as shown in Figure 5-10 (Note: I utilize this naming system of bonding configuration according to our previous study[193]). The total energies of each isomer were obtained from the geometry optimization listed in Table 5-2. The total energies are proportional to the Gibbs free energy of each isomer. Among the isomers, PP(-2/3, 1/3) had the lowest total energy. Thus, I calculated the relative total energy based on this most thermodynamically stable isomer, shown in Figure 5-10b. The total energies

130

of the PP(1/3, 1/3) and PP(1/3, -2/3) isomers were 0.10 eV and 0.068 eV, respectively, higher than that of PP(-2/3, 1/3), suggesting PP(1/3, -2/3) and PP(1/3, 1/3) may be kinetically favored products.

I further simulated the excited states of these isomers via TD-DFT. The OCC PL wavelengths of each isomer were simulated. Figure 5-10c and Table 5-3 show that PP(-2/3, 1/3), PP(1/3, 1/3), and PP(1/3,-2/3) have simulated OCC emission at 960 nm, 972nm, and 1186 nm, respectively. Compared to the experimental data shown in Figure 5-6, Figure 5-7, and Figure 5-8, the thermodynamic bonding configuration PP(-2/3, 1/3), thus, is related to the $E_{11}^{\sim}$ at 1112 nm, kinetic configuration PP(1/3, 1/3) can be assign to E_{11}^{-} at 1139 nm, while PP(1/3, -2/3) corresponds to E_{11}^{-*} at 1213 nm. This assignment agrees well with the experimental results (PL spectra superimposed in Figure 5-10c).
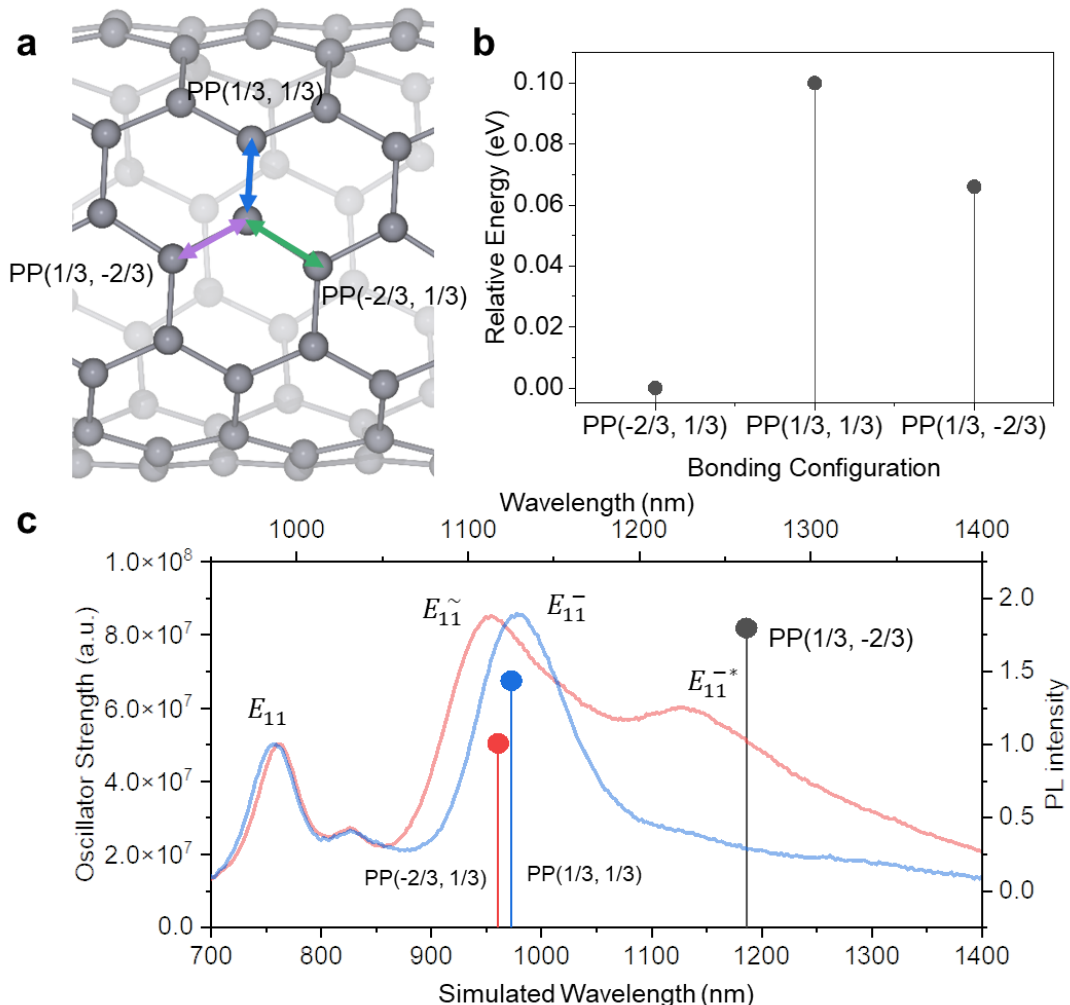
Figure 5-10. Emission and relative energy of the 3 possible bonding configurations of OCCs generated by N-MMI. a, A schematic of the OCC bonding configurations formed on the SWCNT based on the [2+2] cycloaddition reaction, in which the functional group is covalently bonded at a pair of nanotube carbon atoms indicated by PP(1/3, 1/3) (blue, 87° to the SWCNT axis), PP(1/3, -2/3) (purple, 27° to the SWCNT axis), and PP(-2/3, 1/3) (green, 33° to the SWCNT axis). b, DFT simulated relative total energies of N-MMI-(6,5)-SWCNT isomers with respect to the most stable structure of PP(-2/3, 1/3). c, TD-DFT simulated emission wavelength of OCCs featuring the PP(-2/3, 1/3), PP(1/3, 1/3) and PP(1/3, -2/3) bonding configurations (bottom and left axis), superimposed with the experimental PL spectra from N-MMI-(6,5)-SWCNTs at 80 °C (blue) and 100 °C (red) (top and right axis).

132

Table 5-2. Total energy and relative total energy of each bonding configuration obtained by DFT.

Configurations	Total energy (Hartree)	Relative total energy (eV)
PP(1/3, 1/3)	-34292.690947	0.100328
PP(1/3, -2/3)	-34292.692116	0.068518
PP(-2/3, 1/3)	- 34292.694634	0

Table 5-3. OCC emission energy of each bonding configuration obtained by TD-DFT

Configurations	Wavelength (nm)	Oscillator strength (a.u.)
PP(1/3, 1/3)	972.60	6.75×10^7
PP(1/3, -2/3)	1186.06	8.18×10^7
PP(-2/3, 1/3)	960.58	5.04×10^7

5.3 Conclusions

I demonstrate the addition of enophile molecules to SWCNTs can enable a [2+2] cycloaddition reaction that produces just three bonding configurations. The formation of two OCC isomers that emit at $E_{11}\tilde{}$ (1112 nm) and E_{11}^- (1139 nm) can be controlled by the reaction temperature. A low temperature favors the synthesis of E_{11}^-, which is likely a kinetically-favored product, while a higher temperature favors the production of $E_{11}\tilde{}$. The relative system energy and OCC emission wavelengths were calculated by DFT simulation, which I used to assign the OCC emissions to the different bonding configurations. Our results indicated the E_{11}^- and E_{11}^{-*} emissions are related to kinetic OCC products, while $E_{11}\tilde{}$ corresponds to the thermodynamically most stable bonding configuration. Our results demonstrate a scalable method that can be used for a variety of SWCNT chiralities to create structurally controlled OCCs at specific bonding configuration. This can help narrow down the OCC emission range, while the scalability can facilitate the fabrication of optical devices, such as single photon sources for quantum applications that require narrow emission.[21, 159]

5.4 Methods

5.4.1 Synthesis of OCCs.

The OCCs were synthesized using a [2+2] cycloaddition reaction based on the addition of various enophiles to the conjugated double-bond SWCNT structure. To conduct this reaction, ~1–5 mg of SWCNT powder (CoMoCat SG65i, Sigma Aldrich, Lot # MKBZ1159V) was added to ~5 mL of ethylene glycol (VWR, lot 000238286) in a 10 mL round bottom flask. Then ~2–15 mg of N-MMI (Sigma Aldrich, 97%), MA (Sigma Aldrich, 99%), or CPD (Sigma Aldrich, 95%) was added to the mixture of SWCNTs and ethylene glycol. I used different weights of N-MMI, MA, or CPD and the mole ratio of [EP]:[C] were calculated in each figure. [C] was calculated based on the mass of the SWCNT powder without considering the (6,5)-SWCNT purity. The round bottom flask was placed in a mineral oil bath and heated up to 70–140 $^{\circ}$C overnight. The reaction was stopped by cooling down to room temperature and filtering out the SWCNTs on a polyvinylidene fluoride membrane (MilliporeSigma VVLP membrane, 0.1 μm pore size), and then rinsed with ~50 mL Nanopure^{TM} water for at least three times. Then 5 mL of ethanol was used to rinse the SWCNTs for at least three times to remove the water. The powder was dried under vacuum at room temperature for 1 h to obtain a dry powder of SWCNTs.

5.4.2 Individual dispersion of OCC-SWCNTs.

The dry OCC-SWCNT powder was dispersed by ultrasonication (Misonix) in 1 wt% DOC (Sigma Aldrich)-H$_2$O solution at 4 W/mL for 30 min. Typically, ~1 mg of OCC-SWCNTs was dispersed by 1.5–2 mL 1 wt% DOC solution, followed by

centrifugation at 25000 g (1717 rad/s, 16400 rpm) for 1 h (Eppendorf centrifuge 5417 R) to remove bundled SWCNTs.

5.4.3 PL Characterization.

The ensemble PL spectra was collected using a NanoLog spectrofluorometer (Horiba Jobin Yvon). The samples were excited with a 450 W Xenon source dispersed by a double-grating monochromator. The slit width bandpass of the excitation and emission beams were both set to 10 nm. The PL spectra were collected using a liquid-N_2 cooled linear InGaAs array detector. The emission spectra were collected with excitation light at the E_{22} wavelength of each specific chirality. The integration time for the PL spectra and PL excitation map were 2–60 s and 5 s, respectively. Note that all samples were diluted with 1 wt% DOC and had an optical density at the E_{11} band of less than 0.5 (A/cm), measured using a PerkinElmer Lambda 1050 spectrophotometer with a broadband InGaAs detector.

To collect individual nanotube PL, the OCC-SWCNTs were imaged using the same hyperspectral imaging setup, as I previously reported.[34, 175] In brief, ~5 µL of the 1000-fold diluted OCC-SWCNTs solution was drop-cast onto a polystyrene-coated Au on Si substrate. The polystyrene layer acts as an insulating layer to prevent the SWCNTs from contacting with the Au, which would quench the PL, while the Au layer is used as a mirror to double the excitation and emission light. An infrared optimized 100x objective (LCPLN100XIR, numerical aperture (NA) = 0.85, Olympus) was used, along with a continuous wave laser at 730 nm (Shanghai Dream Lasers Technology Co., Ltd.) as the excitation light source. Fluorescent emission from the sample was filtered through a long pass dichroic mirror (875 nm edge, Semrock, USA), which

removed the elastic laser scattering from the sample, then dispersed by a volume Bragg grating (VBG; Photon Etc, Inc. Montreal, Canada). Only the diffracted light with a narrow bandwidth of 3.7 nm was collected on the detector to form a spectral image.

Raman spectroscopy was performed using a LabRAM ARAMIS Raman microscope (Horiba Jobin Yvon), 532 nm laser excitation (46 mW), and a 1.0 neutral density filter to prevent sample damage. The integration time was 1 s, taken 10 times in total. The dispersed nanotube solution was precipitated with ethanol and then deposited on a Si substrate, which simultaneously served as a reference with the Si peak at 520.7 cm^{-1} during the measurement.

5.4.4 *Density Functional Theory (DFT).*

All DFT calculations were performed with Gaussian 09 software.[186] A 10 nm (6,5)-SWCNT was functionalized with N-MMI at 3 ortho positions (PP(1/3,1/3), PP(1/3,-2/3), and PP(-2/3,1/3)), as shown in Figure 5-10. The geometries of all structures were optimized using the Coulomb-attenuated B3LYP (CAM-B3LYP) functional[187] and 3-21G basis set.[188] The optical transitions were computed using TD-DFT with the same functional and basis set as in DFT. I analyzed the natural transition orbitals (NTOs)[189] with Gaussian 09 software and confirmed that the NTOs were strongly localized at the OCC, further verifying the defect origin of the optical transitions (Figure 5-11).I note that the simulated peaks are higher energy compared to the experimental data due to the vacuum environment used in the simulation and the finite length of the SWCNTs. However, correction of the simulated peaks to the experimentally observed range was not performed as this correction is a qualitative adjustment and does not change the relative emission energy ordering of the OCCs with

different bonding configurations and requires significant additional computation expense.[178]
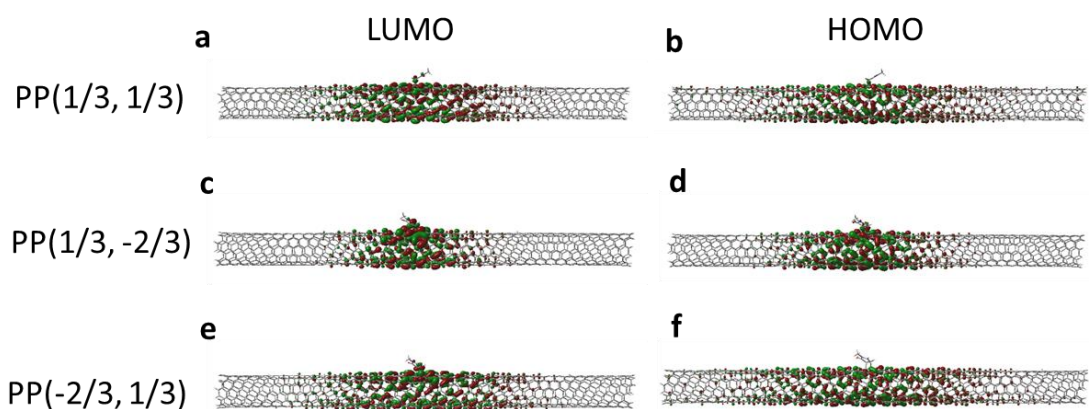
Figure 5-11. Natural transition orbitals of OCCs with different bonding configurations. (a) LUMO, and (b) HOMO of PP(1/3, 1/3). (c) LUMO, and (d) HOMO of PP(1/3, -2/3). (e) LUMO and (f) HOMO of PP(-2/3, 1/3). Note that only the NTO pairs that dominantly contribute to the transition (> 60%) are included in the plots.

6 Summary and Outlook

Parts of this chapter are adapted from published works I co-authored:

Wu, X.; Kim, M.; Qu, H.; Wang, Y. Single-Defect Spectroscopy in the Shortwave Infrared. Nat. Commun. 2019, 10, 2672.

Qu, H.; Rayabharam, A.; Wu, X.; Wang, P.; Li, Y.; Fagan, J.; Aluru, N. R.; Wang, Y., Selective Filling of N-Hexane in a Tight Nanopore. Nat. Commun. 2021, 12, 310.

Qu, H.; Wu, X.; Fortner, J.; Kim, M.; Wang, P.; Wang, Y., Reconfiguring Organic Color Centers on the sp² Carbon Lattice of Single-Walled Carbon Nanotubes. ACS Nano 2022, 16, 2077-2087.

Single-walled carbon nanotubes have intriguing electronic and optical properties, which arise from their 1D quantum confinement effect. The pore size of a specific chirality is well-defined by the chiral index (n, m). The interior channel of nanotubes is atomically smooth which allows a fast transport of liquid. The optical properties are affected by both outside and inside the nanotubes. Understanding the mechanism of molecules encapsulated inside the nanotubes is important to the fundamental physics and biology. Furthermore, the OCCs as an emerging light source that can be used for molecular sensing and single photon source which require a narrow emission. However, the asymmetric sp² carbon structure creates heterogeneous emissions, arising from the different bonding configurations. Managing and reducing the heterogeneity help to improve the applications of nanotubes where requires a narrow emission, such as quantum light sources, optoelectronics, bioimaging, and more. To enrich our knowledge in this emerging field, my research was directed to

provide new insights on the encapsulated molecules and the functional groups-controlled photoluminescence.

6.1 Summary

In this dissertation, I describe our custom-built hyperspectral imaging system that can be used for detecting molecular filling inside SWCNTs via the nanotube PL, and measuring the emissive OCCs. These OCCs are chemical defects that fluoresce in the shortwave infrared, which open exciting opportunities in deep-penetration bioimaging, chemically specific sensing, and quantum technologies. However, the atomic size of defects and the high noise of infrared detectors have posed significant challenges to the studies of these unique emitters at the single defect limit. I demonstrate high throughput single-defect spectroscopy in the shortwave infrared capable of quantitatively and spectrally resolving chemical defects at the single defect level. By cooling an InGaAs detector array down to -190 $^{\circ}$C and implementing a nondestructive readout scheme, I are able to capture low light fluorescent events in the shortwave infrared with a signal-to-noise ratio improved by more than three orders-of-magnitude. As a demonstration, I show it is possible to resolve individual chemical defects in carbon nanotube semiconductors, simultaneously collecting a full spectrum for each defect within the entire field of view.

Secondly, I achieved a molecular sieve using (6,5)-SWCNTs, which have a well-defined pore diameter, and established a dynamic microscopic view of molecules to reveal the mechanism which enables larger molecules to enter smaller pores. In nearly all known examples, the nanopore is larger than the molecule that selectively enters the pore. I experimentally demonstrate the ability of single-wall carbon

nanotubes with a van der Waals pore size of 0.42 nm to separate n-hexane from cyclohexane—despite the fact that both molecules have kinetic diameters larger than the rigid nanopore. This unexpected finding challenges our current understanding of nanopore selectivity and how molecules may enter a tight channel. Ab initio molecular dynamics simulations reveal that n-hexane molecules stretch by nearly 11.2 % inside the nanotube pore. Although at a relatively low probability (28.5 % overall), the stretched state of n-hexane does exist in the bulk solution, allowing the molecule to enter the tight pore even at room temperature. These new insights open up opportunities to engineer nanopore selectivity based on the molecular degrees of freedom.

Thirdly, I reported a laser irradiation method to address the OCCs emission heterogeneity problem. I show that laser irradiation of the nanotube host can locally reconfigure the chemical bonding of aryl OCCs on (6,5) nanotubes to significantly reduce their spectral inhomogeneity. After irradiation, the defect emission narrows in distribution by ~ 26% to yield a single photoluminescence peak. I use hyperspectral photoluminescence imaging to follow this structural transformation on the single nanotube level. Density functional theory calculations corroborate our experimental observations, suggesting that the OCCs convert from kinetic structures to the more thermodynamically stable configuration. This approach may allow localized tuning and creation of identical OCCs for emerging applications in bio-imaging, molecular sensing, and quantum information sciences.

Lastly, to further deal with the heterogeneity of OCC emission caused by the bonding configurations. I show that heat-activated [2+2] cycloaddition reactions lead to the synthesis of divalent OCCs with a reduced number of atomic configurations. The

chemistry occurs by simply mixing enophile molecules (e.g., methylmaleimide, maleic anhydride, and 4-cyclopentene-1,3-dione) with an ethylene glycol suspension of SWCNTs at elevated temperature (70–140 $^{\circ}$C). Unlike monovalent OCCs, I observe 3 types of OCC emissions at distinct wavelengths that I can assign to the three possible bonding configurations of divalent OCCs based on density functional theory calculations. Notably, these OCC photoluminescence peaks can be controlled by temperature to further decrease the emission heterogeneity. This divalent chemistry does not generate by-products, providing a scalable way to synthesize OCCs with controlled emission for emerging applications.

6.2 Outlook

SWCNTs are ideal model systems for studying liquids confined inside a nanopore. I have demonstrated the molecular sieving effect of organic molecules and revealed the mechanism behind the molecular encapsulation. The possibility of quantum sieving via pushing the pore size to even smaller to achieve isotope separation remains unexplored. It will have a considerable impact on the industrial application of purification of isotopes and liquids by reducing costs and increasing efficiency, as the smooth channel of SWCNTs enable an enhanced flow rate. Thus, it is important to develop new nanotube synthesis and chirality enriching methods to obtain nanotubes with even smaller diameter compared with the commonly used (6,5)-SWCNTs.

OCCs are emerging quantum emitters that can work at room temperature. They can potentially be used in a wide range of applications, such as quantum communication, biological imaging, and molecular sensing. Due to the structural asymmetricity, OCCs are generated as a mixture of different bonding configurations.

In this work, I have dealt with the structural heterogeneity either by converting the kinetic bonding configuration to thermodynamically stabled bonding configuration or by controlling the reaction mechanism via a [2+2] cycloaddition to reduce the numbers of resulting isomers. However, inability to control the interior environment that may potentially be filled with water or organic contaminants still broadens the emission range because the environment varies from nanotube to nanotube. Therefore, it is important to find an efficient and controllable method to create a stable and inert environment both inside and outside SWCNTs to further narrow emissions. For the application of sensing, once the analytes reach the OCCs, PL should respond via either peak shift or intensity change. Thus, a narrow and homogeneous OCC emission can improve the sensitivity and detection limit for molecules. Thus, I propose the combination of the research done in Chapter 3 to 5 to narrow the emissions by filling the interior with inert chemicals to control the endohedral environment that affect the PL, utilizing the [2+2] cycloaddition reaction to first reduce the possible bonding configuration of OCCs, then apply laser irradiation to further reduce them and convert the kinetic one to thermodynamically stable structure.

After a narrow emission is achieved, I would expect applications, such as lab-on-chip devices for detecting chemicals and quantum communication techniques, would be benefited from this improvement. I would propose a device with OCCs functionalized SWCNTs immobilized on the chip. The OCCs should selectively interact with analyte, for example, the OCCs can be linked to antibodies that can bond to certain protein causing the local electron cloud change inducing a change in the OCCs emission. On this device, the SWCNTs surface should be protected by some

inert chemical or polymer that prevent the interaction between SWCNT sp^2 lattice with the ionic species in the analyte which may quench or shift the PL. Only OCCs are exposed to the environment to serve as sensor sites. Other similar devices may also be invented. These OCCs can be used for deep tissue bioimaging and *in vivo* sensing, as the quantum yield and PL are greatly enhanced.

7 List of Publications

1. Aluru, N.; Aydin, F.; Bazant, M.; Blankschtein, D.; Brozena, A.; de Souza, J. P.; Elimelech, M.; Faucher, S.; Fourkas, J.; Koman, V.; Kuehne, M.; Kulik, H.; Li, H.; Li, Y.; Li, Z.; Majumdar, A.; Martis, J.; Misra, R.; Noy, A.; Pham, T. A.; Qu, H.; Rayabharam, A.; Reed, M.; Ritt, C.; Schwegler, E.; Siwy, Z.; Strano, M.; Wang, Y.; Yao, Y. ; Zhang, C.; Zhang, Z., Fluids and Electrolytes under Confinement in Single-Digit Nanopores. *Chem. Rev.* **2022**, Submitted.

2. Qu, H.; Wu, X.; Fortner, J.; Wang, Y., Thermally-controlled [2+2] cycloaddition produces divalent organic color-centers in single-walled carbon nanotubes with fewer atomic configurations. In preparation.

3. Rayabharam, A.; Qu, H.; Wang, Y.; Aluru, N. Spontaneous Sieving of Water from Ethanol-Water Mixtures using Single-Walled Carbon Nanotubes. In preparation.

4. Qu, H.; Wu, X.; Fortner, J.; Kim, M.; Wang, P.; Wang, Y., Reconfiguring Organic Color Centers on the Sp2 Carbon Lattice of Single-Walled Carbon Nanotubes. *ACS Nano* **2022**, *16*, 2077-2087.

5. Qu, H.; Rayabharam, A.; Wu, X.; Wang, P.; Li, Y.; Fagan, J.; Aluru, N. R.; Wang, Y., Selective Filling of N-Hexane in a Tight Nanopore. *Nat. Commun.* **2021**, 12, 310.

6. Huang, Z.; Powell, L. R.; Wu, X.; Kim, M.; Qu, H.; Wang, P.; Fortner, J. L.; Xu, B.; Ng, A. L.; Wang, Y., Photolithographic Patterning of Organic Color-Centers. *Adv. Mater.* **2020**, 32, e1906517.

7. Luo, H. B.; Wang, P.; Wu, X.; Qu, H.; Ren, X.; Wang, Y., One-Pot, Large-Scale Synthesis of Organic Color Center-Tailored Semiconducting Carbon Nanotubes. *ACS Nano* **2019**, 13, 8417-8424.

8. Wu, X.; Kim, M.; Qu, H.; Wang, Y., Single-Defect Spectroscopy in the Shortwave Infrared. *Nat. Commun.* **2019**, 10, 2672.

9. Wang, P.; Barnes, B.; Wu, X.; Qu, H.; Zhang, C.; Shi, Y.; Headrick, R. J.; Pasquali, M.; Wang, Y., Self-Sorting of 10-Microm-Long Single-Walled Carbon Nanotubes in Aqueous Solution. *Adv. Mater.* **2019**, 31, e1901641.

10. Luo, H. B.; Wang, P.; Wu, X.; Qu, H.; Ren, X.; Wang, Y., One-Pot, Large-Scale Synthesis of Organic Color Center-Tailored Semiconducting Carbon Nanotubes. *ACS Nano* **2019**, 13, 8417-8424.

11. Li, Y.; Wu, X.; Kim, M.; Fortner, J.; Qu, H.; Wang, Y., Fluorescent Ultrashort Nanotubes from Defect-Induced Chemical Cutting. *Chem. Mater.* **2019**, 31, 4536-4544.

Bibliography

1.   Radushkevich L.V., L. V. M., O Strukture Ugleroda, Obrazujucegosja Pri Termiceskom Razlozenii Okisi Ugleroda Na Zeleznom Kontakte (About the Structure of Carbon Formed by Thermal Decomposition of Carbon Monoxide on Iron Substrate). *Zurn. Fisic. Chim.* **1952**, *26*, 88-95.
2.   Iijima, S., Helical Microtubules of Graphitic Carbon. *Nature* **1991**, *354*, 56-58.
3.   Yu, M. F.; Lourie, O.; Dyer, M. J.; Moloni, K.; Kelly, T. F.; Ruoff, R. S., Strength and Breaking Mechanism of Multiwalled Carbon Nanotubes under Tensile Load. *Science* **2000**, *287*, 637-640.
4.   Treacy, M. M. J.; Ebbesen, T. W.; Gibson, J. M., Exceptionally High Young's Modulus Observed for Individual Carbon Nanotubes. *Nature* **1996**, *381*, 678-680.
5.   Yao, N.; Lordi, V., Young's Modulus of Single-Walled Carbon Nanotubes. *J. Appl. Phys.* **1998**, *84*, 1939-1943.
6.   Benedict, L. X.; Louie, S. G.; Cohen, M. L., Static Polarizabilities of Single-Wall Carbon Nanotubes. *Phys Rev B Condens Matter* **1995**, *52*, 8541-8549.
7.   Berber, S.; Kwon, Y.-K.; Tománek, D., Unusually High Thermal Conductivity of Carbon Nanotubes. *Phys. Rev. Lett.* **2000**, *84*, 4613-4616.
8.   Bethune, D. S.; Kiang, C. H.; de Vries, M. S.; Gorman, G.; Savoy, R.; Vazquez, J.; Beyers, R., Cobalt-Catalysed Growth of Carbon Nanotubes with Single-Atomic-Layer Walls. *Nature* **1993**, *363*, 605.
9.   Iijima, S.; Ichihashi, T., Single-Shell Carbon Nanotubes of 1-Nm Diameter. *Nature* **1993**, *363*, 603-605.
10.   Tunuguntla, R. H.; Allen, F. I.; Kim, K.; Belliveau, A.; Noy, A., Ultrafast Proton Transport in Sub-1-Nm Diameter Carbon Nanotube Porins. *Nat. Nanotechnol.* **2016**, *11*, 639-644.
11.   Agrawal, K. V.; Shimizu, S.; Drahushuk, L. W.; Kilcoyne, D.; Strano, M. S., Observation of Extreme Phase Transition Temperatures of Water Confined inside Isolated Carbon Nanotubes. *Nat. Nanotechnol.* **2017**, *12*, 267-273.
12.   Martel, R.; Schmidt, T.; Shea, H. R.; Hertel, T.; Avouris, P., Single- and Multi-Wall Carbon Nanotube Field-Effect Transistors. *Appl. Phys. Lett.* **1998**, *73*, 2447-2449.
13.   Javey, A.; Guo, J.; Wang, Q.; Lundstrom, M.; Dai, H., Ballistic Carbon Nanotube Field-Effect Transistors. *Nature* **2003**, *424*, 654-657.
14.   Barone, P. W.; Baik, S.; Heller, D. A.; Strano, M. S., Near-Infrared Optical Sensors Based on Single-Walled Carbon Nanotubes. *Nat. Mater.* **2004**, *4*, 86.
15.   Heller, D. A.; Jeng, E. S.; Yeung, T.-K.; Martinez, B. M.; Moll, A. E.; Gastala, J. B.; Strano, M. S., Optical Detection of DNA Conformational Polymorphism on Single-Walled Carbon Nanotubes. *Science* **2006**, *311*, 508.
16.   Kruss, S.; Hilmer, A. J.; Zhang, J.; Reuel, N. F.; Mu, B.; Strano, M. S., Carbon Nanotubes as Optical Biomedical Sensors. *Adv Drug Deliv Rev* **2013**, *65*, 1933-1950.
17.   Ackermann, J.; Metternich, J. T.; Herbertz, S.; Kruss, S., Biosensing with Fluorescent Carbon Nanotubes. *Angew Chem Int Ed Engl* **2022**, *n/a*, e202112372.

18.   Mandal, A. K.; Wu, X.; Ferreira, J. S.; Kim, M.; Powell, L. R.; Kwon, H.; Groc, L.; Wang, Y.; Cognet, L., Fluorescent Sp(3) Defect-Tailored Carbon Nanotubes Enable Nir-Ii Single Particle Imaging in Live Brain Slices at Ultra-Low Excitation Doses. *Sci. Rep.* **2020**, *10*, 5286.

19.   Luo, Y.; He, X.; Kim, Y.; Blackburn, J. L.; Doorn, S. K.; Htoon, H.; Strauf, S., Carbon Nanotube Color Centers in Plasmonic Nanocavities: A Path to Photon Indistinguishability at Telecom Bands. *Nano Lett.* **2019**, *19*, 9037-9044.

20.   Saha, A.; Gifford, B. J.; He, X.; Ao, G.; Zheng, M.; Kataura, H.; Htoon, H.; Kilina, S.; Tretiak, S.; Doorn, S. K., Narrow-Band Single-Photon Emission through Selective Aryl Functionalization of Zigzag Carbon Nanotubes. *Nat. Chem.* **2018**, *10*, 1089-1095.

21.   He, X.; Hartmann, N. F.; Ma, X.; Kim, Y.; Ihly, R.; Blackburn, J. L.; Gao, W.; Kono, J.; Yomogida, Y.; Hirano, A.; Tanaka, T.; Kataura, H.; Htoon, H.; Doorn, S. K., Tunable Room-Temperature Single-Photon Emission at Telecom Wavelengths from Sp3 Defects in Carbon Nanotubes. *Nat. Photonics* **2017**, *11*, 577-582.

22.   Bachilo, S. M.; Strano, M. S.; Kittrell, C.; Hauge, R. H.; Smalley, R. E.; Weisman, R. B., Structure-Assigned Optical Spectra of Single-Walled Carbon Nanotubes. *Science* **2002**, *298*, 2361-2366.

23.   Yang, F.; Wang, M.; Zhang, D.; Yang, J.; Zheng, M.; Li, Y., Chirality Pure Carbon Nanotubes: Growth, Sorting, and Characterization. *Chem Rev* **2020**, *120*, 2693-2758.

24.   Saito, R.; Dresselhaus, G.; Dresselhaus, M. S., Trigonal Warping Effect of Carbon Nanotubes. *Phys. Rev. B* **2000**, *61*, 2981-2990.

25.   Miyauchi, Y., Photoluminescence Studies on Exciton Photophysics in Carbon Nanotubes. *J. Mater. Chem. C* **2013**, *1*, 6499–6521.

26.   O'Connell, M. J.; Bachilo, S. M.; Huffman, C. B.; Moore, V. C.; Strano, M. S.; Haroz, E. H.; Rialon, K. L.; Boul, P. J.; Noon, W. H.; Kittrell, C.; Ma, J.; Hauge, R. H.; Weisman, R. B.; Smalley, R. E., Band Gap Fluorescence from Individual Single-Walled Carbon Nanotubes. *Science* **2002**, *297*, 593-596.

27.   Graf, A.; Zakharko, Y.; Schießl, S. P.; Backes, C.; Pfohl, M.; Flavel, B. S.; Zaumseil, J., Large Scale, Selective Dispersion of Long Single-Walled Carbon Nanotubes with High Photoluminescence Quantum Yield by Shear Force Mixing. *Carbon* **2016**, *105*, 593-599.

28.   Wang, P.; Kim, M.; Peng, Z.; Sun, C.-F.; Mok, J.; Lieberman, A.; Wang, Y., Superacid-Surfactant Exchange: Enabling Nondestructive Dispersion of Full-Length Carbon Nanotubes in Water. *ACS Nano* **2017**, *11*, 9231-9238.

29.   Wang, P.; Barnes, B.; Wu, X.; Qu, H.; Zhang, C.; Shi, Y.; Headrick, R. J.; Pasquali, M.; Wang, Y., Self-Sorting of 10-Microm-Long Single-Walled Carbon Nanotubes in Aqueous Solution. *Adv. Mater.* **2019**, *31*, e1901641.

30.   Perebeinos, V.; Tersoff, J.; Avouris, P., Effect of Exciton-Phonon Coupling in the Calculated Optical Absorption of Carbon Nanotubes. *Phys. Rev. Lett.* **2005**, *94*, 027402.

31.   Wang, R. K.; Chen, W. C.; Campos, D. K.; Ziegler, K. J., Swelling the Micelle Core Surrounding Single-Walled Carbon Nanotubes with Water-Immiscible Organic Solvents. *J. Am. Chem. Soc.* **2008**, *130*, 16330-16337.

32.   Barone, P. W.; Yoon, H.; Ortiz-Garcia, R.; Zhang, J.; Ahn, J. H.; Kim, J. H.; Strano, M. S., Modulation of Single-Walled Carbon Nanotube Photoluminescence by Hydrogel Swelling. *ACS Nano* **2009**, *3*, 3869-3877.

33.   Cambre, S.; Santos, S. M.; Wenseleers, W.; Nugraha, A. R.; Saito, R.; Cognet, L.; Lounis, B., Luminescence Properties of Individual Empty and Water-Filled Single-Walled Carbon Nanotubes. *ACS Nano* **2012**, *6*, 2649-2655.

34.   Qu, H.; Rayabharam, A.; Wu, X.; Wang, P.; Li, Y.; Fagan, J.; Aluru, N. R.; Wang, Y., Selective Filling of N-Hexane in a Tight Nanopore. *Nat. Commun.* **2021**, *12*, 310.

35.   Campo, J.; Cambre, S.; Botka, B.; Obrzut, J.; Wenseleers, W.; Fagan, J. A., Optical Property Tuning of Single-Wall Carbon Nanotubes by Endohedral Encapsulation of a Wide Variety of Dielectric Molecules. *ACS Nano* **2021**, *15*, 2301-2317.

36.   Högele, A.; Galland, C.; Winger, M.; Imamoğlu, A., Photon Antibunching in the Photoluminescence Spectra of a Single Carbon Nanotube. *Phys. Rev. Lett.* **2008**, *100*, 217401.

37.   Hong, G.; Diao, S.; Antaris, A. L.; Dai, H., Carbon Nanomaterials for Biological Imaging and Nanomedicinal Therapy. *Chem. Rev.* **2015**, *115*, 10816-10906.

38.   Dresselhaus, M. S.; Dresselhaus, G.; Saito, R.; Jorio, A., Raman Spectroscopy of Carbon Nanotubes. *Phys. Rep.* **2005**, *409*, 47-99.

39.   Malard, L. M.; Pimenta, M. A.; Dresselhaus, G.; Dresselhaus, M. S., Raman Spectroscopy in Graphene. *Phys. Rep.* **2009**, *473*, 51-87.

40.   Faucher, S.; Kuehne, M.; Koman, V. B.; Northrup, N.; Kozawa, D.; Yuan, Z.; Li, S. X.; Zeng, Y.; Ichihara, T.; Misra, R. P.; Aluru, N.; Blankschtein, D.; Strano, M. S., Diameter Dependence of Water Filling in Lithographically Segmented Isolated Carbon Nanotubes. *ACS Nano* **2021**, *15*, 2778-2790.

41.   Faucher, S.; Aluru, N.; Bazant, M. Z.; Blankschtein, D.; Brozena, A. H.; Cumings, J.; Pedro de Souza, J.; Elimelech, M.; Epsztein, R.; Fourkas, J. T.; Rajan, A. G.; Kulik, H. J.; Levy, A.; Majumdar, A.; Martin, C.; McEldrew, M.; Misra, R. P.; Noy, A.; Pham, T. A.; Reed, M., et al., Critical Knowledge Gaps in Mass Transport through Single-Digit Nanopores: A Review and Perspective. *J. Phys. Chem. C* **2019**, *123*, 21309-21326.

42.   Hebbar, R. S.; Isloor, A. M.; Inamuddin; Asiri, A. M., Carbon Nanotube- and Graphene-Based Advanced Membrane Materials for Desalination. *Environ. Chem. Lett.* **2017**, *15*, 643-671.

43.   Das, R.; Ali, M. E.; Hamid, S. B. A.; Ramakrishna, S.; Chowdhury, Z. Z., Carbon Nanotube Membranes for Water Purification: A Bright Future in Water Desalination. *Desalination* **2014**, *336*, 97-109.

44.   Ghosh, S.; Sood, A. K.; Kumar, N., Carbon Nanotube Flow Sensors. *Science* **2003**, *299*, 1042-1044.

45.   Yang, Y.; Dementyev, P.; Biere, N.; Emmrich, D.; Stohmann, P.; Korzetz, R.; Zhang, X.; Beyer, A.; Koch, S.; Anselmetti, D.; Golzhauser, A., Rapid Water Permeation through Carbon Nanomembranes with Sub-Nanometer Channels. *ACS Nano* **2018**, *12*, 4695-4701.

46.   Verweij, H.; Schillo, M. C.; Li, J., Fast Mass Transport through Carbon Nanotube Membranes. *Small* **2007**, *3*, 1996-2004.

47.   Fornasiero, F.; Park, H. G.; Holt, J. K.; Stadermann, M.; Grigoropoulos, C. P.; Noy, A.; Bakajin, O., Ion Exclusion by Sub-2-Nm Carbon Nanotube Pores. *Proc. Natl. Acad. Sci. U. S. A.* **2008**, *105*, 17250-17255.

48.   Campo, J.; Piao, Y.; Lam, S.; Stafford, C. M.; Streit, J. K.; Simpson, J. R.; Hight Walker, A. R.; Fagan, J. A., Enhancing Single-Wall Carbon Nanotube Properties through Controlled Endohedral Filling. *Nanoscale Horiz* **2016**, *1*, 317-324.

49.   Fagan, J. A.; Huh, J. Y.; Simpson, J. R.; Blackburn, J. L.; Holt, J. M.; Larsen, B. A.; Walker, A. R., Separation of Empty and Water-Filled Single-Wall Carbon Nanotubes. *ACS Nano* **2011**, *5*, 3943-3953.

50.   Cambre, S.; Wenseleers, W., Separation and Diameter-Sorting of Empty (End-Capped) and Water-Filled (Open) Carbon Nanotubes by Density Gradient Ultracentrifugation. *Angew. Chem. Int. Ed. Engl.* **2011**, *50*, 2764-2768.

51.   Ao, G.; Streit, J. K.; Fagan, J. A.; Zheng, M., Differentiating Left- and Right-Handed Carbon Nanotubes by DNA. *J. Am. Chem. Soc.* **2016**, *138*, 16677-16685.

52.   Ao, G.; Khripin, C. Y.; Zheng, M., DNA-Controlled Partition of Carbon Nanotubes in Polymer Aqueous Two-Phase Systems. *J. Am. Chem. Soc.* **2014**, *136*, 10383-10392.

53.   Fagan, J. A.; Haroz, E. H.; Ihly, R.; Gui, H.; Blackburn, J. L.; Simpson, J. R.; Lam, S.; Hight Walker, A. R.; Doorn, S. K.; Zheng, M., Isolation of >1 Nm Diameter Single-Wall Carbon Nanotube Species Using Aqueous Two-Phase Extraction. *ACS Nano* **2015**, *9*, 5377-5390.

54.   Crochet, J.; Clemens, M.; Hertel, T., Quantum Yield Heterogeneities of Aqueous Single-Wall Carbon Nanotube Suspensions. *J. Am. Chem. Soc.* **2007**, *129*, 8058-8059.

55.   Brozena, A. H.; Kim, M.; Powell, L. R.; Wang, Y., Controlling the Optical Properties of Carbon Nanotubes with Organic Colour-Centre Quantum Defects. *Nat. Rev. Chem.* **2019**, *3*, 375-392.

56.   Zhang, Y.; Valley, N.; Brozena, A. H.; Piao, Y.; Song, X.; Schatz, G. C.; Wang, Y., Propagative Sidewall Alkylcarboxylation That Induces Red-Shifted near-Ir Photoluminescence in Single-Walled Carbon Nanotubes. *J. Phys. Chem. Lett.* **2013**, *4*, 826-830.

57.   Piao, Y.; Meany, B.; Powell, L. R.; Valley, N.; Kwon, H.; Schatz, G. C.; Wang, Y., Brightening of Carbon Nanotube Photoluminescence through the Incorporation of Sp^3 Defects. *Nat. Chem.* **2013**, *5*, 840-845.

58.   Kwon, H.; Furmanchuk, A.; Kim, M.; Meany, B.; Guo, Y.; Schatz, G. C.; Wang, Y., Molecularly Tunable Fluorescent Quantum Defects. *J. Am. Chem. Soc.* **2016**, *138*, 6878-6885.

59.   Piao, Y.; Meany, B.; Powell, L. R.; Valley, N.; Kwon, H.; Schatz, G. C.; Wang, Y., Brightening of Carbon Nanotube Photoluminescence through the Incorporation of Sp3 Defects. *Nat. Chem.* **2013**, *5*, 840-845.

60.   Kwon, H.; Kim, M.; Meany, B.; Piao, Y.; Powell, L. R.; Wang, Y., Optical Probing of Local Ph and Temperature in Complex Fluids with Covalently Functionalized, Semiconducting Carbon Nanotubes. *J. Phys. Chem. C* **2015**, *119*, 3733-3739.

61.   Cognet, L.; Tsyboulski, D. A.; Rocha, J. D.; Doyle, C. D.; Tour, J. M.; Weisman, R. B., Stepwise Quenching of Exciton Fluorescence in Carbon Nanotubes by Single-Molecule Reactions. *Science* **2007**, *316*, 1465-1468.

62.   Powell, L. R.; Piao, Y.; Wang, Y., Optical Excitation of Carbon Nanotubes Drives Localized Diazonium Reactions. *J. Phys. Chem. Lett.* **2016**, *7*, 3690-3694.

63.   Powell, L. R.; Kim, M.; Wang, Y., Chirality-Selective Functionalization of Semiconducting Carbon Nanotubes with a Reactivity-Switchable Molecule. *J. Am. Chem. Soc.* **2017**, *139*, 12533-12540.

64.   Wu, X.; Kim, M.; Kwon, H.; Wang, Y., Photochemical Creation of Fluorescent Quantum Defects in Semiconducting Carbon Nanotube Hosts. *Angew. Chem. Int. Ed. Engl.* **2018**, *57*, 648-653.

65.   Luo, H. B.; Wang, P.; Wu, X.; Qu, H.; Ren, X.; Wang, Y., One-Pot, Large-Scale Synthesis of Organic Color Center-Tailored Semiconducting Carbon Nanotubes. *ACS Nano* **2019**, *13*, 8417-8424.

66.   Berger, F. J.; Luttgens, J.; Nowack, T.; Kutsch, T.; Lindenthal, S.; Kistner, L.; Muller, C. C.; Bongartz, L. M.; Lumsargis, V. A.; Zakharko, Y.; Zaumseil, J., Brightening of Long, Polymer-Wrapped Carbon Nanotubes by Sp3 Functionalization in Organic Solvents. *ACS Nano* **2019**, *13*, 9259-9269.

67.   Schmidt, G.; Gallon, S.; Esnouf, S.; Bourgoin, J. P.; Chenevier, P., Mechanism of the Coupling of Diazonium to Single-Walled Carbon Nanotubes and Its Consequences. *Chem. Eur. J.* **2009**, *15*, 2101-2110.

68.   He, X.; Gifford, B. J.; Hartmann, N. F.; Ihly, R.; Ma, X.; Kilina, S. V.; Luo, Y.; Shayan, K.; Strauf, S.; Blackburn, J. L.; Tretiak, S.; Doorn, S. K.; Htoon, H., Low-Temperature Single Carbon Nanotube Spectroscopy of Sp3 Quantum Defects. *ACS Nano* **2017**, *11*, 10785-10796.

69.   Kim, M.; Adamska, L.; Hartmann, N. F.; Kwon, H.; Liu, J.; Velizhanin, K. A.; Piao, Y.; Powell, L. R.; Meany, B.; Doorn, S. K.; Tretiak, S.; Wang, Y., Fluorescent Carbon Nanotube Defects Manifest Substantial Vibrational Reorganization. *J. Phys. Chem. C* **2016**, *120*, 11268-11276.

70.   He, X.; Sun, L.; Gifford, B. J.; Tretiak, S.; Piryatinski, A.; Li, X.; Htoon, H.; Doorn, S. K., Intrinsic Limits of Defect-State Photoluminescence Dynamics in Functionalized Carbon Nanotubes. *Nanoscale* **2019**, *11*, 9125-9132.

71.   Dresselhaus, M. S.; Dresselhaus, G.; Saito, R., Physics of Carbon Nanotubes. *Carbon* **1995**, *33*, 883-891.

72.   Gifford, B. J.; Kilina, S.; Htoon, H.; Doorn, S. K.; Tretiak, S., Exciton Localization and Optical Emission in Aryl-Functionalized Carbon Nanotubes. *J. Phys. Chem. C* **2018**, *122*, 1828-1838.

73.   Niyogi, S.; Hamon, M. A.; Hu, H.; Zhao, B.; Bhowmik, P.; Sen, R.; Itkis, M. E.; Haddon, R. C., Chemistry of Single-Walled Carbon Nanotubes. *Acc. Chem. Res.* **2002**, *35*, 1105-1113.

74.   Manzeli, S.; Ovchinnikov, D.; Pasquier, D.; Yazyev, O. V.; Kis, A., 2d Transition Metal Dichalcogenides. *Nat. Rev. Mater.* **2017**, *2*, 17033.

75.   Choi, W.; Choudhary, N.; Han, G. H.; Park, J.; Akinwande, D.; Lee, Y. H., Recent Development of Two-Dimensional Transition Metal Dichalcogenides and Their Applications. *Mater. Today* **2017**, *20*, 116-130.

76.   Celis, A.; Nair, M. N.; Taleb-Ibrahimi, A.; Conrad, E. H.; Berger, C.; de Heer, W. A.; Tejeda, A., Graphene Nanoribbons: Fabrication, Properties and Devices. *J. Phys. D: Appl. Phys.* **2016**, *49*, 143001.

77.   Narlikar, A. V.; Fu, Y. Y.; Collins, P. G., Defects and Disorder in Carbon Nanotubes. **2017**, *1*.

78.   Dresselhaus, M. S., Fifty Years in Studying Carbon-Based Materials. *Phys. Scr.* **2012**, *T146*, 014002.

79.   Hong, J.; Jin, C.; Yuan, J.; Zhang, Z., Atomic Defects in Two-Dimensional Materials: From Single-Atom Spectroscopy to Functionalities in Opto-/Electronics, Nanomagnetism, and Catalysis. *Adv. Mater.* **2017**, *29*, 1606434-1606466.

80.   Brozena, A. K., M.; Powel, L. R.; Wang, Y.H, Controlling the Physical Properties of Carbon Nanotubes with Quantum Defects. *Nat. Rev. Chem.* **2019**.

81.   He, X.; Gifford, B. J.; Hartmann, N. F.; Ihly, R.; Ma, X.; Kilina, S. V.; Luo, Y.; Shayan, K.; Strauf, S.; Blackburn, J. L.; Tretiak, S.; Doorn, S. K.; Htoon, H., Low-Temperature Single Carbon Nanotube Spectroscopy of Sp(3) Quantum Defects. *ACS Nano* **2017**, *11*, 10785-10796.

82.   Deng, S.; Zhang, Y.; Brozena, A. H.; Mayes, M. L.; Banerjee, P.; Chiou, W. A.; Rubloff, G. W.; Schatz, G. C.; Wang, Y., Confined Propagation of Covalent Chemical Reactions on Single-Walled Carbon Nanotubes. *Nat. Commun.* **2011**, *2*, 382.

83.   Bruns, O. T.; Bischof, T. S.; Harris, D. K.; Franke, D.; Shi, Y.; Riedemann, L.; Bartelt, A.; Jaworski, F. B.; Carr, J. A.; Rowlands, C. J.; Wilson, M. W. B.; Chen, O.; Wei, H.; Hwang, G. W.; Montana, D. M.; Coropceanu, I.; Achorn, O. B.; Kloepper, J.; Heeren, J.; So, P. T. C., et al., Next-Generation in Vivo Optical Imaging with Short-Wave Infrared Quantum Dots. *Nat. Biomed. Eng.* **2017**, *1*, 0056.

84.   Carr, J. A.; Franke, D.; Caram, J. R.; Perkinson, C. F.; Saif, M.; Askoxylakis, V.; Datta, M.; Fukumura, D.; Jain, R. K.; Bawendi, M. G.; Bruns, O. T., Shortwave Infrared Fluorescence Imaging with the Clinically Approved near-Infrared Dye Indocyanine Green. *Proceedings of the National Academy of Sciences of the United States of America* **2018**, *115*, 4465-4470.

85.   Gisin, N.; Thew, R., Quantum Communication. *Nat. Photonics* **2007**, *1*, 165-171.

86.   He, X.; Hartmann, N. F.; Ma, X.; Kim, Y.; Ihly, R.; Blackburn, J. L.; Gao, W.; Kono, J.; Yomogida, Y.; Hirano, A.; Tanaka, T.; Kataura, H.; Htoon, H.; Doorn, S. K., Tunable Room-Temperature Single-Photon Emission at Telecom Wavelengths from Sp3 Defects in Carbon Nanotubes. *Nat. Photonics* **2017**, *11*, 577-582.

87.   He, X.; Htoon, H.; Doorn, S. K.; Pernice, W. H. P.; Pyatkov, F.; Krupke, R.; Jeantet, A.; Chassagneux, Y.; Voisin, C., Carbon Nanotubes as Emerging Quantum-Light Sources. *Nat. Mater.* **2018**, *17*, 663-670.

88.   Bosma, T.; Lof, G. J. J.; Gilardoni, C. M.; Zwier, O. V.; Hendriks, F.; Magnusson, B.; Ellison, A.; Gallstrom, A.; Ivanov, I. G.; Son, N. T.; Havenith, R. W. A.; van der Wal, C. H., Identification and Tunable Optical Coherent Control of Transition-Metal Spins in Silicon Carbide. *Npj Quantum Inform.* **2018**, *4*, 48.

89.   Hong, G.; Diao, S.; Chang, J.; Antaris, A. L.; Chen, C.; Zhang, B.; Zhao, S.; Atochin, D. N.; Huang, P. L.; Andreasson, K. I.; Kuo, C. J.; Dai, H., Through-Skull

Fluorescence Imaging of the Brain in a New near-Infrared Window. *Nat. Photonics* **2014**, *8*, 723-730.

90.   Zhang, H.; Salo, D.; Kim, D. M.; Komarov, S.; Tai, Y. C.; Berezin, M. Y., Penetration Depth of Photons in Biological Tissues from Hyperspectral Imaging in Shortwave Infrared in Transmission and Reflection Geometries. *J. Biomed. Opt.* **2016**, *21*, 126006.

91.   Welsher, K.; Liu, Z.; Sherlock, S. P.; Robinson, J. T.; Chen, Z.; Daranciang, D.; Dai, H., A Route to Brightly Fluorescent Carbon Nanotubes for near-Infrared Imaging in Mice. *Nat. Nanotechnol.* **2009**, *4*, 773-780.

92.   Hong, G. S.; Lee, J. C.; Robinson, J. T.; Raaz, U.; Xie, L. M.; Huang, N. F.; Cooke, J. P.; Dai, H. J., Multifunctional in Vivo Vascular Imaging Using near-Infrared Ii Fluorescence. *Nat. Med.* **2012**, *18*, 1841.

93.   Ghosh, D.; Bagley, A. F.; Na, Y. J.; Birrer, M. J.; Bhatia, S. N.; Belcher, A. M., Deep, Noninvasive Imaging and Surgical Guidance of Submillimeter Tumors Using Targeted M13-Stabilized Single-Walled Carbon Nanotubes. *Proc. Natl. Acad. Sci. U. S. A.* **2014**, *111*, 13948-13953.

94.   Gruber, A., Scanning Confocal Optical Microscopy and Magnetic Resonance on Single Defect Centers. *Science* **1997**, *276*, 2012-2014.

95.   Francoeur, S.; Klem, J. F.; Mascarenhas, A., Optical Spectroscopy of Single Impurity Centers in Semiconductors. *Phys. Rev. Lett.* **2004**, *93*, 067403.

96.   Danne, N.; Kim, M.; Godin, A. G.; Kwon, H.; Gao, Z.; Wu, X.; Hartmann, N. F.; Doorn, S. K.; Lounis, B.; Wang, Y.; Cognet, L., Ultrashort Carbon Nanotubes That Fluoresce Brightly in the near-Infrared. *ACS Nano* **2018**, *12*, 6059-6065.

97.   Crochet, J. J.; Duque, J. G.; Werner, J. H.; Doorn, S. K., Photoluminescence Imaging of Electronic-Impurity-Induced Exciton Quenching in Single-Walled Carbon Nanotubes. *Nat. Nanotechnol.* **2012**, *7*, 126-132.

98.   Rust, M. J.; Bates, M.; Zhuang, X., Sub-Diffraction-Limit Imaging by Stochastic Optical Reconstruction Microscopy (Storm). *Nat. Methods* **2006**, *3*, 793-795.

99.   Lee, S. H.; Baday, M.; Tjioe, M.; Simonson, P. D.; Zhang, R.; Cai, E.; Selvin, P. R., Using Fixed Fiduciary Markers for Stage Drift Correction. *Opt. Express* **2012**, *20*, 12177-12183.

100.   Wu, X.; Kim, M.; Kwon, H.; Wang, Y., Photochemical Creation of Fluorescent Quantum Defects in Semiconducting Carbon Nanotube Hosts. *Angew. Chem., Int. Ed. Engl.* **2018**, *57*, 648-653.

101.   Kim, M.; Wu, X. J.; Ao, G. Y.; He, X. W.; Kwon, H.; Hartmann, N. F.; Zheng, M.; Doorn, S. K.; Wang, Y. H., Mapping Structure-Property Relationships of Organic Color Centers. *Chem* **2018**, *4*, 2180-2191.

102.   Ma, Y. Z.; Valkunas, L.; Dexheimer, S. L.; Bachilo, S. M.; Fleming, G. R., Femtosecond Spectroscopy of Optical Excitations in Single-Walled Carbon Nanotubes: Evidence for Exciton-Exciton Annihilation. *Phys. Rev. Lett.* **2005**, *94*, 157402.

103.   Ai, N.; Walden-Newman, W.; Song, Q.; Kalliakos, S.; Strauf, S., Suppression of Blinking and Enhanced Exciton Emission from Individual Carbon Nanotubes. *ACS Nano* **2011**, *5*, 2664-2670.

104.   Thompson, R. E.; Larson, D. R.; Webb, W. W., Precise Nanometer Localization Analysis for Individual Fluorescent Probes. *Biophys. J.* **2002**, *82*, 2775-2783.

105.   Ma, X.; Adamska, L.; Yamaguchi, H.; Yalcin, S. E.; Tretiak, S.; Doorn, S. K.; Htoon, H., Electronic Structure and Chemical Nature of Oxygen Dopant States in Carbon Nanotubes. *ACS Nano* **2014**, *8*, 10782-10789.

106.   Harvey, J. D.; Baker, H. A.; Mercer, E.; Budhathoki-Uprety, J.; Heller, D. A., Control of Carbon Nanotube Solvatochromic Response to Chemotherapeutic Agents. *ACS Appl. Mater. Interfaces* **2017**, *9*, 37947-37953.

107.   Roxbury, D.; Jena, P. V.; Williams, R. M.; Enyedi, B.; Niethammer, P.; Marcet, S.; Verhaegen, M.; Blais-Ouellette, S.; Heller, D. A., Hyperspectral Microscopy of near-Infrared Fluorescence Enables 17-Chirality Carbon Nanotube Imaging. *Sci. Rep.* **2015**, *5*, 14167.

108.   Marchetti, P.; Jimenez Solomon, M. F.; Szekely, G.; Livingston, A. G., Molecular Separation with Organic Solvent Nanofiltration: A Critical Review. *Chem. Rev.* **2014**, *114*, 10735-10806.

109.   Koros, W. J.; Zhang, C., Materials for Next-Generation Molecularly Selective Synthetic Membranes. *Nat. Mater.* **2017**, *16*, 289-297.

110.   Faucher, S.; Aluru, N.; Bazant, M. Z.; Blankschtein, D.; Brozena, A. H.; Cumings, J.; Pedro de Souza, J.; Elimelech, M.; Epsztein, R.; Fourkas, J. T.; Rajan, A. G.; Kulik, H. J.; Levy, A.; Majumdar, A.; Martin, C.; McEldrew, M.; Misra, R. P.; Noy, A.; Pham, T. A.; Reed, M., et al., Critical Knowledge Gaps in Mass Transport through Single-Digit Nanopores: A Review and Perspective. *J. Phys. Chem. C* **2019**, *123*, 21309-21326.

111.   Barker, B. S.; Young, G. T.; Soubrane, C. H.; Stephens, G. J.; Stevens, E. B.; Patel, M. K., Ion Channels. In *Conn's Translational Neuroscience*, Conn, P. M., Ed. Academic Press: San Diego, 2017; pp 11-43.

112.   Dyer, A., *An Introduction to Zeolite Molecular Sieves*. John Wiley & Sons: United States, 1988.

113.   Smit, B.; Maesen, T. L., Towards a Molecular Understanding of Shape Selectivity. *Nature* **2008**, *451*, 671-678.

114.   Sui, H.; Han, B. G.; Lee, J. K.; Walian, P.; Jap, B. K., Structural Basis of Water-Specific Transport through the Aqp1 Water Channel. *Nature* **2001**, *414*, 872-878.

115.   Kong, Y.; Ma, J., Dynamic Mechanisms of the Membrane Water Channel Aquaporin-1 (Aqp1). *Proc. Natl. Acad. Sci. U.S.A.* **2001**, *98*, 14345-14349.

116.   Luna-Triguero, A.; Gomez-Alvarez, P.; Calero, S., Adsorptive Process Design for the Separation of Hexane Isomers Using Zeolites. *Phys. Chem. Chem. Phys.* **2017**, *19*, 5037-5042.

117.   Bachilo, S. M.; Strano, M. S.; Kittrell, C.; Hauge, R. H.; Smalley, R. E.; Weisman, R. B., Structure-Assigned Optical Spectra of Single-Walled Carbon Nanotubes. *Science* **2002**, *298*, 2361-2366.

118.   Tunuguntla, R. H.; Henley, R. Y.; Yao, Y.-C.; Pham, T. A.; Wanunu, M.; Noy, A., Enhanced Water Permeability and Tunable Ion Selectivity in Subnanometer Carbon Nanotube Porins. *Science* **2017**, *357*, 792.

119.   Lee, C. Y.; Choi, W.; Han, J.-H.; Strano, M. S., Coherence Resonance in a Single-Walled Carbon Nanotube Ion Channel. *Science* **2010**, *329*, 1320.

120.   Ferreira, A. F.; Mittelmeijer-Hazeleger, M. C.; Granato, M. A.; Martins, V. F.; Rodrigues, A. E.; Rothenberg, G., Sieving Di-Branched from Mono-Branched and Linear Alkanes Using Zif-8: Experimental Proof and Theoretical Explanation. *Phys. Chem. Chem. Phys.* **2013**, *15*, 8795-8804.

121.   Breck, D. W., *Zeolite Molecular Sieves: Structure, Chemistry, and Use*. John Wiley & Sons: New York, 1973.

122.   Muller, J. A.; Conner, W. C., Cyclohexane in Zsm 5. 1. Ftir and X-Ray Studies. *J. Phys. Chem.* **2002**, *97*, 1451-1454.

123.   Cambre, S.; Santos, S. M.; Wenseleers, W.; Nugraha, A. R.; Saito, R.; Cognet, L.; Lounis, B., Luminescence Properties of Individual Empty and Water-Filled Single-Walled Carbon Nanotubes. *ACS Nano* **2012**, *6*, 2649-2655.

124.   Campo, J.; Piao, Y.; Lam, S.; Stafford, C. M.; Streit, J. K.; Simpson, J. R.; Hight Walker, A. R.; Fagan, J. A., Enhancing Single-Wall Carbon Nanotube Properties through Controlled Endohedral Filling. *Nanoscale Horiz.* **2016**, *1*, 317-324.

125.   Silvera-Batista, C. A.; Wang, R. K.; Weinberg, P.; Ziegler, K. J., Solvatochromic Shifts of Single-Walled Carbon Nanotubes in Nonpolar Microenvironments. *Phys. Chem. Chem. Phys.* **2010**, *12*, 6990–6998.

126.   Yang, L.; Han, J., Electronic Structure of Deformed Carbon Nanotubes. *Phys. Rev. Lett.* **2000**, *85*, 154-157.

127.   Fagan, J. A.; Huh, J. Y.; Simpson, J. R.; Blackburn, J. L.; Holt, J. M.; Larsen, B. A.; Walker, A. R., Separation of Empty and Water-Filled Single-Wall Carbon Nanotubes. *ACS Nano* **2011**, *5*, 3943-3953.

128.   Wu, X.; Kim, M.; Qu, H.; Wang, Y., Single-Defect Spectroscopy in the Shortwave Infrared. *Nat. Commun.* **2019**, *10*, 2672.

129.   Roxbury, D.; Jena, P. V.; Williams, R. M.; Enyedi, B.; Niethammer, P.; Marcet, S.; Verhaegen, M.; Blais-Ouellette, S.; Heller, D. A., Hyperspectral Microscopy of near-Infrared Fluorescence Enables 17-Chirality Carbon Nanotube Imaging. *Sci Rep* **2015**, *5*, 14167.

130.   Streit, J.; Snyder, C. R.; Campo, J.; Zheng, M.; Simpson, J. R.; Hight Walker, A. R.; Fagan, J. A., Alkane Encapsulation Induces Strain in Small-Diameter Single-Wall Carbon Nanotubes. *J. Phys. Chem. C* **2018**, *122*, 11577-11585.

131.   Leeuw, T. K.; Tsyboulski, D. A.; Nikolaev, P. N.; Bachilo, S. M.; Arepalli, S.; Weisman, R. B., Strain Measurements on Individual Single-Walled Carbon Nanotubes in a Polymer Host: Structure-Dependent Spectral Shifts and Load Transfer. *Nano Lett.* **2008**, *8*, 826-831.

132.   Yang, L.; Han, J., Electronic Structure of Deformed Carbon Nanotubes. *Phys. Rev. Lett.* **2000**, *85*, 154-157.

133.   Lebedkin, S.; Arnold, K.; Kiowski, O.; Hennrich, F.; Kappes, M. M., Raman Study of Individually Dispersed Single-Walled Carbon Nanotubes under Pressure. *Phys. Rev. B* **2006**, *73*.

134.   Dresselhaus, G.; Dresselhaus, M. S.; Saito, R., *Physical Properties of Carbon Nanotubes*. World scientific: 1998.

135.   Popov, V. N., Curvature Effects on the Structural, Electronic and Optical Properties of Isolated Single-Walled Carbon Nanotubes within a Symmetry-Adapted Non-Orthogonal Tight-Binding Model. *New J. Phys.* **2004**, *6*, 17-17.

136.   Pauling, L., *The Nature of the Chemical Bond*. Ithaca, NY: Cornell University Press: 1945.

137.   Rowland, R. S.; Taylor, R., Intermolecular Nonbonded Contact Distances in Organic Crystal Structures: Comparison with Distances Expected from Van Der Waals Radii. *J. Phys. Chem.* **1996**, *100*, 7384-7391.

138.   Yao, J.; Wang, H., Zeolitic Imidazolate Framework Composite Membranes and Thin Films: Synthesis and Applications. *Chem. Soc. Rev.* **2014**, *43*, 4470-4493.

139.   Lyndon, R.; You, W.; Ma, Y.; Bacsa, J.; Gong, Y.; Stangland, E. E.; Walton, K. S.; Sholl, D. S.; Lively, R. P., Tuning the Structures of Metal–Organic Frameworks Via a Mixed-Linker Strategy for Ethylene/Ethane Kinetic Separation. *Chem. Mater.* **2020**, *32*, 3715-3722.

140.   Lin, R. B.; Li, L.; Zhou, H. L.; Wu, H.; He, C.; Li, S.; Krishna, R.; Li, J.; Zhou, W.; Chen, B., Molecular Sieving of Ethylene from Ethane Using a Rigid Metal-Organic Framework. *Nat. Mater.* **2018**, *17*, 1128-1133.

141.   Redfern, L. R.; Farha, O. K., Mechanical Properties of Metal–Organic Frameworks. *Chem. Sci* **2019**, *10*, 10666-10679.

142.   Okubo, S.; Okazaki, T.; Kishi, N.; Joung, S.-K.; Nakanishi, T.; Okada, S.; Iijima, S., Diameter-Dependent Band Gap Modification of Single-Walled Carbon Nanotubes by Encapsulated Fullerenes. *J. Phys. Chem. C* **2008**, *113*, 571-575.

143.   Lee, A. J.; Wang, X.; Carlson, L. J.; Smyder, J. A.; Loesch, B.; Tu, X.; Zheng, M.; Krauss, T. D., Bright Fluorescence from Individual Single-Walled Carbon Nanotubes. *Nano Lett.* **2011**, *11*, 1636-1640.

144.   Jorgensen, W. L.; Maxwell, D. S.; Tirado-Rives, J., Development and Testing of the Opls All-Atom Force Field on Conformational Energetics and Properties of Organic Liquids. *J. Am. Chem. Soc.* **1996**, *118*, 11225-11236.

145.   Certain Equipment, Instruments or Materials Are Identified in This Paper in Order to Adequately Specify the Experimental Details. Such Identification Does Not Imply Recommendation by the National Institute of Standards and Technology (Nist) nor Does It Imply the Materials Are Necessarily the Best Available for the Purpose.

146.   Wang, P.; Kim, M.; Peng, Z.; Sun, C. F.; Mok, J.; Lieberman, A.; Wang, Y., Superacid-Surfactant Exchange: Enabling Nondestructive Dispersion of Full-Length Carbon Nanotubes in Water. *ACS Nano* **2017**, *11*, 9231-9238.

147.   Wallace, W. E., Mass Spectra. In *Nist Chemistry Webbook, Nist Standard Reference Database Number 69*, Linstrom, P. J.; Mallard, W. G., Eds. National Institute of Standards and Technology, Gaithersburg MD, 20899.

148.   Plimpton, S., Fast Parallel Algorithms for Short-Range Molecular Dynamics. *J. Comp. Phys.* **1995**, *117*, 1-19.

149.   Jorgensen, W. L.; Maxwell, D. S.; Tirado-Rives, J., Development and Testing of the Opls All-Atom Force Field on Conformational Energetics and Properties of Organic Liquids. *J. Am. Chem. Soc.* **1996**, *118*, 11225-11236.

150.   Stuart, S. J.; Tutein, A. B.; Harrison, J. A., A Reactive Potential for Hydrocarbons with Intermolecular Interactions. *J. Chem. Phys.* **2000**, *112*, 6472-6486.

151.   Jones, J. E., On the Determination of Molecular Fields. Ii. From the Equation of State of a Gas. *Proc. Royal Soc. A: Math. Phys. Eng. Sci.* **1924**, *106*, 463-477.

152.   Mooney, D. A.; Müller-Plathe, F.; Kremer, K., Simulation Studies for Liquid Phenol: Properties Evaluated and Tested over a Range of Temperatures. *Chem. Phys. Lett.* **1998**, *294*, 135-142.

153.   Berendsen, H. J. C.; Postma, J. P. M.; van Gunsteren, W. F.; Hermans, J., Interaction Models for Water in Relation to Protein Hydration. In *Intermolecular Forces*, Pullman, B., Ed. Springer Netherlands: Dordrecht, 1981; pp 331-342.

154.   Kresse, G.; Furthmüller, J., Efficient Iterative Schemes for Ab Initio Total-Energy Calculations Using a Plane-Wave Basis Set. *Phys. Rev. B* **1996**, *54*, 11169-11186.

155.   Perdew, J. P.; Burke, K.; Ernzerhof, M., Generalized Gradient Approximation Made Simple. *Phys. Rev. Lett.* **1996**, *77*, 3865-3868.

156.   Gifford, B. J.; Kilina, S.; Htoon, H.; Doorn, S. K.; Tretiak, S., Controlling Defect-State Photophysics in Covalently Functionalized Single-Walled Carbon Nanotubes. *Acc. Chem. Res.* **2020**, *53*, 1791-1801.

157.   Shiraki, T.; Miyauchi, Y.; Matsuda, K.; Nakashima, N., Carbon Nanotube Photoluminescence Modulation by Local Chemical and Supramolecular Chemical Functionalization. *Acc. Chem. Res.* **2020**, *53*, 1846-1859.

158.   Kim, M.; Wu, X.; Ao, G.; He, X.; Kwon, H.; Hartmann, N. F.; Zheng, M.; Doom, S. K.; Wang, Y., Mapping Structure-Property Relationships of Organic Color Centers. *Chem* **2018**, *4*, 2180-2191.

159.   Ma, X.; Hartmann, N. F.; Baldwin, J. K.; Doorn, S. K.; Htoon, H., Room-Temperature Single-Photon Generation from Solitary Dopants of Carbon Nanotubes. *Nat. Nanotechnol.* **2015**, *10*, 671-675.

160.   Gisin, N.; Thew, R., Quantum Communication. *Nat. Photonics* **2007**, *1*, 165-171.

161.   Gifford, B. J.; He, X.; Kim, M.; Kwon, H.; Saha, A.; Sifain, A. E.; Wang, Y.; Htoon, H.; Kilina, S.; Doorn, S. K.; Tretiak, S., Optical Effects of Divalent Functionalization of Carbon Nanotubes. *Chem. Mater.* **2019**, *31*, 6950-6961.

162.   Maeda, Y.; Murakoshi, H.; Tambo, H.; Zhao, P.; Kuroda, K.; Yamada, M.; Zhao, X.; Nagase, S.; Ehara, M., Thermodynamic Control of Quantum Defects on Single-Walled Carbon Nanotubes. *Chem. Commun.* **2019**, *55*, 13757-13760.

163.   Huang, Z.; Powell, L. R.; Wu, X.; Kim, M.; Qu, H.; Wang, P.; Fortner, J. L.; Xu, B.; Ng, A. L.; Wang, Y., Photolithographic Patterning of Organic Color-Centers. *Adv. Mater.* **2020**, *32*, e1906517.

164.   Salice, P.; Fabris, E.; Sartorio, C.; Fenaroli, D.; Figà, V.; Casaletto, M. P.; Cataldo, S.; Pignataro, B.; Menna, E., An Insight into the Functionalisation of Carbon Nanotubes by Diazonium Chemistry: Towards a Controlled Decoration. *Carbon* **2014**, *74*, 73-82.

165.   Combellas, C.; Kanoufi, F.; Pinson, J.; Podvorica, F. I., Time-of-Flight Secondary Ion Mass Spectroscopy Characterization of the Covalent Bonding between a Carbon Surface and Aryl Groups. *Langmuir* **2005**, *21*, 280-286.

166.   Greenwood, J.; Phan, T. H.; Fujita, Y.; Li, Z.; Ivasenko, O.; Vanderlinden, W.; Van Gorp, H.; Frederickx, W.; Lu, G.; Tahara, K.; Tobe, Y.; Uji-i, H.; Mertens, S. F. L.; De Feyter, S., Covalent Modification of Graphene and Graphite Using

Diazonium Chemistry: Tunable Grafting and Nanomanipulation. *ACS Nano* **2015**, *9*, 5520-5535.

167.   Ghosh, S.; Bachilo, S. M.; Simonette, R. A.; Beckingham, K. M.; Weisman, R. B., Oxygen Doping Modifies near-Infrared Band Gaps in Fluorescent Single-Walled Carbon Nanotubes. *Science* **2010**, *330*, 1656-1659.

168.   Iakoubovskii, K.; Minami, N.; Kim, Y.; Miyashita, K.; Kazaoui, S.; Nalini, B., Midgap Luminescence Centers in Single-Wall Carbon Nanotubes Created by Ultraviolet Illumination. *Appl. Phys. Lett.* **2006**, *89*, 173108.

169.   Zheng, Y.; Bachilo, S. M.; Weisman, R. B., Photoexcited Aromatic Reactants Give Multicolor Carbon Nanotube Fluorescence from Quantum Defects. *ACS Nano* **2020**, *14*, 715-723.

170.   Kozawa, D.; Wu, X.; Ishii, A.; Fortner, J.; Otsuka, K.; Xiang, R.; Inoue, T.; Maruyama, S.; Wang, Y.; Kato, Y. K. Formation of Organic Color Centers in Air-Suspended Carbon Nanotubes Using Vapor-Phase Reaction 2021, arXiv:2103.00689. arXiv e-prints. https://ui.adsabs.harvard.edu/abs/2021arXiv210300689K (accessed February 01, 2021).

171.   Brozena, A. H.; Leeds, J. D.; Zhang, Y.; Fourkas, J. T.; Wang, Y., Controlled Defects in Semiconducting Carbon Nanotubes Promote Efficient Generation and Luminescence of Trions. *ACS Nano* **2014**, *8*, 4239-4247.

172.   Kwon, H.; Kim, M.; Nutz, M.; Hartmann, N. F.; Perrin, V.; Meany, B.; Hofmann, M. S.; Clark, C. W.; Htoon, H.; Doorn, S. K.; Hogele, A.; Wang, Y., Probing Trions at Chemically Tailored Trapping Defects. *ACS Cent. Sci.* **2019**, *5*, 1786-1794.

173.   Lohmann, S. H.; Trerayapiwat, K. J.; Niklas, J.; Poluektov, O. G.; Sharifzadeh, S.; Ma, X., Sp3-Functionalization of Single-Walled Carbon Nanotubes Creates Localized Spins. *ACS Nano* **2020**, *14*, 17675-17682.

174.   Wang, C.; Meany, B.; Wang, Y., Optically Triggered Melting of DNA on Individual Semiconducting Carbon Nanotubes. *Angew. Chem. Int. Ed. Engl.* **2017**, *56*, 9326-9330.

175.   Wu, X.; Kim, M.; Qu, H.; Wang, Y., Single-Defect Spectroscopy in the Shortwave Infrared. *Nat. Commun.* **2019**, *10*, 2672.

176.   Souza, N.; Zeiger, M.; Presser, V.; Mücklich, F., In Situ Tracking of Defect Healing and Purification of Single-Wall Carbon Nanotubes with Laser Radiation by Time-Resolved Raman Spectroscopy. *RSC Adv.* **2015**, *5*, 62149-62159.

177.   Settele, S.; Berger, F. J.; Lindenthal, S.; Zhao, S.; El Yumin, A. A.; Zorn, N. F.; Asyuda, A.; Zharnikov, M.; Hogele, A.; Zaumseil, J., Synthetic Control over the Binding Configuration of Luminescent Sp3-Defects in Single-Walled Carbon Nanotubes. *Nat. Commun.* **2021**, *12*, 2119.

178.   Gifford, B. J.; Sifain, A. E.; Htoon, H.; Doorn, S. K.; Kilina, S.; Tretiak, S., Correction Scheme for Comparison of Computed and Experimental Optical Transition Energies in Functionalized Single-Walled Carbon Nanotubes. *J. Phys. Chem. Lett.* **2018**, *9*, 2460-2468.

179.   Kilina, S.; Ramirez, J.; Tretiak, S., Brightening of the Lowest Exciton in Carbon Nanotubes Via Chemical Functionalization. *Nano Lett.* **2012**, *12*, 2306-2312.

180.   Carbon Nanotube, Single-Walled. https://www.sigmaaldrich.com/US/en/product/aldrich/773735 (accessed 10/25/2021).

181.   X. Cao, J.; H. Yan, X.; Xiao, Y., Specific Heat of Single-Walled Carbon Nanotubes: A Lattice Dynamics Study. *J. Phys. Soc. Jpn.* **2003**, *72*, 2256-2259.

182.   Khoukhi, M.; Tahat, M., Effect of Temperature and Density Variations on Thermal Conductivity of Polystyrene Insulation Materials in Oman Climate. *J. Eng. Phys. Thermophys.* **2015**, *88*, 994-998.

183.   Wang, H.-D.; Liu, J.-H.; Guo, Z.-Y.; Zhang, X.; Zhang, R.-F.; Wei, F.; Li, T.-Y., Thermal Transport across the Interface between a Suspended Single-Walled Carbon Nanotube and Air. *Nanoscale Microscale Thermophys. Eng.* **2013**, *17*, 349-365.

184.   Huxtable, S. T.; Cahill, D. G.; Shenogin, S.; Xue, L.; Ozisik, R.; Barone, P.; Usrey, M.; Strano, M. S.; Siddons, G.; Shim, M.; Keblinski, P., Interfacial Heat Flow in Carbon Nanotube Suspensions. *Nat. Mater.* **2003**, *2*, 731-734.

185.   Streit, J. K.; Bachilo, S. M.; Ghosh, S.; Lin, C.-W.; Weisman, R. B., Directly Measured Optical Absorption Cross Sections for Structure-Selected Single-Walled Carbon Nanotubes. *Nano Lett.* **2014**, *14*, 1530-1536.

186.   Frisch, M. J.; Trucks, G. W.; Schlegel, H. B.; Scuseria, G. E.; Robb, M. A.; Cheeseman, J. R.; Scalmani, G.; Barone, V.; Petersson, G. A.; Nakatsuji, H.; Li, X.; Caricato, M.; Marenich, A. V.; Bloino, J.; Janesko, B. G.; Gomperts, R.; Mennucci, B.; Hratchian, H. P.; Ortiz, J. V.; Izmaylov, A. F., et al. *Gaussian 09*, Gaussian, Inc.: Wallingford, CT, 2009.

187.   Yanai, T.; Tew, D. P.; Handy, N. C., A New Hybrid Exchange–Correlation Functional Using the Coulomb-Attenuating Method (Cam-B3lyp). *Chem. Phys. Lett.* **2004**, *393*, 51-57.

188.   Binkley, J. S.; Pople, J. A.; Hehre, W. J., Self-Consistent Molecular Orbital Methods. 21. Small Split-Valence Basis Sets for First-Row Elements. *J. Am. Chem. Soc.* **2002**, *102*, 939-947.

189.   Martin, R. L., Natural Transition Orbitals. *J. Chem. Phys.* **2003**, *118*, 4775-4777.

190.   Hartmann, N. F.; Velizhanin, K. A.; Haroz, E. H.; Kim, M.; Ma, X.; Wang, Y.; Htoon, H.; Doorn, S. K., Photoluminescence Dynamics of Aryl Sp3 Defect States in Single-Walled Carbon Nanotubes. *ACS Nano* **2016**, *10*, 8355-8365.

191.   Sykes, M. E.; Kim, M.; Wu, X.; Wiederrecht, G. P.; Peng, L.; Wang, Y.; Gosztola, D. J.; Ma, X., Ultrafast Exciton Trapping at Sp3 Quantum Defects in Carbon Nanotubes. *ACS Nano* **2019**, *13*, 13264-13270.

192.   Miyauchi, Y.; Iwamura, M.; Mouri, S.; Kawazoe, T.; Ohtsu, M.; Matsuda, K., Brightening of Excitons in Carbon Nanotubes on Dimensionality Modification. *Nat. Photonics* **2013**, *7*, 715-719.

193.   Qu, H.; Wu, X.; Fortner, J.; Kim, M.; Wang, P.; Wang, Y., Reconfiguring Organic Color Centers on the Sp2 Carbon Lattice of Single-Walled Carbon Nanotubes. *ACS Nano* **2022**, *16*, 2077-2087.

194.   Lounis, B.; Orrit, M., Single-Photon Sources. *Rep. Prog. Phys.* **2005**, *68*, 1129-1179.

195.   Antaris, A. L.; Yaghi, O. K.; Hong, G.; Diao, S.; Zhang, B.; Yang, J.; Chew, L.; Dai, H., Single Chirality (6,4) Single-Walled Carbon Nanotubes for Fluorescence Imaging with Silicon Detectors. *Small* **2015**, *11*, 6325-6330.

196.   Hong, G.; Diao, S.; Antaris, A. L.; Dai, H., Carbon Nanomaterials for Biological Imaging and Nanomedicinal Therapy. *Chem. Rev.* **2015**, *115*, 10816-10906.

197.   Tobia, D.; Harrison, R.; Phillips, B.; White, T. L.; DiMare, M.; Rickborn, B., Unusual Stability of N-Methylmaleimide Cycloadducts: Characterization of Isobenzofuran Retro-Diels-Alder Reactions. *The Journal of Organic Chemistry* **1993**, *58*, 6701-6706.

198.   Hoffmann, R.; Woodward, R. B., Orbital Symmetry Control of Chemical Reactions. *Science* **1970**, *167*, 825-831.

199.   Woodward, R. B.; Hoffmann, R., Stereochemistry of Electrocyclic Reactions. *J. Am. Chem. Soc.* **2002**, *87*, 395-397.

200.   Kumar, I.; Rana, S.; Cho, J. W., Cycloaddition Reactions: A Controlled Approach for Carbon Nanotube Functionalization. *Chemistry* **2011**, *17*, 11092-11101.

201.   He, X.; Kevlishvili, I.; Murcek, K.; Liu, P.; Star, A., [2pi + 2pi] Photocycloaddition of Enones to Single-Walled Carbon Nanotubes Creates Fluorescent Quantum Defects. *ACS Nano* **2021**, *15*, 4833-4844.

202.   Li, Y.; Wu, X.; Kim, M.; Fortner, J.; Qu, H.; Wang, Y., Fluorescent Ultrashort Nanotubes from Defect-Induced Chemical Cutting. *Chem. Mater.* **2019**, *31*, 4536-4544.